2mip

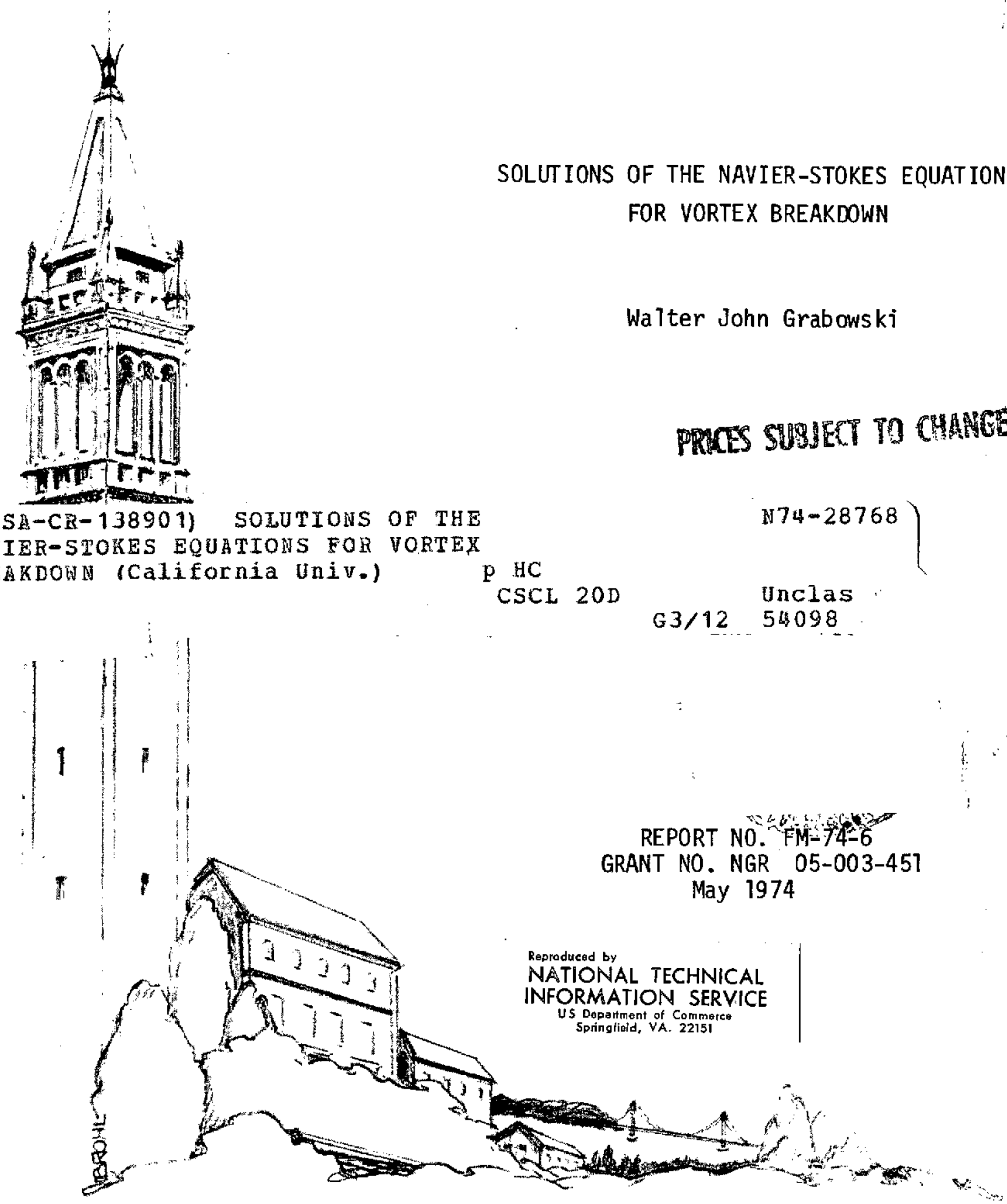

SOLUTIONS OF THE NAVIER-STOKES EQUATIONS FOR VORTEX BREAKDOWN

Walter John Grabowski

(NASA-CR-138901) SOLUTIONS OF THE NAVIER-STOKES EQUATIONS FOR VORTEX BREAKDOWN (California Univ.) p HC CSCL 20D
N74-28768
Unclas
G3/12 54098

REPORT NO. FM-74-6
GRANT NO. NGR 05-003-451
May 1974

COLLEGE OF ENGINEERING

UNIVERSITY OF CALIFORNIA, Berkeley

1438

GRANT NO. NGR 05-003-451
REPORT NO. FM-74-6
May 1974

SUPPORTED BY
NATIONAL AERONAUTICS AND SPACE
ADMINISTRATION -AMES RESEARCH CENTER

SOLUTIONS OF THE NAVIER-STOKES EQUATIONS FOR VORTEX BREAKDOWN

Walter John Grabowski

FACULTY INVESTIGATOR:
S.A. Berger, Professor of Aeronautical Sciences

PROGRAM DIRECTOR: M. Holt,
Professor of
Aeronautical Sciences

May 1974

UNIVERSITY OF CALIFORNIA

Mechanical Engineering Department
Berkeley, California 94720

ACKNOWLEDGMENTS

I would like to express my special thanks to my teacher, Professor Stanley A. Berger, whose guidance and encouragement made this study possible. I would also like to thank Professor Maurice Holt for his interest and many valuable suggestions, and Professor Alexandre J. Chorin for his generous advice regarding the numerical formulation of the problem. Also, special mention should be made of the efforts of Mrs. Arlene Martin, who laboriously typed all of the manuscript.

Finally, I would like to thank my wife, Sharon, without whose love, patience and understanding this work could never have been completed.

ABSTRACT

Several explanations of the vortex breakdown phenomenon have been proposed, including the finite transition theory of Benjamin and the boundary-layer separation analogy of Gartshore, Hall, and others. However, due essentially to a lack of quantitative information with which to compare the predictions of these theories, none has gained general acceptance. A numerical investigation has, therefore, been undertaken to provide such information. Steady solutions of the Navier-Stokes equations, in terms of velocity and pressure, for breakdown in an unconfined viscous vortex are obtained numerically using the "artificial compressibility" technique of Chorin combined with an ADI finite-difference scheme. Axisymmetry is assumed and boundary conditions are carefully applied at the boundaries of a large finite region in an axial plane while resolution near the axis is maintained by a coordinate transformation. The solutions, which are obtained for Reynolds numbers up to 200 based on the free-stream axial velocity and a characteristic core radius, show that breakdown results from the diffusion and convection of vorticity away from the vortex core which, because of the strong coupling between the circumferential and axial velocity fields in strongly swirling flows, can lead to stagnation and reversal of the axial flow near the axis. Breakdown is shown to be a necessary occurrence in flows with large enough values of a single parameter, calculated from conditions specified upstream, which decreases as Reynolds number increases toward the minimum required for the appearance of discontinuous solutions of the quasi-cylindrical equations, which apply only to high Reynolds number flows. These discontinuities are due to the large axial gradients which occur in flows which break down or nearly break down. Breakdowns in flows with both super- and subcritical upstream conditions are obtained so that the finite transition theory, which requires supercritical conditions upstream, is unable to fully account for the phenomenon. Based on the appearance in the solutions of a second retardation of the axial velocity behind the breakdown bubble in highly swirling flows, an explanation of the several experimentally observed forms of breakdown is proposed.

TABLE OF CONTENTS

LIST OF FIGURES

1.0 INTRODUCTION

1.1 Motivation for This Study

The rolled-up wake system behind a lifting wing consists essentially of two oppositely rotating viscous cores each of which is surrounded by a swirling irrotational flow. In the case of the very heavy transport aircraft which have been introduced in the past several years, these viscous vortex systems can extend many miles, and remain vigorous, with high rotational velocities, for relatively long periods of time. They are a particular danger in the crowded airspace near airports, and encounters of smaller aircraft with such flows have resulted in numerous fatal accidents. There is an obvious necessity to in some way bring about their more rapid dissipation, and vortex breakdown is one of several mechanisms which have been suggested for this purpose. Unfortunately, the breakdown phenomenon is not very well understood, and while there is no lack of experimental observations, little quantitative information exists with which to correlate any of the several existing theories.

It is with these considerations that a numerical approach to the study of vortex breakdown is undertaken. It is hoped that this study will yield practical information regarding the behavior of vortex flows exhibiting breakdown, and provide some insight into a poorly understood phenomenon.

1.2 Definition and Description of Vortex Breakdown

To begin this study, a definition of vortex breakdown is required.

Vortex breakdown is a pronounced decrease in the axial velocity on the axis of an axisymmetric swirling flow, and the corresponding divergence of the stream surfaces near the axis.

Generally, the axial flow retardation results in stagnation and a region of reversed flow which may or may not be axisymmetric.

A summary of the experimental observations of Harvey (1962) and Sarpkaya (1971a,b) will serve to present the several forms in which vortex breakdown can appear.

For flow in a tube, initially *without* swirl, a sequence of phenomena, made visible by injecting dye or smoke into the tube axis, may be observed as the amount of initial swirl is increased.

The first to appear, for sufficient swirl, is an asymmetric phenomenon. The axial filament deforms into a spiral following an abrupt kink which occurs just upstream of a stagnation point. The spiral persists for a few turns, then breaks up into turbulence.

As the swirl is increased a second asymmetric phenomenon may occur. The axial filament decelerates and expands into a curved sheet which deforms sinuously, and, as in the previous case, gradually breaks up into turbulence. There is no evidence of stagnation in these flows.

For larger amounts of swirl, the axial filament spreads symmetrically at a stagnation point and the outer stream surfaces expand as if meeting a solid body. Behind the stagnation point there can be either a bubble of recirculating fluid followed by a return to conditions similar to those upstream and a spiral breakdown like that described above, or a bubble immediately followed by an expanding region of turbulent flow.

Finally, if enough swirl is imparted, a core of reversed flow stretching along the axis for nearly the entire tube length can be obtained.

1.3 Observations of Vortex Breakdown

Besides its possible occurrence in trailing vortex systems, vortex breakdown has been observed and studied in a variety of flow situations.

The first recorded observation of breakdown was in conical leading edge vortices in separated flow over highly swept leading edges at high angles of attack (Peckham and Atkinson, 1957), and most of the early experimental investigations dealt with its effect on lift and moment coefficients (Elle, 1958; Werlé, 1960; Lambourne and Bryer, 1961). It was observed in supersonic as well as subsonic flow by Lambourne and Bryer (1961).

Breakdown can occur in swirling flow in nozzles and diffusers (Gore and Ranz, 1964; So, 1967), and may also occur in tornado funnels (Morton, 1966). It was studied extensively by both Harvey (1962) and Sarpkaya (1971a,b) in vortex tubes with the aid of smoke and dye, as mentioned in the previous section.

Although there is no lack of experimental observations of breakdown, the extreme sensitivity of the phenomenon to disturbances makes the introduction of probes impossible so that very little quantitative information exists. Most of what is known about flow conditions immediately upstream and downstream of breakdown has been deduced from photographs. Laser anemometry, which is now being introduced to study trailing vortices, would be a useful technique for studying breakdown.

1.4 Theoretical Explanations

The several theoretical explanations of vortex breakdown, which are discussed in detail in the review by Hall (1972), may be divided into three basic categories:

(1) Vortex breakdown is similar to the separation of a two-dimensional boundary layer.

(2) Vortex breakdown is a consequence of hydrodynamic instability.

(3) Vortex breakdown is in some way dependent on the existence of a critical state.

The first of these explanations, that breakdown is analogous to the separation of a two-dimensional boundary layer, developed from the attempts of Gartshore (1962,1963) and Hall (1966,1967) to obtain solutions of a system of equations which were obtained from the full, viscous, incompressible equations from the assumptions that the Reynolds number of the flow, based on a free stream velocity and vortex core radius, is large and that gradients in the axial direction are much smaller than in the radial. The resulting equations of this so-called "quasi-cylindrical" approximation are very much like the two-dimensional boundary-layer equations, and may be solved from given upstream conditions. Both Gartshore, who used an integral method similar to the Kármán-Polhausen technique for the boundary layer equations, and Hall, who used a finite-difference method, found that for certain upstream conditions their solutions could not be continued beyond some point downstream. They then assumed that this inability to continue was due to the violation of the requirement that $\partial/\partial z << \partial/\partial r$, and that breakdown must occur nearby. This is analogous to the assumption that boundary-layer separation occurs near the computed point at which wall shear vanishes even though the boundary-layer approximation may have failed somewhere upstream.

The second theory, that breakdown is the result of a hydrodynamic instability to spiral disturbances was proposed by Ludwieg (1962,1965). He found a stability boundary for spiralling flows in a narrow annulus which was experimentally verified and suggested that it could be at least an approximate necessary condition for the stability of vortex flows.

The third theory, that breakdown depends in some way on the existence of a critical state, was initially proposed by Squire (1960). He looked for conditions, which were later defined by Benjamin (1962) as the critical state, in which a standing cylindrical wave of infinite length could be first sustained, and assumed that such conditions could lead to breakdown. He considered three different swirl distributions and found critical values of the ratio of the swirl velocity to the axial velocity to be of the order of unity.

Benjamin (1962,1965,1967;Fraenkel,1967), proposed that breakdown was a transition between two steady states of axisymmetric swirling flow and made an analogy with the hydraulic jump in open-channel flow. He showed that in an inviscid cylindrical swirling flow, the equation of motion for the stream function ψ possesses an infinite number of solutions for given values of ψ at $r = 0$ and $r = R$, and given distributions, with respect to ψ, of the circulation and the total head. He argued that only two of the solutions, which do not intersect except at their endpoints, are relevant, and showed that one of the solutions is supercritical, that is, cannot support infinitesimal standing waves, and that the other is subcritical, and can. The momentum flux (or flow force)

$$2\pi \int_0^R (p + \rho w^2)\, r\, dr$$

of the subcritical flow, however, is larger than that of the supercritical so that if a transition from one to the other is to occur the differences in the momentum flux must be made up. He then explained vortex breakdown as the transition of the flow from the supercritical to the subcritical state, with the appearance of axisymmetric standing waves in the subcritical state to make up the momentum flux difference when it is small. Larger momentum differences, however, cannot be made up in this way and he proposed that the leading wave then breaks and results in turbulence with a corresponding reduction in the momentum flux.

Recent theoretical work has combined elements of these theories.

Hall (1972) by considering two solutions, one expressed as a perturbation of the other, of the quasi-cylindrical equation for inviscid flow at cross sections a small distance Δz apart, showed that the condition that the perturbation not vanish as Δz approaches zero, that is, that axial gradients become infinitely large, is identical with the condition of the critical state.

He then described breakdown as the result of the initially supercritical flow, which may be described by the quasi-cylindrical approximation, approaching the critical state where the approximation fails and derivatives increase without bounds. He thus identified with vortex breakdown both the failure of the quasi-cylindrical approximation and the appearance of the critical state.

Mager (1972), following the work of Gartshore (1963) and Bossel (1967,1971), showed that the solutions of the quasi-cylindrical momentum-integral equations have two distinct branches and, with the appropriate upstream conditions, discontinuities which represent the appearance of infinite axial gradients and are assumed to signal the inception of vortex breakdown. He then demonstrated that Benjamin's finite transition could be explained as a sudden cross-over, upstream of the discontinuity, from one branch of the solution to the other, and suggested that the physical manifestation of the discontinuity might be the spiral breakdown while the cross-over, if it occurred, might appear as the axisymmetric bubble upstream. An important aspect of this analysis is that the discontinuities may arise both in initially supercritical *and* subcritical flows, and that they occur in the vicinity of the critical state.

The work of Hall and Mager suggests, therefore, that the critical state, which is determined from an inviscid analysis, is approximately the condition for which the quasi-cylindrical approximation fails and breakdown occurs, and that this condition may be approached by both supercritical and subcritical flows.

1.5 Outline of the Study

This study obtains numerical solutions of the full Navier-Stokes equations for a single, unconfined, viscous vortex, imbedded in an irrotational flow with a uniform free-stream axial velocity. Chapter 2 describes the mathematical formulation of the problem, and Chapter 3 presents the numerical model. Results and discussion are presented in Chapter 4, and Chapter 5 summarizes the findings of this study.

2.0 MATHEMATICAL MODEL

2.1 Equations

While energy and angular momentum considerations require that an unconfined vortex appear as a member of an oppositely rotating vortex pair (Morton, 1969), a single vortex may be studied with the assumption that its opposite is far enough away to have little effect. Assuming axisymmetry and that the flow is steady in a coordinate system fixed with respect to the vortex generator (e.g., a lifting wing), the momentum equations for an incompressible flow in the radial, circumferential, and axial directions reduce to

$$\rho\left(u\frac{\partial u}{\partial r} + w\frac{\partial u}{\partial z} - \frac{v^2}{r}\right) = -\frac{\partial p}{\partial r} + \mu\left(\frac{\partial^2 u}{\partial r^2} + \frac{1}{r}\frac{\partial u}{\partial r} + \frac{\partial^2 u}{\partial z^2} - \frac{u}{r^2}\right) \tag{2-1}$$

$$\rho\left(u\frac{\partial v}{\partial r} + w\frac{\partial v}{\partial z} + \frac{uv}{r}\right) = \mu\left(\frac{\partial^2 v}{\partial r^2} + \frac{1}{r}\frac{\partial v}{\partial r} + \frac{\partial^2 v}{\partial z^2} - \frac{v}{r^2}\right) \tag{2-2}$$

$$\rho\left(u\frac{\partial w}{\partial r} + w\frac{\partial w}{\partial z}\right) = -\frac{\partial p}{\partial z} + \mu\left(\frac{\partial^2 w}{\partial r^2} + \frac{1}{r}\frac{\partial w}{\partial r} + \frac{\partial^2 w}{\partial z^2}\right) \tag{2-3}$$

while mass conservation may be expressed as

$$\frac{1}{r}\frac{\partial(ur)}{\partial r} + \frac{\partial w}{\partial z} = 0 \tag{2-4}$$

ρ is the density, μ the viscosity, p the pressure, and u, v, and w are the velocity components in the r, θ, and z directions, respectively (Fig. 1).

Non-dimensionalizing lengths by a characteristic core radius, r_c^*, velocities by W_∞, the free stream axial velocity, and defining a dimensionless pressure, $(p-p_\infty)/\rho W_\infty^2$, where p_∞ is the uniform ambient pressure infinitely far from the vortex, casts equations (2-1) through (2-4) in the following dimensionless form

$$u \frac{\partial u}{\partial r} + w \frac{\partial u}{\partial z} - \frac{v^2}{r} = - \frac{\partial p}{\partial r} + \frac{1}{Re} \left(\frac{\partial^2 u}{\partial r^2} + \frac{1}{r} \frac{\partial u}{\partial r} + \frac{\partial^2 u}{\partial z^2} - \frac{u}{r^2} \right) \tag{2-5}$$

$$u \frac{\partial v}{\partial r} + w \frac{\partial v}{\partial z} + \frac{uv}{r} = \frac{1}{Re} \left(\frac{\partial^2 v}{\partial r^2} + \frac{1}{r} \frac{\partial v}{\partial r} + \frac{\partial^2 v}{\partial z^2} - \frac{v}{r^2} \right) \tag{2-6}$$

$$u \frac{\partial w}{\partial r} + w \frac{\partial w}{\partial z} = - \frac{\partial p}{\partial z} + \frac{1}{Re} \left(\frac{\partial^2 w}{\partial r^2} + \frac{1}{r} \frac{\partial w}{\partial r} + \frac{\partial^2 w}{\partial z^2} \right) \tag{2-7}$$

$$\frac{1}{r} \frac{\partial (ur)}{\partial r} + \frac{\partial w}{\partial z} = 0 \tag{2-8}$$

where for convenience the same symbols for the variables have been retained, and $Re \equiv W_\infty r_c^*/\nu$ is the core Reynolds number.

Although a solution of these equations is to be obtained for an unconfined vortex, boundary conditions applied at the boundary of a finite domain will be used for reasons discussed in a later section.

2.2 Boundary Conditions

Choosing the core radius at $z = 0$ as r_c^* conditions are specified on the boundary of a region $0 \leq r \leq R$, $0 \leq z \leq L$ where R and L are much larger than one. The boundary conditions, depicted graphically in Fig. 2, are given below. A detailed explanation follows.

At the upstream, $z = 0$, boundary the velocities are specified functions of r with

$$u(r) = 0 \qquad \text{for} \quad 0 \leq r \leq R \tag{2-9}$$

and

$$\left.\begin{aligned} v(r) &= V\, r(2-r^2) \\ w(r) &= \alpha + (1-\alpha)\, r^2\,(6 - 8r + 3r^2) \end{aligned}\right\} \quad \text{for } 0 \le r \le 1 \qquad (2\text{-}10)$$

while

$$\left.\begin{aligned} v(r) &= V/R \\ w(r) &= 1 \end{aligned}\right\} \quad \text{for } 1 \le r \le R \qquad (2\text{-}11)$$

and α and V are defined below.

At the downstream, $z = L$, boundary

$$\frac{\partial u}{\partial z} = 0 \quad , \quad \frac{\partial v}{\partial z} = 0 \quad , \quad \text{and} \quad \frac{\partial w}{\partial z} = 0 \qquad (2\text{-}12)$$

are imposed for $0 \le r \le R$.

At the axis, $r = 0$,

$$u = 0 \quad , \quad v = 0 \quad , \quad \text{and} \quad \frac{\partial w}{\partial r} = 0 \qquad (2\text{-}13)$$

$$\text{for } 0 \le z \le L$$

while at the radial boundary, $r = R$

$$\frac{\partial (ur)}{\partial r} = 0 \quad , \quad v = V/R \quad , \quad \text{and} \quad w = 1 \qquad (2\text{-}14)$$

$$\text{for } 0 \le z \le L.$$

The upstream, $z = 0$, conditions were chosen to approximate the experimentally observed behavior of the velocity in the cores of trailing vortices (McCormick, Tangler, and Sherrieb, 1968; Chigier and Corsiglia, 1971,1972), and were used by Mager (1971) in his breakdown analysis. The vorticity is concentrated within the vortex core and the external angular velocity is then required to have the irrotational, r^{-1}, distribution. V is the specified velocity at the core edge and is equal to the circulation around the core after non-dimensionalization by $2\pi r_c W_\infty$. The cubic form of $v(r)$ allows solid-body-like rotation near the core center, and, since the derivatives are equal at $r = 1$, a smooth transition to the irrotational flow at the core edge. The maximum angular velocity, 1.088 V, occurs at $r = \sqrt{2/3}$.

The quartic distribution of axial velocity in the core satisfies the requirements that it join smoothly with the uniform axial flow outside, and that $\partial w/\partial r$ and, hence, shear, vanish at the axis. The form factor α is the ratio of the axial velocity at the core center to the velocity in the free stream.

These distributions, requiring the specification of only two parameters, are quite flexible. Any desired amount of swirl and, therefore, circulation may be obtained by proper choice of V, while setting α less than or greater than one yields axial velocity profiles with axial momentum flux deficits or excesses (i.e., wake-like or jet-like profiles). Uniform axial flow results when $\alpha = 1$.

The downstream, $z = L$, conditions assume that L has been chosen large enough that the rate of change of the flow properties with z is negligibly small. This approach is far less restrictive than, for example, attempting to specify *a priori* the solution downstream. Although some small error is introduced, its effect upstream is limited for large enough L, as a numerical investigation described in a later section demonstrated. Similar conditions for primitive $(\vec{v},p)$ variable formulations at outflow boundaries have been used by several authors (e.g., Taylor and Ndefo, 1970; Fortin, Peyret, Temam, 1971).

The axis, $r = 0$, conditions result from mass conservation, which requires that $u = 0$, and from the requirement that shear stress at the axis and, therefore, v and $\partial w/\partial r$ vanish.

Conditions at $r = R$ are based on the assumption that phenomena near the axis, including both breakdown and diffusion of the vortex core have negligible effect on the circulation and axial velocity at large radial distances from the axis. The axial velocity is then simply that in the uniform free stream, while the swirl velocity is given by the irrotational distribution. Continuity yields $\partial(ur)/\partial r = 0$, allowing entrainment of fluid from outside the solution domain.

3.0 NUMERICAL METHOD

3.1 Artificial Compressibility

After considering a number of numerical methods for obtaining solutions of equations (2-5) through (2-8), Chorin's "artificial compressibility" technique (Chorin, 1967) was selected. This method solves the primitive variable equations directly, avoiding the use of vorticity-stream function equations which, for axisymmetric flows with swirl, are quite complicated, and which, in general, tend to yield less accurate numerical solutions than the corresponding primitive variable equations (Orzag, 1971,1974). Chorin's method is simple, efficient, and has a significant advantage over other primitive variable techniques in that the solution of a Poisson equation for pressure and, consequently, boundary conditions for the pressure, are not required. A brief explanation of the method follows.

Beginning with the equations of motion for a steady, incompressible flow, for which a solution is desired

$$\vec{v} \cdot \nabla\vec{v} = -\nabla p + \frac{1}{Re} \nabla^2 \vec{v} \qquad (3\text{-}1)$$

$$\nabla \cdot \vec{v} = 0 \qquad (3\text{-}2)$$

an auxiliary system of equations

$$\frac{\partial\vec{v}}{\partial t} + \vec{v} \cdot \nabla\vec{v} = -\nabla p + \frac{1}{Re} \nabla^2 \vec{v} \qquad (3\text{-}3)$$

$$\delta \frac{\partial p}{\partial t} + \nabla \cdot \vec{v} = 0 \qquad (3\text{-}4)$$

is introduced. This new system features a time-like dependence on a new variable t, and the replacement of the kinematic constraint (3-2) by (3-4), which permits a simple explicit variation of the pressure field. These auxiliary equations may be solved numerically from essentially arbitrary initial conditions to a steady (i.e., t-independent) limit using any of a large variety of finite difference schemes developed for initial value problems. Then, since steady solutions of (3-3) and (3-4) necessarily satisfy (3-1) and (3-2), the resulting numerical solution satisfies the original differential equations to the spatial order of accuracy of the particular difference scheme used. The desired solution is thus obtained. The artificial compressibility, δ, plays a role similar to a relaxation parameter and vanishes from the steady solution. Its numerical value is chosen for most rapid convergence.

Convergence of the auxiliary system of equations has been proven for Stokes' flow with $\vec{v}$ specified at boundaries (Chorin, op. cit.; Fortin, Temam, and Peyret, 1971), and the method has been applied with various difference schemes to a number of problems (Chorin, op. cit.; Fortin, et al.; Plows, 1968).

Applying the method directly to this study, solutions of (2-5) through (2-8) should be obtained by the solution of the corresponding auxiliary equations, which are simply (2-5) through (2-8) with the additional terms $\partial u/\partial t$, $\partial v/\partial t$, $\partial w/\partial t$, and $\delta\partial p/\partial t$, respectively, carried out to a steady state. Rather than attempting a finite difference solution of the auxiliary equations directly, however, a coordinate transformation, described in the next section, was first applied.

3.2 Coordinate Transformation

Since vortex breakdown is essentially a phenomenon of the vortex core, good resolution and a finely-spaced grid are required in and near the core. Unfortunately, uniform grid spacing in the rather large region, $0 \leq r \leq R$, $0 \leq z \leq L$, is then not possible because of the overwhelming number of grid points which would be required. However, explicit in the boundary conditions

$$\frac{\partial u}{\partial z} = 0 \quad , \quad \frac{\partial v}{\partial z} = 0 \quad , \quad \frac{\partial w}{\partial z} = 0$$

at $z = L$ and both explicit and implicit in the condition

$$\frac{\partial (ur)}{\partial r} = 0 \quad , \quad v = V/R \quad , \quad w = 1$$

at $r = R$ are the assumptions that derivatives in the axial direction far enough downstream and in the radial direction outside the core become increasingly small with r and z, respectively. Therefore, an unequally spaced array of grid points with increasing mesh width as both r and z increase is sufficient, and, since it makes more efficient use of each grid point, definitely advantageous.

The effect of a non-uniform mesh has been obtained in this study through the application of the coordinate transformation

$$y = \frac{1}{a} \ln (1 + r/b) \tag{3-5}$$

$$x = \frac{1}{c} \ln (1 + z/d) \tag{3-6}$$

which, with proper choice of a, b, c, and d, effectively stretches the region near the axis radially and the region near the upstream boundary axially, while contracting the more distant regions. These transformations have been used in a number of problems

(Skoglund and Gay, 1968; Rimon and Cheng, 1969; Pao and Daugherty, 1969), and have been applied in this study to map the region $0 \leq r \leq R$, $0 \leq z \leq L$ onto $0 \leq y \leq 1/2$, $0 \leq x \leq 1$. Numerical values of a, b, c, and d are determined in practice from R, L, the total number of grid points in each direction, and the number of points desired in any increment of r and z originating at zero.

Details regarding the application of these transformations to the auxiliary equation have been left to Appendix A. The transformed auxiliary equations are

$$\frac{\partial u}{\partial t} + f\,u\,\frac{\partial u}{\partial y} + s\,w\,\frac{\partial u}{\partial x} - e\,v^2 = -f\,\frac{\partial p}{\partial y} + \frac{1}{Re}\left[f^2\,\frac{\partial^2 u}{\partial y^2} + (g+ef)\,\frac{\partial u}{\partial y} + s^2\,\frac{\partial^2 u}{\partial x^2} + t\,\frac{\partial u}{\partial x} - e^2\,u\right] \qquad (3\text{-}7)$$

$$\frac{\partial v}{\partial t} + f\,u\,\frac{\partial v}{\partial y} + s\,w\,\frac{\partial v}{\partial x} + e\,u\,v = \frac{1}{Re}\left[f^2\,\frac{\partial^2 v}{\partial y^2} + (g+ef)\,\frac{\partial v}{\partial y} + s^2\,\frac{\partial^2 v}{\partial x^2} + t\,\frac{\partial v}{\partial x} - e^2\,v\right] \qquad (3\text{-}8)$$

$$\frac{\partial w}{\partial t} + f\,u\,\frac{\partial w}{\partial y} + s\,w\,\frac{\partial w}{\partial x} = -s\,\frac{\partial p}{\partial x} + \frac{1}{Re}\left[f^2\,\frac{\partial^2 w}{\partial y^2} + (g+ef)\,\frac{\partial w}{\partial y} + s^2\,\frac{\partial^2 w}{\partial x^2} + t\,\frac{\partial w}{\partial x}\right] \qquad (3\text{-}9)$$

$$\delta\,\frac{\partial p}{\partial t} + e\,f\,\frac{\partial (u/e)}{\partial y} + \frac{\partial w}{\partial x} = 0 \qquad (3\text{-}10)$$

where $f = f(y)$, $g = g(y)$, $s = s(x)$, $t = t(x)$ are coefficients defined in Appendix A, and $e = 1/r(y)$.

The transformed boundary conditions are as follows.

For $x = 0, \quad 0 \leq y \leq 1/2$:

u, v, and w are specified functions of r(y) as given previously. (3-11)

For $x = 1, \quad 0 \leq y \leq 1/2$:

$$\frac{\partial u}{\partial x} = 0 \quad , \quad \frac{\partial v}{\partial x} = 0 \quad , \text{ and } \quad \frac{\partial w}{\partial x} = 0 \quad . \qquad (3\text{-}12)$$

For $0 \leq x \leq 1, \quad y = 0$:

$$u = 0 \quad , \quad v = 0 \quad , \quad \text{and} \quad \frac{\partial w}{\partial y} = 0 \qquad (3\text{-}13)$$

while, for $0 \leq x \leq 1, \quad y = 1/2$:

$$u + \frac{f}{e}\frac{\partial u}{\partial y} = 0 \quad , \quad v = V/R \quad \text{and} \quad w = 1 \qquad (3\text{-}14)$$

The finite difference scheme developed to solve equations (3-7) through (3-10) subject to the boundary conditions above is discussed in a later section.

3.3 Exploratory Calculations

To obtain a numerical solution for vortex breakdown several approaches, briefly described in the following paragraphs, were explored. Each provided essential information and experience without which the final scheme used to obtain the solution presented later in this report could not have been developed.

Initially an explicit finite difference scheme with simple programming was constructed. However, instead of (3-5) and (3-6), the transformation

$$x = \frac{\ln (1 + b z)}{b z}$$

$$y = \frac{c r}{1 + c r}$$

was applied. This was used to map the infinite region $0 \leq r < \infty$, $0 \leq z < \infty$ onto $0 \leq y \leq 1$, $0 \leq x \leq 1$ so that conditions $u = 0$, $v = 0$, and $w = 1$, which apply as r and z approach infinity could be used at the boundaries of the transformed region without approximation. The form of the z to x transformation was chosen to match, in the sense that singularities are avoided, the asymptotic solution of Batchelor (1964) for a viscous trailing vortex. The r to y transformation was chosen for its easy inversion. The resulting transformed auxiliary equation, which, except for the definitions of the coefficients f, g, etc., are almost identical to (3-7) through (3-10), were solved by an explicit scheme which used centered differences for the diffusion and pressure terms, forward differencing for t, and first-order upwind differencing for the convection terms. These initial coarse grid calculations established the possibility of obtaining and studying a vortex breakdown numerically at Reynolds numbers sufficiently low for finite difference solutions to be meaningful.

In order that solutions might be obtained more efficiently other finite difference methods were considered and an implicit scheme based on the alternating-direction implicit (ADI) method of Peaceman and Rachford (1955) was eventually selected.

This scheme was significantly faster. Time steps much larger than possible with the explicit scheme could be used, easily compensating for the extra computational labor involved. Initially all spatial derivatives were approximated by centered differences, but experiments, even with a fine mesh spacing, 61 points in the x-direction and 31 in the y-direction, demonstrated that only solutions for very low Reynolds numbers (< 50) could be obtained. However, by applying upwind differencing for $x > 2/3$, flows at $Re = 100$ could be calculated. Higher Reynolds number flows required upwind differencing everywhere. Fully aware that there could be significant errors due to the large numerical viscosity introduced by upwind differencing, calculations were performed for Reynolds numbers from 100 to 1000. These computations later proved essential in providing estimates for the approximate location of breakdown, the breakdown bubble's radius and length, and the magnitude of the reversed axial flow in the bubble.

The reason only extremely low Reynolds number flows could be obtained without upwind differencing is apparent. While the grid spacing in the transformed (x,y) plane could be made arbitrarily small through the use of an increased number of grid points, the grid spacing as it would appear in the r-z plane always becomes very large and eventually infinite as x and y approach one. Letting h_r represent the mesh spacing in the r-z plane, the criterion

$$Re\, h_r = O(1)$$

which has been claimed to be a necessary condition for a numerical solution (Dennis and Cheng, 1969; Chorin, 1972), will always be violated for large r and z. A similar criterion for a solution in x-y space is obtained by letting h represent the fixed grid spacing in that space. Then

$$\frac{h}{h_r} = \frac{\Delta x}{\Delta z} \approx \frac{dx}{dz}$$

and since dx/dz = s(x), the coefficient of the transformed equation defined in Chapter 2,

$$h_r \approx \frac{h}{s} \quad .$$

Therefore, the condition

$$Re \frac{h}{s} = 0(1)$$

must be satisfied. As x approaches one, s approaches zero and this criterion is violated. For the Re = 50 case mentioned above, the violation occurs at a small number of downstream grid locations, and apparently a solution could still be obtained. For Re = 100, however, violation was more widespread, and a solution could only be obtained by using upwind differencing for x > 2/3 which, in effect, lowered the Reynolds number in that region with the introduction of numerical viscosity.

An examination of the solutions obtained in these calculations suggested that approximations could be made at finite r and z. Boundary conditions could then be formulated for a finite region in r-z space, while allowing a solution to be obtained for an unconfined flow. Use of such a finite domain was expected to avoid the mesh width difficulties explained above, and to allow the calculation of accurate solutions at higher Reynolds numbers than possible in the infinite domain. The finite domain model of

Section 2.2 and the finite transformation presented in 3.2 were then developed.

3.4 The Finite Difference Scheme

An ADI scheme similar to that described in the previous section for the infinite domain calculations was used to obtain steady solutions of (3-7), (3-8), (3-9) and (3-10), subject to the boundary conditions (3-11) through (3-14), for a wide range of the parameters Re, α, and V. The scheme, including treatment of the boundary conditions, is presented in detail in Appendix B. Centered differences were used for all spatial derivatives including convection terms, so that no numerical viscosity was introduced. A staggered grid system, which was used to increase the accuracy of the scheme and to avoid the necessity of calculating pressure at the boundaries, is also described in the appendix. The spatial truncation error of the scheme is $O(\Delta x^2) + O(\Delta y^2)$ and, except for the effects of first order approximations for the derivative boundary conditions, solutions are of the same order.

The location of the radial and downstream boundaries, $r = R$ and $z = L$, were determined in the following manner. Estimates were first obtained from an examination of the results of the infinite domain calcaulations at Re = 100. Then, using a grid system with 61 points in the x-direction, 31 points in the y-direction, and 12 points in the intervals $0 \leq r \leq 1$, $0 \leq z \leq 1$, solutions with various values of R and L, based on the estimated values, were obtained. These solutions demonstrated that R could be safely set at 10 and L at 20 since the use of larger values did not significantly change the solutions, and, also, since a comparison of these solutions with those obtained in the infinite domain showed very good agreement. Such a comparison is presented in Fig. 4 for the axial velocity on the axis versus z.

Numerical experiments which varied δ in the hope of obtaining an optimum value demonstrated that larger values of δ permitted longer time steps, while shorter steps were required for smaller δ. This behavior was predicted by Chorin. Very long time steps based on large values of δ did not permit stable calculations to convergence, probably due to the timewise linearization of the convection terms in the finite difference momentum equations. Eventually, δ was set equal to one, and a time step of length 0.11 was then used in all calculations.

Computations were run to convergence, defined as changes in velocities less than 0.0005 over 100 time steps with the 61 x 31 grid system explained above. This required from two to four thousand time steps, depending on the particular case and initial conditions. This rather large number of time steps resulted from the quite complicated three dimensional dynamics of the flow in vortex breakdown. When possible, the initial condition of any computation was a solution from a previous computation with values of Re, α, and V close to those of the case being considered. This was most efficient, saving as many as 1500 time steps, for fixed Re and α, as V was varied from low to high values. Each computation required from two to four minutes of computer time on the Lawrence Berkeley Laboratory CDC 7600 when compiled with the CDC FTN optimizing compiler. Graphical output was disposed to both microfiche and 35mm film, from which many of the figures presented later in this report were obtained.

4.0 RESULTS AND DISCUSSION

4.1 Preliminary Comments

A total of 39 solutions with various combinations of Re, α, and V were obtained. The combinations, which are summarized in Table 1, were chosen with the intent that each solution should be as informative as possible, and that the net effect of all the solutions should be to provide a comparison of the several existing theories of vortex breakdown with quantitative results.

It should be noted prior to a discussion of the solutions that centered differencing of all spatial derivatives was used for computations with Reynolds numbers up to 200. Solutions at higher Reynolds numbers, which were obtained for qualitative purposes only, required upwind differencing for the convection terms in the momentum equations and, therefore, a slight modification of the program described in the previous chapter.

4.2 Solutions for Vortex Flow

The development of a vortex breakdown, in terms of a sequence of steady state solutions with increasing amounts of swirl will be described in this section. These solutions were all obtained with $Re = 200$, $\alpha = 1$ so that the axial velocity distribution at $z = 0$ was uniform. Calculations were performed with V set at 0.63, 0.80, 0.85, 0.894, 1.0, and 1.095. In most cases, little of interest occurs outside the region $0 \leq r \leq 2$, $0 \leq z \leq 6$, which is a small part of the domain $0 \leq r \leq 10$, $0 \leq z \leq 20$, in which the solutions have been obtained. Therefore, most of the figures to be presented will display, in detail, various aspects of the solutions in this small region only.

Figure 5a shows a contour plot for a number of constant values of the Stokes stream function, ψ, defined by

$$\psi = \int^{(r,z)} r(w\,dz - u\,dr)$$

where the line integral is taken along an arbitrary curve in an axial plane joining a reference point where $\psi = 0$ to the point (r,z) (Batchelor, 1970). ψ was computed at each grid point by simple numerical integration of the velocities from the solution obtained with $V = 0.63$. Each contour represents a stream surface and, since the flow is steady, a fluid particle entering the domain at $z = 0$ proceeds downstream spiralling along the stream surface on which it enters. Plots of other aspects of this solution are presented in Figs. 5b through 5g.

Figure 5b displays axial velocity profiles at a number of axial locations, and Fig. 5c shows the variation of the axial velocity at several values of r with distance downstream. The slight retardation of the axial velocity within the core reduces the axial velocity at $r = 0$ to about 0.80 at $z = 6$.

Figure 5d shows swirl velocity profiles at the same axial locations chosen for Fig. 5b, and Fig. 5e displays the variation of the swirl velocity with z at the same radial positions plotted in Fig. 5c. The swirl velocity at $r = 0$ is always zero and not labeled in Fig. 5e. A reduction in the swirl velocities in the core due to the diffusion of vorticity away from the axis is evident in these figures. For example, the velocity at $r = 0.486$ decreases from 0.55 at $z = 0$ to 0.48 at $z = 6$.

It should be noted that the changing velocity field, as

Morton (1969) has pointed out, associated with vorticity diffusion, is due to a stress distribution which, in effect, transmits inward a retarding torque resulting from the non-zero circulation at radial infinity. The angular momentum of a disk of fluid of unit thickness, concentric with the axis, will, therefore, decrease with z. This may be clearly demonstrated by integrating the angular momentum equation (2-2), from $r = 0$ to $r = r^*$, where $r^* \geq r_c$, to obtain, after rearrangement

$$\frac{d}{dz} \int_0^{r^*} (w\,v - \frac{1}{Re} \frac{\partial v}{\partial z})\, r\, dr = - (u\, r)_{r^*}\, \Gamma - \frac{2\Gamma}{Re} \qquad (4\text{-}1)$$

where Γ is the fixed constant circulation outside the core. The angular momentum flux along a cylinder of radius r^* is, therefore, not fixed but increases due to entrainment of fluid from the exterior of the cylinder, and decreases due to the effect of a torque at r^*, and, although the angular momentum of the disk becomes infinite as r^* approaches infinity, it must still decrease at a finite rate with z since $(ur)_{r^*=\infty}$ does not, in general, vanish. The flux of angular momentum, therefore, is not constant in vortex flows.

Figure 5f presents the variation with z of three quantities: the pressure, p_c, along the row of staggered grid points nearest the axis; the radius of the vortex core, r_c, which has been defined here as the cylindrical region, concentric with the axis around which the circulation is 0.95 V; and the maximum swirl velocity in the core, V_{max}. Note that since the pressure within the core will be less than the ambient pressure, the non-dimensional pressure $(p-p_\infty)/\rho w_\infty^2$ will always be less than zero. In this case p_c varies very slowly with z, increasing from about -0.63 at $z = 0$ to -0.50 at $z = 6$. Diffusion of vorticity away from the axis is responsible for both the increase of the core radius from about 0.90 at $z = 0$ to 1.20 at $z = 6$, and the reduction of the maximum swirl velocity from 0.69 to about 0.57.

The axial velocity decrease within the core, noted above, may now be explained. As vorticity diffuses beyond the initial core radius, the swirl velocity of a particle of fluid near the axis will decrease. The radial pressure gradient required to balance the centrifugal acceleration of the particle must, therefore, also decrease. This reduction is obtained through the increase in the pressure near the center of the core, displayed in Fig. 5f. The axial flow near the axis, encountering a small adverse gradient of pressure is, therefore, slightly retarded.

The above argument may be demonstrated analytically using the approximation

$$\frac{\partial p}{\partial r} = \rho \frac{v^2}{r} \tag{4-2}$$

which expresses the balance of a particle's centrifugal acceleration with the restraining pressure force. This equation is exact only for slowly expanding cores in the limit of high Reynolds numbers, and forms part of the "quasi-cylindrical" approximation of the Navier-Stokes equations which is valid for such conditions (Gartshore, 1963; Hall, 1966; Bossel, 1967). Integration with respect to r from the axis to radial infinity followed by differentiation with respect to z, yields

$$\frac{\partial p_0}{\partial z} = -\rho \int_0^\infty \frac{v}{r} \frac{\partial v}{\partial z} dr$$

where p_0 is the pressure at the center of the core. Since v is always positive, and viscous dissipation of swirl makes $\partial v/\partial z < 0$ there results a positive axial pressure gradient at the axis, and thus the retardation of the axial flow near the axis.

Figure 5g shows the axial velocity at the axis for the entire length of the computational domain. The deceleration of the axial flow does not continue indefinitely. As v and $-\partial v/\partial z$ decrease, the rate of change of the pressure will also decrease so that the adverse pressure gradient becomes smaller with z. This behavior is predicted by equation (4-2). Viscous forces are then able to overcome the pressure gradient and accelerate the fluid, eventually to the free stream axial velocity.

The solution obtained with $V = 0.80$ is displayed in Figs. 6a through 6g.

A slight expansion of the stream surfaces in Fig. 6a is barely apparent so that the solution seems little different from that obtained with $V = 0.63$. However, the deceleration of the axial flow in the core (Figs. 6b and c) is much more pronounced with the velocity at $r = 0$, for example, decreasing to 0.55 at $z = 6$. Also more pronounced is the rate at which the swirl velocities (Figs. 6d and e) decrease with z. The swirl at $r = 0.486$ decreases from 0.70 at $z = 0$ to 0.41 at $z = 6$. This increased rate of swirl velocity decrease is due to the increased concentration of vorticity near the axis, which results

results in more rapid diffusion. In terms of the shear stress distribution, τ_{r_θ} at $z = 0$ is equal to $-2\mu Vr^2$ so that the torque applied to a disk of fluid is of unit thickness, for $r \leq 1$, $-4\pi\mu Vr^4$, directly proportional to V.

Using, once again, the notion of a balance between the centrifugal acceleration of fluid particles and the radial pressure gradient, the increased rate of swirl reduction with z must be supported by a more rapidly increasing pressure on the axis. Since v and $-\partial v/\partial z$ are larger than in the previous case, $\partial p_0/\partial z$ must also be larger. Comparison of 6f with 5f shows the difference in the pressure variation. For $V = 0.63$ the pressure varies only very slowly with z, while for $V = 0.80$ the pressure, which initially must be lower to provide the larger radial pressure gradient required for the increased swirl, shows a much more rapid rise, increasing from -1.03 at $z = 0$ to -0.63 at $z = 6$. The more pronounced retardation of the axial velocity noted above corresponds to this larger adverse pressure gradient.

Figure 6f also displays the increasing core radius and the decreasing maximum swirl velocity in the core. Figure 6g shows that the axial velocity decreases to a minimum of about 0.5 before shear forces begin the acceleration which will eventually result in a uniform axial flow infinitely far downstream.

Increasing V from 0.80 to 0.85 results in the solution presented in Figs. 7a through 7g. The stream surface expansion (Fig. 7a) is now clearly evident. The radii of the surfaces near the axis reach a maximum at about $z = 5$, and the axial velocity on the axis (Figs. 7b and c) is quickly decelerated to a minimum of 0.25 also near $z = 5$. The swirl velocity in the core (Figs. 7d and e) after decreasing initially in a manner very similar to the previous cases, reaches a minimum near $z = 5$, where, for example, the velocity at $r = 0.486$ is 0.28, and then begins to increase. The acceleration of the swirl velocity near the center of the core continues for a short distance, then, although not shown in Fig. 7e, gives way to a final deceleration, which eventually will lead to total dissipation. Figure 7f shows that after a rapid initial increase, the pressure reaches a constant value, -0.57, and begins to decrease slightly, also near $z = 5$.

The dynamic situation may be explained as follows. A fluid particle enters the domain at $z = 0$ close to the axis with axial velocity and angular momentum. As it proceeds downstream, shear forces reduce its angular momentum and, as explained previously, this is associated with an adverse gradient of pressure which acts to decrease the axial velocity of the particle. However, since both v and $-\partial v/\partial z$ are initially larger than the previous cases, the amount of retardation of the axial flow is also larger, and continuity requires that a significant amount of fluid move radially outward. This movement is apparent in the stream surface plot. Then, since, except for viscous effects the angular momentum of the fluid particle is conserved as it moves radially, its angular velocity must decrease. Figure 7d illustrates this behavior. As z increases from zero to about 5, the swirl velocity at any radial position is that of a fluid particle which has originated at some position closer to the axis. The effect of this is the development of a slowly rotating region on the axis apparent from about $z = 4$. For z less than about 3, the reduction of swirl due to the radial outflow explained above requires, when combined with viscous effects, a much larger increase in the pressure at the axis. This is clearly seen in Figure 7f. For larger z, however, since v and $\partial v/\partial z$ are very small near the axis, the adverse pressure gradient also becomes small, and shear forces are then able to accelerate the axial flow near the center of the core (Fig. 7c). Continuity then requires an inward motion of fluid toward the axis, and, again assuming angular momentum conservation for a particle, the increase in the angular velocity at radial psoitions, displayed on Fig. 7e, must occur. The increasing angular velocity near the axis requires that the pressure on the axis decrease slightly, as may be seen in Fig. 7f at $z = 6$. Beyond this point the pressure continues to slowly decrease until approximately $z = 7.5$, assisting the shear forces in accelerating the axial flow (see Fig. 7g). Then the effect of viscous diffusion once again becomes significant, reducing the swirl velocities near the axis and leading to an adverse pressure gradient which decreases the rate of acceleration of the axial velocity. This is apparent in Fig. 7g from about $z = 7$ to 8. As in previous cases, however, this adverse gradient decreases with z as v and $-\partial v/\partial z$ decrease so that the axial velocity will eventually be accelerated by shear forces to the free stream velocity.

The solution obtained with $V = 0.8944$ is presented in Figs. 8a through 8g. A small, well-developed bulge in the stream surface near $z = 3$ is readily apparent in Fig. 8a. Similar stream surface expansions were obtained experimentally by Sarpkaya (1971), and analytically by Bossel (1967) for flow conditions close to those for which his integral analysis of the quasi-cylindrical equation failed.

The axial velocity devrease (Figs. 8b and c) in the core is considerably more rapid than those enouuntered in the previous cases, and nearly results in stagnation at $z = 3$ where the axial velocity on the axis reaches a minimum of 0.02. The acceleration, then deceleration of fluid outside the core as it passes over the bulge may be detected in Fig. 8b, and is seen clearly at $r = 1$ in Fig. 8c.

The swirl velocity profiles (Figs. 8d and e) show, as in the previous case, the decrease in the swirl velocity due to shear stress and, especially, the reduction induced by the stream surface expansion. The reduction near the axis is particularly substantial. As Fig. 8c demonstrates, the swirl velocity at $r = 0.486$ decreases from 0.77 at $z = 0$ to 0.20 at $z = 3$.

As shown in Fig. 8f, the pressure increases steeply from -1.21 at $z = 0$ to -0.76 at $z = 2$, and then becomes essentially constant within the bulge region, $2 \leq z \leq 4$, with a value of about -0.65. The contraction of the stream surfaces, begun by shear forces near the axis, as explained previously, then causes the pressure to decrease to -0.72 at $z = 5.5$ as the angular velocity of fluid near the axis increases. Viscous effects, however, begin to decrease the swirl velocity and, once again, an increasing pressure near the axis is required.

Also displayed in Fig. 8f is the rapid increase in r_c

between $z = 2$ and 3, which is due in the most part to radial convection of vorticity; and, the sharp decrease in V_{max} from 0.96 at $z = 1$ to 0.77 at $z = 3$.

Figure 8g presents the variation of axial velocity on the axis. The initial decrease, as explained above, is due to the large adverse pressure gradient, and the acceleration which begins at $z = 2$ is initially due to shear forces but given assistance, beginning at about $z = 4$, by a favorable pressure gradient. The second deceleration, beginning at about $z = 5.5$, is the result of the second adverse pressure gradient and the following acceleration is due to the effect of shear forces as this gradient decreases.

Figures 9a through 9g display a vortex breakdown obtained with $V = 1.0$. The small stream surface surface bulge of the previous solution has developed into a closed bubble of recirculating fluid, similar in shape to some of those obtained by Sarpkaya (1971a). The stream surfaces within the bubble have small negative values. The outer stream surfaces, after expanding over the bubble, neck down behind it, and expand slightly again.

The axial velocity plots (Figs. 9b and c) show the very rapid deceleration near the axis upstream of the bubble. w at $r = 0$ reaches a minimum of -0.082 at $z = 1.64$, then increases to 0.359 at $z = 3.62$. A second deceleration reduces the velocity to 0.176 at $z = 5.16$, where it begins its gradual return to free stream conditions (Fig. 9g). Clear in both Figs. 9b and 9c is the acceleration of fluid outside the core as it passes over the bubble.

Figures 9d and 9e demonstrate that due to the stream surface expansion the swirl velocities within and near the bubble are very small. At $r = 0.486$, for example, the swirl decreases from 0.86 initially to 0.124 at $z = 1.78$, before increasing to 0.53 at $z = 3.96$ due to the stream surface contraction behind the bubble.

Figure 9f shows a very steep increase in the pressure near the axis ahead of the bubble. The pressure near the axis within the bubble is essentially constant, however, due to the very slow rotational speeds mentioned above. As in the previous cases, the stream surface contraction results in a pressure decrease, beginning at $z = 1.78$, which assists the acceleration of the axial velocity. Beyond $z = 3.6$, the pressure begins to increase with the dissipation of swirl due to shear stresses.

The solution for a large, more vigorous breakdown, obtained with $V = 1.095$, is displayed in Figs. 10a through 10g.

The bubble, as shown in Fig. 10a, is larger than the previous case and has moved further upstream. The stream surface expansion around the bubble is now very rapid, and the contraction behind the bubble is followed by a second pronounced expansion, beginning at about $z = 3$. The near entrainment into the bubble of the stream surface closest to the axis should especially be noted. Sarpkaya (1971a) reported that fluid did not enter through the front of his experimentally obtained bubble, but instead passed over it and entered from the back. Then, after mixing turbulently inside, fluid exited into a second core-like region behind the bubble. While turbulent mixing has not, of course, been included in this study, the similarity between Fig. 8a and his photographs is striking.

Further comparison of Fig. 8a with Sarpkaya's photographs suggests that the second expansion might be the axisymmetric counterpart to the spiral breakdown which is always found, experimentally, behind an axisymmetric breakdown. If the flow in this second expansion were unstable to spiral disturbances, which of course do not exist in these numerical solutions, such a spiralling breakdown might then develop. This hypothesis will be discussed in somewhat more detail in a later section.

Figures 10b through 10g show that the solution differs from those previously discussed in some interesting respects.

An increased rate of deceleration of the axial flow compared to the previous case is apparent in Figs. 10b and 10c although the minimum velocity attained, -0.036 is somewhat larger. Also, the axial velocity on the axis is reversed for a shorter distance than before.

The swirl velocity near the axis (Figs. 10d and 10e) shows a more rapid decrease with z, which corresponds to the more rapid stream tube expansion. The bubble is clearly (Fig. 10d) a region of very slow rotation despite the very large initial swirl.

Figure 10f displays the very large initial pressure gradient and, as in the previous case, the almost constant pressure in the bulge, which is followed by a decrease due to the stream surface contraction. Also, displayed in Fig. 10f are the core radius, which increases rapidly for small z due to outward radial convection of vorticity, then decreases slightly due to inward convection during the contraction, and V_{max}, which decreases quickly due to the stream surface expansion.

Following the discussions of the next two sections, which deal with the solutions presented here, solutions for other values of α, V, and Re will be discussed.

4.3 The Effect of Swirl

It is clear from the solutions presented in the previous section that the appearance in a vortex core of a large adverse pressure gradient, with a corresponding large decrease in axial velocity, is critically dependent on the magnitude of the swirl which is introduced at $z = 0$. Figure 11 has been prepared to quantify this dependence. It shows the minimum axial velocity, W_m, attained on the axis versus V for each of the solutions. The dashed trend curve represents a graphic extrapolation of the solutions to small values of V. As V increases from zero, where no axial retardation will occur, dW_m/dV becomes increasingly negative so that for small V, small changes in V yield only small changes in W_m, but for larger V, particularly near $V = 0.80$, small changes in V yield very large changes in W_m, as may be seen in the figure. An explanation of this highly non-linear behavior may be as follows.

For small values of V, the effect of swirl dissipation is to increase the pressure on the axis and thus cause a small amount of axial flow retardation. The small radial flux away from the axis which is required by continuity, has, however, little little effect on the swirl velocity distribution. The swirl velocity field is, therefore, essentially decoupled from the rest of the flow field and affects it only through the small adverse pressure gradient. For larger amounts of swirl, however, this decoupling is no longer possible. The axial velocity retardation arising from viscous dissipation of the swirl is large enough to require a significant amount of radial outflow, and, as explained in the previous section, this decreases the swirl velocities near the axis, and thus supports a very much larger adverse pressure gradient and an increased reduction of the axial velocity. The very large negative value of dW_m/dV which occurs at about $V = 0.8$ for the values of α and Re of these solutions is, therefore, due to the coupling, as V increases, of the initially decoupled swirl velocity field with the rest of the flow field.

4.4 Comparisons with Experiments and Theory

Before considering other solutions of the equations for breakdown, it is worth comparing the previously discussed solutions with experimental observation and the theoretical explanations described in Chapter 1.

As pointed out earlier, there is very little experimental data regarding vortex breakdown. The quantitative information which does exist has, for the most part, been obtained from photographs taken of flows, after the introduction of dye or smoke. In this way Harvey found that the swirl angle, $\phi \equiv \tan^{-1}(v/w)$, ahead of his breakdowns was never larger than 50.5°, and in a similar experiment Sarpkaya (1971a) found that it was never larger than 51°. Theoretical predictions of ϕ, based on the finite transition concept, vary from 45° (Squire, 1960) to 62.5° (Bossel, 1967), depending on the velocity profiles chosen for analysis. This is a considerable range of variation, particularly since the maximum value of v/w, from which ϕ is obtained, varies, therefore, from 1.0 to 1.88.

The maximum swirl angle at $z = 0$ of the solutions discussed in Section 4.2 varied from 34.38° to 49.95° (see Table 2), and was 44.17° in the solution obtained with $V = 0.8944$ in which the axial flow almost stagnated. There is, therefore, reasonable agreement in terms of the swirl angle between the experimental evidence, theoretical predictions, and the numerical solutions.

It should be noted that Mager (1972) substituted the initial velocity profiles used in his analysis and in this study, into Benjamin's test equation for criticality and solved it with various combinations of α and V. He was then able to divide an α-V^2 plane into supercritical and subcritical regimes. Based on his results, the upstream conditions for all the numerical solutions presented thus far are supercritical, as required by the finite transition theory for breakdown to occur.

The second theoretical explanation reviewed in Chapter 1, that breakdown is the result of a hydrodynamic instability to a spiral disturbance, is obviously irrelevant since no such disturbances exist in these axisymmetric calculations. As mentioned in Section 4.2 and also by Hall (1972), such an instability may determine, however, which type of breakdown, spiral or axisymmetric, occurs in experiment.

The third theoretical approach to breakdown, that it is a swparation-like phenomenon, predicted by the failure of the quasi-cylindrical approximation, must also be considered. Mager (1972) provided a very precise criterion for the appearance of discontinuities, which he assumed were the results of such failures, in his integral solutions of the quasi-cylindrical equations. He defined a parameter θ_1 which is the invariant flux of axial momentum deficiency in the core plus a term dependent on the circulation around the core plus a third term whose value changes only behind the breakdown. θ_1 is determined from the upstream condition, and depends in no way on the super- or subcriticality of these conditions. In general increasing α decreases θ_1, since the axial momentum flux is then larger, while increasing V increases θ_1, since the pressure deficit in the core is then larger. Mager then showed that if the initial conditions, as determined from the values of α and V, are such that θ_1 is less than a certain value, θ_1^*, then there is a continuous solution. If, however, $\theta_1 > \theta_1^*$, discontinuities will arise, marked by the appearance of infinite gradients regardless of the sub- or supercriticality of the upstream flow. He determined that $\theta_1^* = -0.163989$.

Values of θ_1, for all the solutions of Section 4.2, are shown in Table 2. From the discussion of Section 4.2 it is apparent that flow reversal in the numerical solutions corresponds to a value of θ_1 slightly larger than -0.056, which is significantly larger than θ_1^*. There are a number of possible explanations for this difference. First, it is not clear that the failure of the quasi-cylindrical equations requires fully reversed flow, since such a failure represents only the inability of the approximation to deal with large axial gradients, and, as noted in Section 4.2, large gradients do appear in solutions which do not exhibit stagnation.

θ_1^* could then possibly be a good deal less than the θ_1 required for flow reversal, as is the case in these solutions. Second, Mager's assumed profiles may not be general enough to describe the flow approaching breakdown. This is a possibility, as noted by Hall (1972), in all integral formulations. Third, and most obvious, Mager's result applies to high Reynolds number flows and 200 is, at best, only moderate.

If θ_1 is, however, the essential parameter, the occurrence of breakdown should be independent, except for Reynolds number effects, of the particular values chosen for α and V, and depend only on the value of θ_1. Also, if the theoretical explanation proposed in the first chapter, that breakdown is a result of initially supercritical or subcritical flows approaching a critical state in which very large axial gradients develop, is to be demonstrated, breakdowns in initially subcritical flows must be obtained. These ideas were important in the choice of which other solutions would be obtained.

4.5 Other Solutions

Several solutions for $Re = 200$ not described in Section 4.2 are displayed in Figs. 12 through 18. These solutions are, in most respects, quite similar to those previously discussed.

Figures 12 and 13 show the stream surfaces for two solutions with $\alpha = 0.3$. Since α is very small, the axial momentum of the flow near the axis will also be small, so that the adverse pressure gradient which develops as a result of swirl dissipation need not be very large to produce stagnation. The solution with $V = 0.8944$, therefore, exhibits reversed flow (Fig. 13), while that with the same swirl but at $\alpha = 1$, discussed previously (Fig. 8) did not. It should also be noted that this solution results from upstream conditions which are subcritical. The appearance of breakdown in subcritical flows, as required by the proposed explanation discussed previously, is thus demonstrated.

Solutions obtained with $\alpha = 0.6$ and $V = 0.82$, 0.8944, and 1.095 are shown in Figures 14, 15, and 16. While the solution for $V = 0.85$ and $\alpha = 1$ discussed previously showed only very slight stream surface expansion, the expansion is quite pronounced for $V = 0.82$ (Fig. 14), and as with $\alpha = 0.3$, setting V to 0.8944 is sufficient to produce reversed flow (Fig. 15). Figure 16a displays stream surfaces obtained from the solution with $V = 1.095$ for which the upstream conditions were again subcritical. The second retardation of the axial flow (Fig. 16b), which always appears in solutions with large swirl velocities, is, in this case, sufficient to produce stagnation and a second reversed flow region.

Figures 17 and 18 show solutions obtained with $\alpha = 1.4$, and it is apparent that V in excess of 0.95 is required for flow reversal. In this case, the axial momentum of the flow near the axis is very large and, therefore, a very strong adverse pressure gradient, which will exist only for large values of V, is required to produce stagnation.

Attempts were made to obtain solutions for α greater than 1.4. These invariably failed for values of V large enough to be of interest in this study. Also, solutions with V greater than about 1.2 for $\alpha = 1$, which were desired to study further flows with high swirl, failed. These failures were probably due to an incorrect scaling of the equations for flows with high swirl or large axial velocity excesses. For flows in which α or V are large, the core Reynolds number based on the free stream axial velocity may not be a very good estimate of the ratio of convection to diffusion transport. A more appropriate characteristic velocity would have been based on some maximum velocity, for example, $\sqrt{\alpha^2 + V^2}$. Then instead of requiring

$$Re \frac{h}{s} \sim 0(1)$$

for a numerical solution we would require

$$\frac{Re \sqrt{\alpha^2 + V^2}}{W_\infty} \frac{h}{s} \sim 0(1)$$

where Re is the core Reynolds number defined previously. This suggested that flows with high values of α and V could only be obtained with a smaller core Reynolds number.

Several of the solutions obtained with $Re = 100$, and $\alpha = 1$ are presented in Figures 19, 20, and 21.

With $V = 0.8944$, the axial flow retardation produced the very slight stream surface expansion seen in Fig. 19a. This figure and Fig. 19b, which shows the variation of w on the axis, should be compared with Figs. 8a and 8g, which were obtained from the solution with identical α and V, but $Re = 200$. The larger shear forces, corresponding to the smaller Reynolds number, which develop when the axial flow near the axis is retarded, require a stronger adverse pressure gradient to cause stagnation. Figures 20a and b show a well-developed breakdown obtained with

$V = 1.095$. Although higher initial swirl velocities are required, breakdown will still occur at this low Reynolds number.

Figure 21a shows a breakdown obtained with subcritical upstream conditions in a very high swirl flow, with $V = 1.342$. The breakdown bubble is very large, and is followed by a low velocity region (Fig. 21b) in which a second reversal occurs. This rather large low velocity region may be an early stage in the development of a very large scale flow reversal similar to that obtained by Harvey (1962) in a vortex tube and mentioned in Section 1.2.

4.6 Discussion

Figure 22 shows the dependence of the minimum velocity on the axis, W_m, on V for all solutions obtained with $Re = 200$. Figure 11 displayed the case of $\alpha = 1$ only. Solutions for which $W_m \leq 0$ necessarily represent flows in which breakdown has occurred. The data points for equal values of α fall roughly into bands so that, in general, as α increases larger values of V are required to yield a given minimum velocity. As pointed out in the previous section, this behavior is due to the dependence of the axial momentum of the flow near the axis, which must overcome an adverse pressure gradient, on α. The two $\alpha = 0.3$ data points for $V = 0.55$ and 0.63 both represent solutions in which W_m was a minimum at $z = 0$, and, therefore, equal to α. There was no retardation in these two cases since the large viscous forces at $z = 0$ easily overcame the adverse pressure gradient developing downstream.

Figure 23 is a plot of W_m versus the maximum swirl angle, ϕ, at $z = 0$ for the same solutions. As above, the data points fall into bands for equal values of α so that as α increases a given value of W_m corresponds to increasing values of ϕ. For convenience define ϕ^* as the value of ϕ at which $W_m = 0$ for each value of α. Then second order interpolation yields $\phi^* = 42.5°$, $43.0°$, $44.4°$, and $47.2°$ for $\alpha = 0.3$, 0.6, 1.0, and 1.4, respectively. The asymptotic nature of the variation of ϕ^* with α as α becomes small, which may be easily demonstrated by computing $\Delta\phi^*/\Delta\alpha$ for each of the three α intervals, suggests that there exists a minimum value of ϕ^* such that for $\phi < \phi^*$ breakdown will not occur even for very small values of α.

Figure 24 shows a point of W_m versus θ_1. The collapse of the data, except for the two $\alpha = 0.3$ cases which should be ignored since in those solutions no retardation at all took place, is particularly striking. For all values of α, the value of θ_1 corresponding to $W_m = 0$, which may be defined as $\tilde{\theta}_1$, is very close to -0.05. θ_1, therefore, gives a very good indication of the occurrence of breakdown. When $\theta_1 < \tilde{\theta}_1$ no breakdown occurs and, in contrast with the swirl angle, when $\theta_1 > \tilde{\theta}_1$ breakdown necessarily occurs regardless of the value of α.

The appearance of a critical value of θ_1 at which breakdown will occur is in agreement with the quasi-cylindrical theory of Mager (1972) discussed in Section 4.4, as is the relationships between W_m and θ_1 implied by the data collapse.

Figure 25 is a plot of W_m versus θ_1 for solution with $Re = 100$. The data again collapse onto a single curve. The amount of scatter in the data is less than in the previous figure, perhaps since solutions at this lower Reynolds number will tend to be more accurate. It is clear from the figure that $\tilde{\theta}_1 \approx 0.01$ for $Re = 100$, which suggests that $\tilde{\theta}_1$ is a decreasing function of Reynolds number, in which case it could possibly approach Mager's θ_1^* for very high Reynolds numbers. This is, however, only a hypothesis which, due to the difficulty of obtaining solutions for high Reynolds number flows, cannot be substantiated. Also, as pointed out earlier, θ_1^* is the value of θ_1 at which large axial gradients will occur, and not necessarily the value for which reversed flow results. Therefore, even at high Reynolds numbers, $\tilde{\theta}_1$ might be larger than θ_1^* and, thus, closer to the values predicted from these numerical solutions.

Figures 26 and 27 show a comparison for several Reynolds numbers of w at $r = 0$ versus z for $\alpha = 1$, and $V = 0.63$ and 0.8944. The solutions at $Re = 500$ and 1000 were, as previously mentioned, obtained using upwind differencing and are, at best, only suggestive of the actual flows.

Figure 26 shows that the very mild retardation in the solution with $Re = 200$, $\alpha = 1$, and $V = 0.63$, discussed in Section 4.2, becomes slightly more pronounced for decreasing Re and less pronounced as Re increases. This is in accord with the integral analyses of both Gartshore (1962,1963) and Mager (1972) in which Re enters in the solution only as a scale factor for z. Figure 27, however, shows that solutions which exhibit breakdown at small values of Re should continue to do so as Re is increased. It is expected, therefore, that, while this study has obtained quantitative information for moderate Reynolds numbers only, the conclusions reached here can be extended to higher Reynolds number flows.

Regarding the applicability of Benjamin's finite transition theory, it must be noted that as mentioned before the solutions for $Re = 200$, $\alpha = 0.3$, $V = 0.8944$; $Re = 200$, $\alpha = 0.6$, $V = 1.095$; and $Re = 100$, $\alpha = 1$, $V = 1.342$, which are displayed in Figs. 13, 16, and 21, all exhibited breakdown with initial conditions which, based on Mager's analysis, were subcritical. The finite transition theory, however, requires that a vortex flow be supercritical before breakdown occurs, so that the numerical solutions suggest that the theory does not fully account for viscous vortex breakdown.

In order to explain the appearance of an axisymmetric bubble followed by a spiral breakdown in highly swirling flows, and the appearance of only the spiral in flows with less swirl, Mager included the finite transition in his quasi-cylindrical analysis. He argued that the finite transition was a cross-over, ahead of the discontinuity, of the solution to a different branch of the solution curve with the same value of θ_1; and, that the discontinuity appears in the experiment as the spiral breakdown, while the cross-over, if it occurs, appears as the axisymmetric bubble. This argument, however, cannot explain the existence in Harvey's (1962) experiment of two axisymmetric breakdowns followed by a spiral in a steady flow, and the appearance, in Sarpkaya's (1972a) experiment, of similar phenomena in an unsteady flow.

Based on the numerical solutions obtained in this study, and on the observations of Sarpkaya (1972a,b), the following possible explanation of the various forms of vortex breakdown is proposed.

In flows in which the swirl velocities are not large, the axial retardation, which results from diffusion of vorticity and occurs in all viscous vortex flows, may be such as to produce a region in the vortex core in which the flow is unstable to certain spiral disturbances. The introduction of such a disturbance would then result in the development of a spiral breakdown. Sarpkaya (1971b) has, in fact, suggested that the spiral is the result of an instability in flows with moderate swirl; and the agreement pointed out by Ludwieg (1965) between his stability theory (1962,1965) and the measurements of Kirkpatrick (1964) and Hummel (1965) upstream of the breakdown would then be explained. With high swirl, these instabilities might not occur and the retardation of the flow would then result in the axisymmetric bubble. The second retardation which occurs in the numerical solutions for large values of V may, however, result in a region of flow behind the bubble unstable to a spiral disturbance, in which case the flow could experimentally appear as an axisymmetric bubble followed by a spiral. Such flows have, of course, been observed, and since, based on the discussion of Section 4.2, there is no physical reason why more than two retardations cannot occur, the occurrence of a number of stable retardations, appearing as axisymmetric bubbles, followed by an unstable retardation, which would appear as a spiral, is completely in accord with this theory.

The spiral and axisymmetric breakdowns may therefore only represent unstable and stable manifestations of the same physical phenomenon.

5.0 CONCLUSIONS

Numerical solutions of the full Navier-Stokes equations have been obtained for vortex breakdown. The solutions show breakdown to be a necessary occurrence in unconfined vortex flows with a large enough value of a parameter θ_1, which is a measure of the flux of axial momentum deficiency, or flow force deficiency, in the vortex core. The value of θ_1 in any flow is independent of the subcriticality or supercriticality of the assumed upstream conditions from which θ_1 is determined, and solutions exhibiting breakdown were obtained with subcritical initial conditions. The finite transition theory which requires the flow upstream of breakdown to be supercritical, therefore, cannot fully account for vortex breakdown.

The physical mechanism responsible for breakdown is the diffusion and convection of vorticity away from the vortex core, thereby requiring an increase in the pressure on the axis, and causing the retardation of axial flow. When the axial momentum of the flow near the axis is small compared to the pressure forces, which will be the case when θ_1 is large, the retardation is sufficient to produce stagnation and flow reversal and, thus, vortex breakdown. Along with pronounced axial retardation, the numerical solutions showed the breakdown bubble to be closed and contain very slowly rotating fluid. The maximum swirl velocity decreased very rapidly and the core radius increased suddenly in the breakdown region, which suggests that breakdown sould potentially be a useful means of lessening the danger aircraft wing-tip vortices present to following aircraft.

Due to the difficulty of obtaining numerical solutions at Reynolds numbers large enough for comparison, it was not possible to conclusively demonstrate that the failure of the quasi-cylindrical approximation, which occurs in the analysis of Mager (1972) for θ_1 greater than a particular value θ_1^* independent of Reynolds number, always indicates the occurrence of breakdown. However, since the values of θ_1 at which breakdown occur tend to decrease toward θ_1^* as the Reynolds number of the solutions increases, and since the relationship between the minimum axial velocity and θ_1 predicted by quasi-cylindrical analysis has been verified in these numerical solutions, there is substantial evidence that the failure of the approximation, which is the result of large axial gradients, and which occurs in vortex flows exhibiting breakdown, may also occur in those flows with substantial axial velocity retardation although slightly less than sufficient to produce stagnation.

Finally, it has been suggested that breakdowns which appear in solutions with moderate values of swirl might be unstable to spiral disturbances, in which case the physical manifestation of the breakdown might be the single asymmetric spiral observed in the experiments of Harvey (1962) and Sarpkaya (1971a). Similarly, since solutions with large values of swirl exhibit a second axial flow retardation, if the first retardation were stable and the second unstable, the physical manifestation might be the axisymmetric bubble followed by a spiral observed in the same experiments.

REFERENCES

Batchelor, G. K. (1964), "Axial flow in trailing line vortices," J. Fluid Mech. 20, 645.

Batchelor, G. K. (1970), An Introduction to Fluid Dynamics, Cambridge University Press.

Benjamin, T. B. (1962), "Theory of the vortex breakdown phenomenon," J. Fluid Mech. 28, 65.

Benjamin, T. B. (1965), "Significance of the vortex breakdown phenomenon," ASME Trans., Series D, J. of Basic Eng., p. 518.

Benjamin, T. B. (1967), "Some developments in the theory of vortex breakdown," J. Fluid Mech. 28, 65.

Bossel, H. H. (1967), "Inviscid and Viscous Models of the Vortex Breakdown Phenomenon," Ph.D. Thesis, Univ. of Calif., Berkeley.

Bossel, H. H. (1971), "Vortex computation by the method of weighted residuals using exponentials," AIAA J. 9, 2027.

Chigier, N. A. and Corsiglia, V. R. (1971), "Tip vortices--velocity distributions," Presented at the 27th Annual National Forum of the American Helocopter Society.

Chigier, N. A. and Corsiglia, V. R. (1972), "Wind-tunnel studies of wing wake turbulence," AIAA Paper No. 72-41.

Chorin, A. J. (1967), "A numerical method for solving incompressible viscous flow problems," J. Comp. Physics 2, 12.

Chorin, A. J. (1972), "Numerical study of slightly viscous flow," College of Eng., Univ. of Calif., Berkeley Rept. FM-72-4.

Dennis, S. C. R. and Chang, G.-Z. (1969), "Numerical integration of the Navier-Stokes equations for steady two-dimensional flow," Physics of Fluids, Supplement II, Proc. Int'l Symposium on High-Speed Computing in Fluid Dynamics, p. 77.

Elle, B. J. (1958), "An investigation at low speed of the flow near the apex of thin delta wings with sharp leading edges," Brit. ARC R&M 3176.

Fortin, M., Peyret, R., and Temam, R. (1971), "Résolution numérique des équations de Navier-Stokes pour un fluide incompressible," J. de Mecanique 10, 357.

Fraenkel, L. E. (1967), "On Benjamin's theory of conjugate vortex flows," J. Fluid Mech. 28, 85.

Gartshore, I. S. (1962), "Recent work in swirling incompressible flow," NRC (Canada) Aero.Report LR-343.

Gartshore, I. S. (1963), "Some numerical solutions for the viscous core of an irrotational vortex," NRC (Canada) Aero. Report LR-378.

Gore, R. W. and Ranz, W. E. (1964), "Backflows in rotating fluids," AICHE J. 10, 83.

Hall, M. G. (1966), "On the occurrence and identification of vortex breakdown," RAE TR 66283.

Hall, M. G. (1967), "A new approach to vortex breakdown," Proc. 1967 Heat Transfer and Fluid Mechanics Institute, Stanford Univ. Press, pp. 319-340.

Hall, M. G. (1972), "Vortex breakdown," Annual Review of Fluid Mechanics (M. Van Dyke and W. G. Vincente, eds), Vol 4, p. 195.

Harvey, J. K. (1962), "Some observations of the vortex breakdown phenomenon," J. Fluid Mech. 14, 585.

Hummel, D. (1965), "Untersuchungen über das Aufplatzen der Wirbel an Schanken Deltafugeln, " Z. Flugwiss. 13, 158.

Kirkpatrick, C. L. I. (1965), "Experimental Investigation of the Breakdown of a Vortex in a Tube," Brit. ARC CP No. 821.

Lambourne, N. C., and Bryer, D. W. (1961), "The bursting of leading edge vortices," Brit. ARC R&M 3282.

Ludwieg, H. (1962), "Zur Erklärung der Instabilität der über angestellten Deltaflügeln auftretenden freien Wirbelkerne," Z. Flugwiss. 10, 242.

Ludwieg, H. (1965), "Erklärung des Wirbelaufplatzens mit Hilfe der Stabilitatstheorie für Strömunger mit schraubenförmigen Stromlinier," Z. Flugwiss. 13, 437.

Mager, A. (1972), "Dissipation and breakdown of a wing-tip vortex," J. Fluid Mech. 55, 609.

McCormick, B. W., Tangler, J. L., and Sherrieb, H. E. (1968), "Structure of Trailing Vortices," J. of Aircraft 5, 260.

Morton, B. R. (1966), "Geophysical vortices," *Progress in Aeronautical Sciences* (D. Küchemann, Ed.), Pergamon Press, Oxford, Vol. 7.

Morton, B. R. (1969), "The strength of vortex and swirling core flows," J. Fluid Mech. 38, 315.

Orzag, S. A. (1971), "Numerical simulation of incompressible flows within simple boundaries: accuracy," J. Fluid Mech. 49, 75.

Orzag, S. A. (1974), "Numerical simulation of viscous incompressible flows," Flow Research, Inc. Report No. 17.

Pao, Y.-H. and Daugherty, R. J. (1969), "Time-Dependent Viscous Incompressible Flow Past a Finite Flat Plate," Boeing Scientific Research Lab., D1-82-0822.

Peaceman, D. W. and Rachford, H. H., Jr. (1955), "The Numerical Solution of Parabolic and Elliptic Differential Equations," J. Soc. Indust. Appl. Math. 3, 28.

Peckham, D. H. and Atkinson, S. A. (1957), "Preliminary results of low speed wind tunnel tests on a Gothic wing of aspect ratio 1.0," Brit. ARC CP 508.

Plows, W. H. (1968), "Some numerical results for two-dimensional steady laminar Benard convection," Physics of Fluids 11, 1593.

Richtmyer, R. D. and Morton, K. W. (1967), Difference Methods for Initial-Value Problem, Second Ed., Interscience.

Rimon, Y. and Cheng, S. I. (1969), "Numerical Solution of a Uniform Flow over a Sphere at Intermediate Reynolds numbers," Physics of Fluids 12, 949.

Roache, P. J. (1972), Computational Fluid Dynamics, Hermosa Publishers.

Sarpkaya, T. (1971a), "On stationary and travelling vortex breakdowns," J. Fluid Mech. 45, 545.

Sarpkaya, T. (1971b), "Vortex Breakdown in Swirling Conical Flows," AIAA J. 9, 1792.

Skoglund, V. J. and Gay, B. D. (1968), "Numerical Analysis of Gas Dynamics," Bureau of Engineering Research Progress Report PR-85(68)S-082, The University of New Mexico, Albuquerque, N.M.

So, K. L. (1967), "Vortex phenomena in a conical diffuser," AIAA J. 5, 1072.

Squire, H. B. (1960), "Analysis of the 'vortex breakdown' phenomenon, Part I," Imperial College, Aero. Dept. Rept. 102.

Taylor, T. D. and Ndefo, E. (1970), "Computation of viscous flow in a channel by the method of splitting," Proceedings of the Second International Conference on Numerical Methods in Fluid Dynamics (M. Holt, Ed.), Lecture Notes in Physics, Vol. 8, Springer-Verlag, New York.

Werle, H. (1960), "Sur l'ećlatement des tourbillons d'apex d'une aile delta aux faibles vitesses," Recherche Aéronautique 74, 23.

TABLE 1. REYNOLDS NUMBERS OF FINITE DOMAIN SOLUTIONS FOR α - V COMBINATIONS

		α		
V	0.30	0.60	1.0	1.4
0.55	200	100		
0.63	200	100	100	200
		200	200	
			500	
			1000	
0.70	200	100		
		200		
0.775	200	200		
0.80		100	200	
0.82	200			
0.85			200	
0.8944	200	100	100	200
		200	200	
			500	
			1000	
0.95				200
1.0	200		200	200
1.095		100	100	200
		200	200	
			500	
			1000	
1.342			100	

TABLE 2. ϕ_{max} AND θ_1 FOR SOLUTIONS WITH $Re = 200$, $\alpha = 1$

V	ϕ_{max} (degrees)	θ_1
0.63	34.38	-0.231
0.80	40.99	-0.112
0.85	42.71	-0.081
0.8944	44.17	-0.056
1.0	47.36	0.
1.095	49.95	0.046

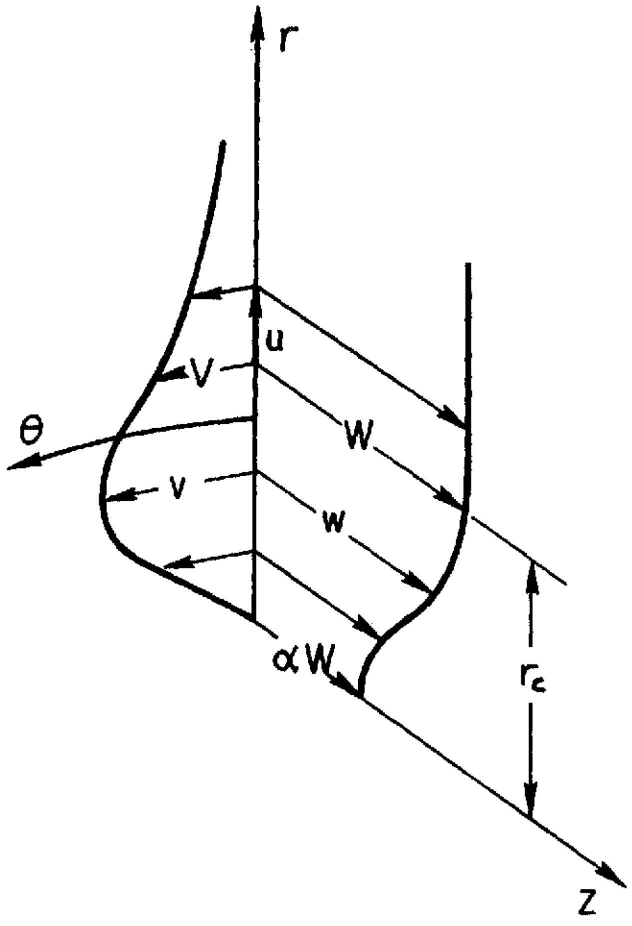

Fig. 1. COORDINATE SYSTEM AND VELOCITIES

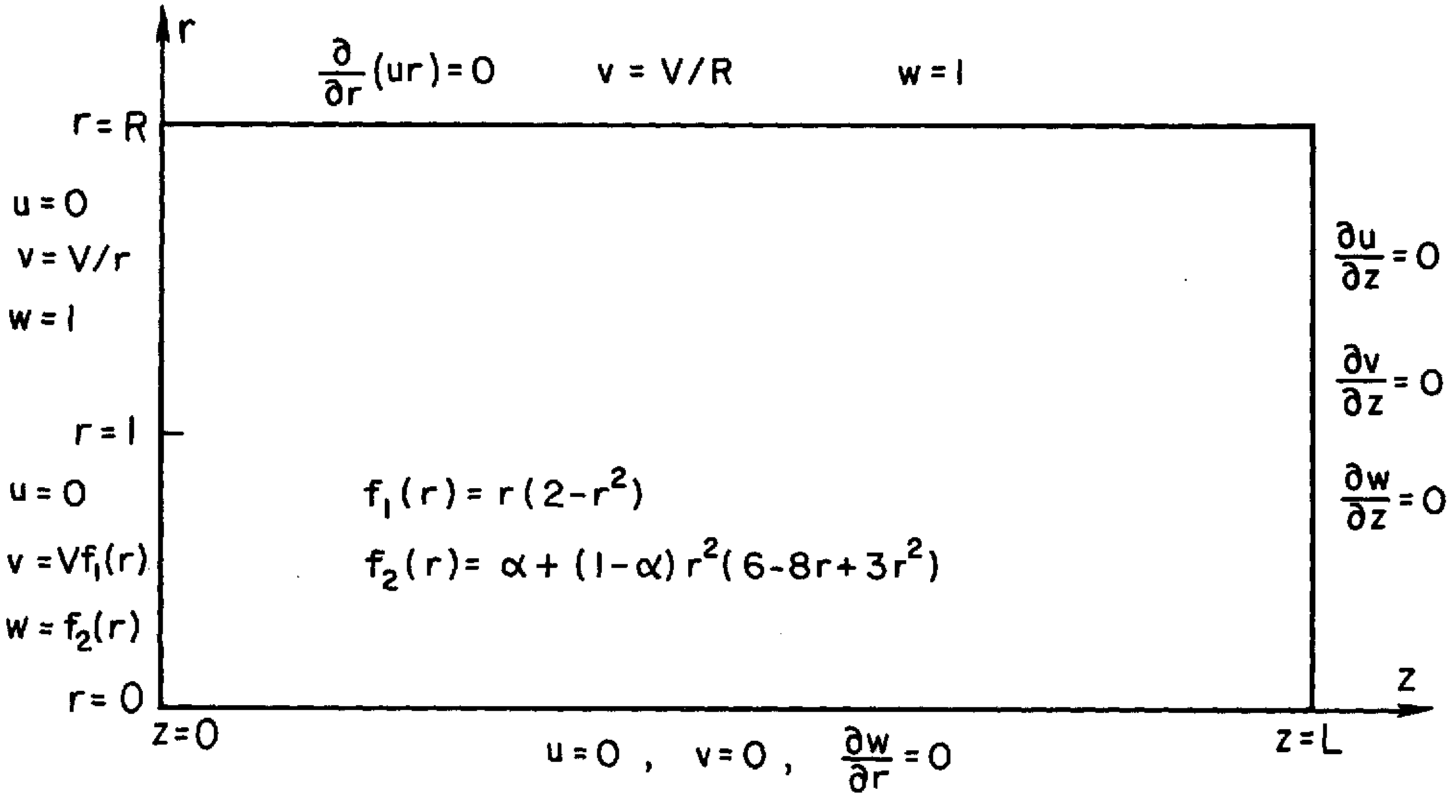

Fig. 2. BOUNDARY CONDITIONS

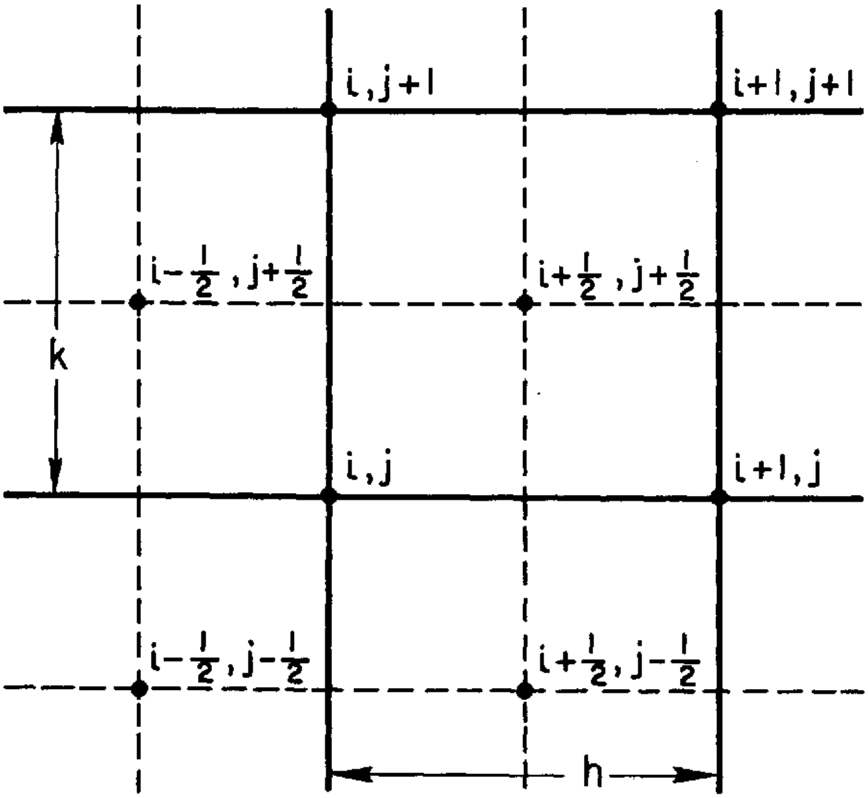

Fig. 3. STAGGERED GRID SYSTEM

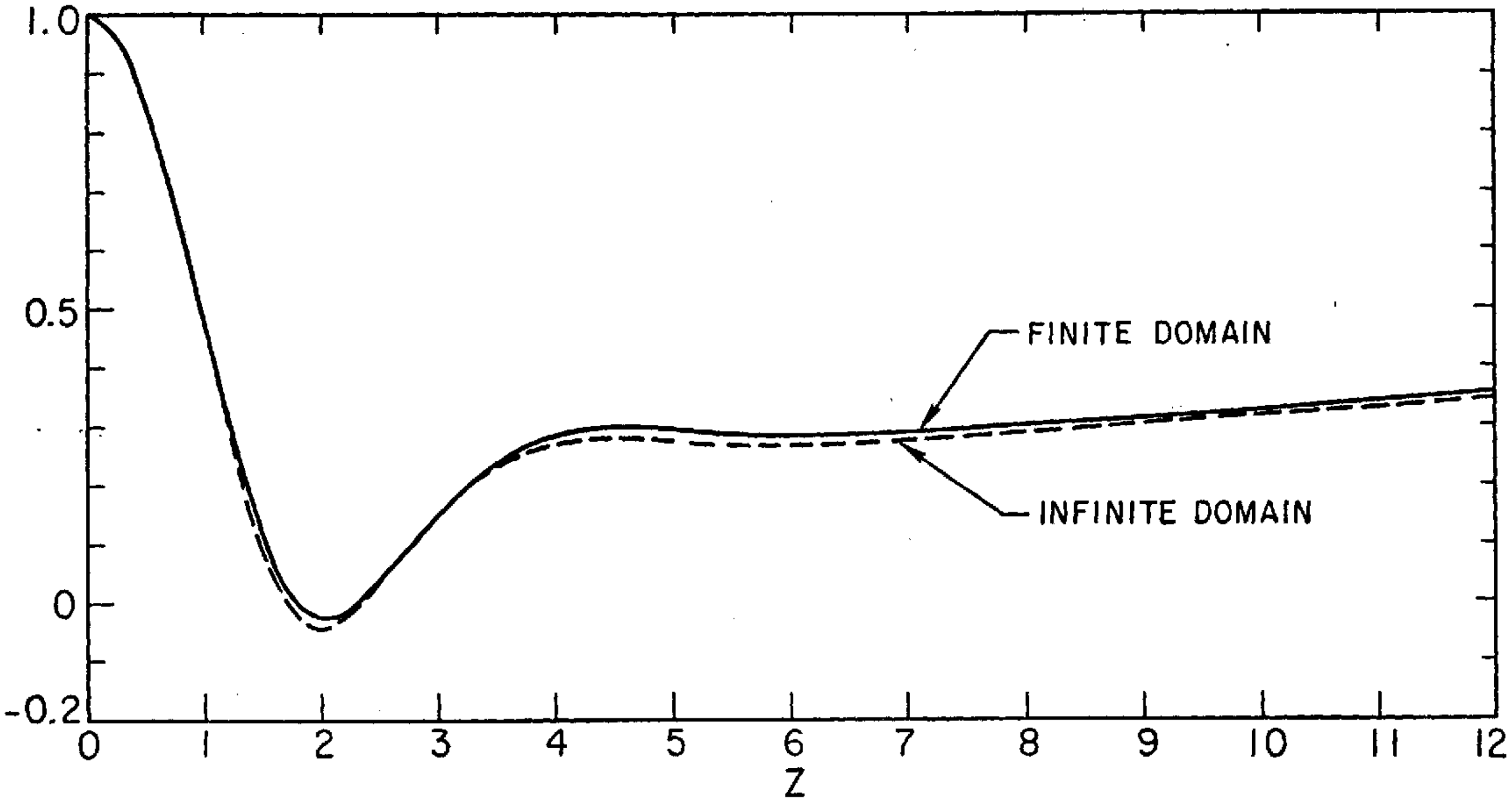

AXIAL VELOCITY ON AXIS VS. Z
Re = 100, $\alpha = 1$, V = 1

Fig. 4. COMPARISON OF SOLUTIONS OBTAINED FROM FINITE AND INFINITE DOMAINS

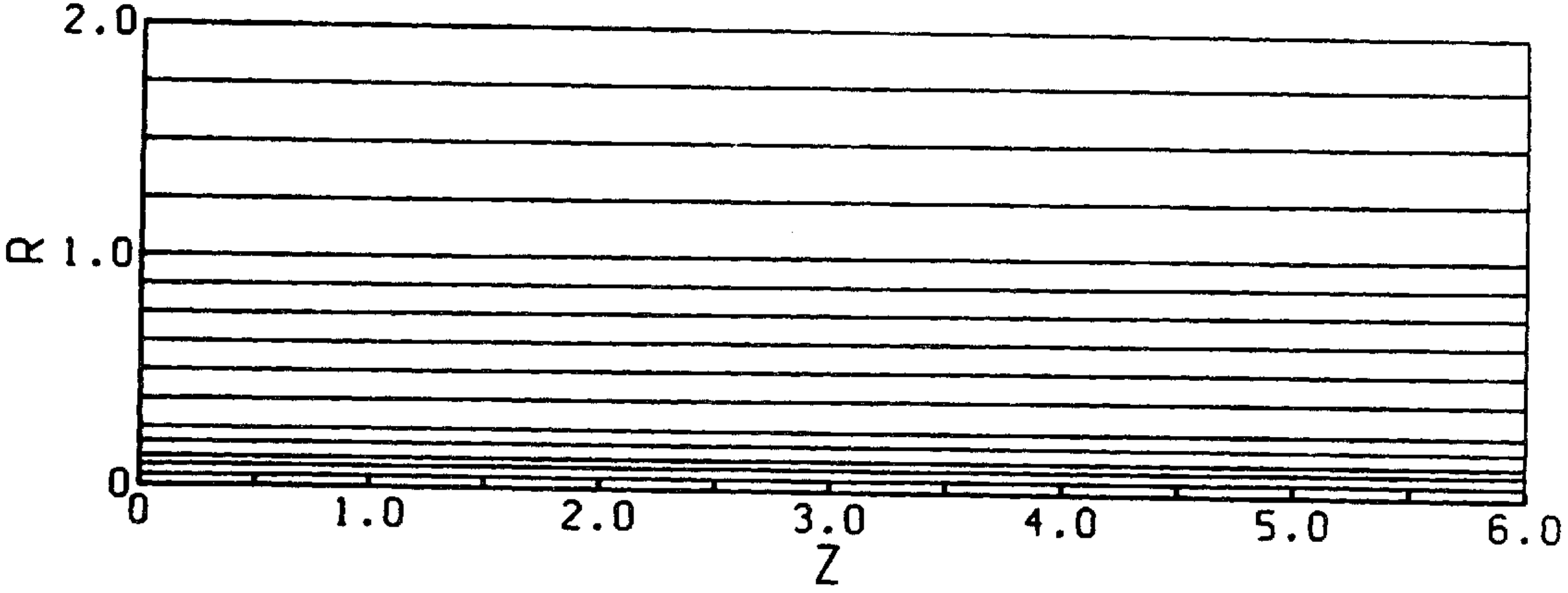

Fig. 5a. STREAM FUNCTION CONTOURS - Re = 200, α = 1.0, V = 0.63

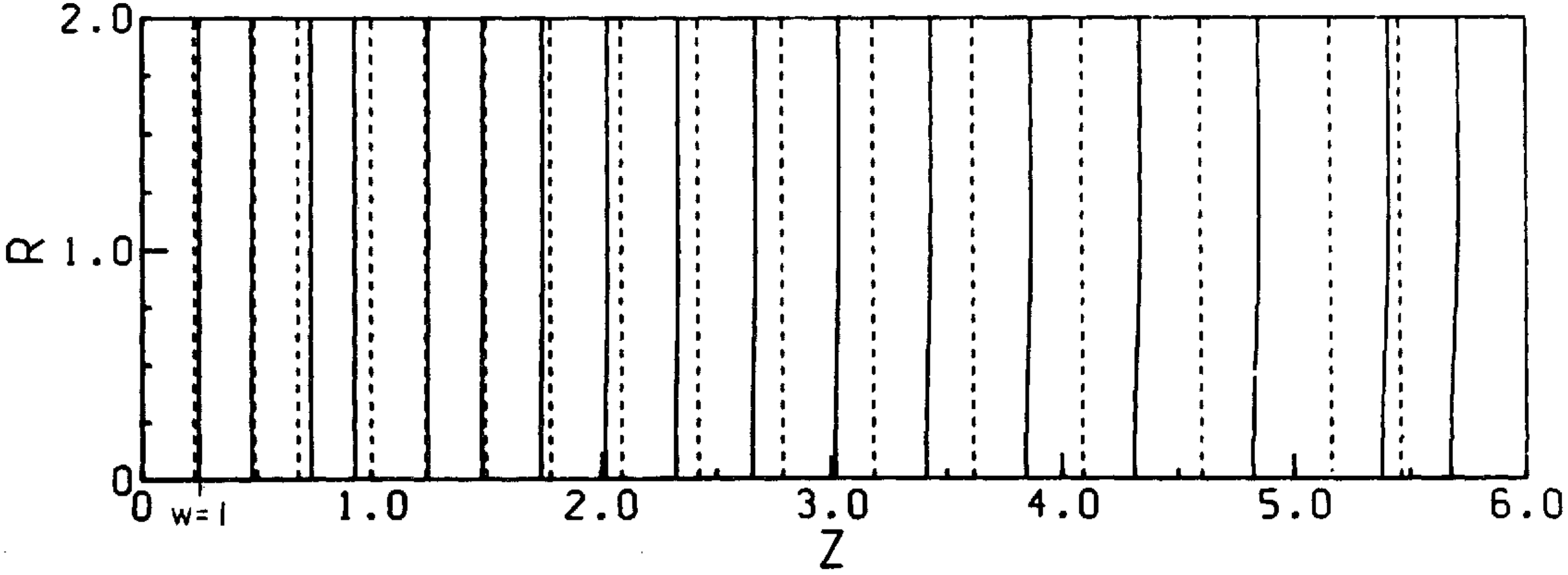

Fig. 5b. AXIAL VELOCITY PROFILES - Re = 200, α = 1.0, V = 0.63

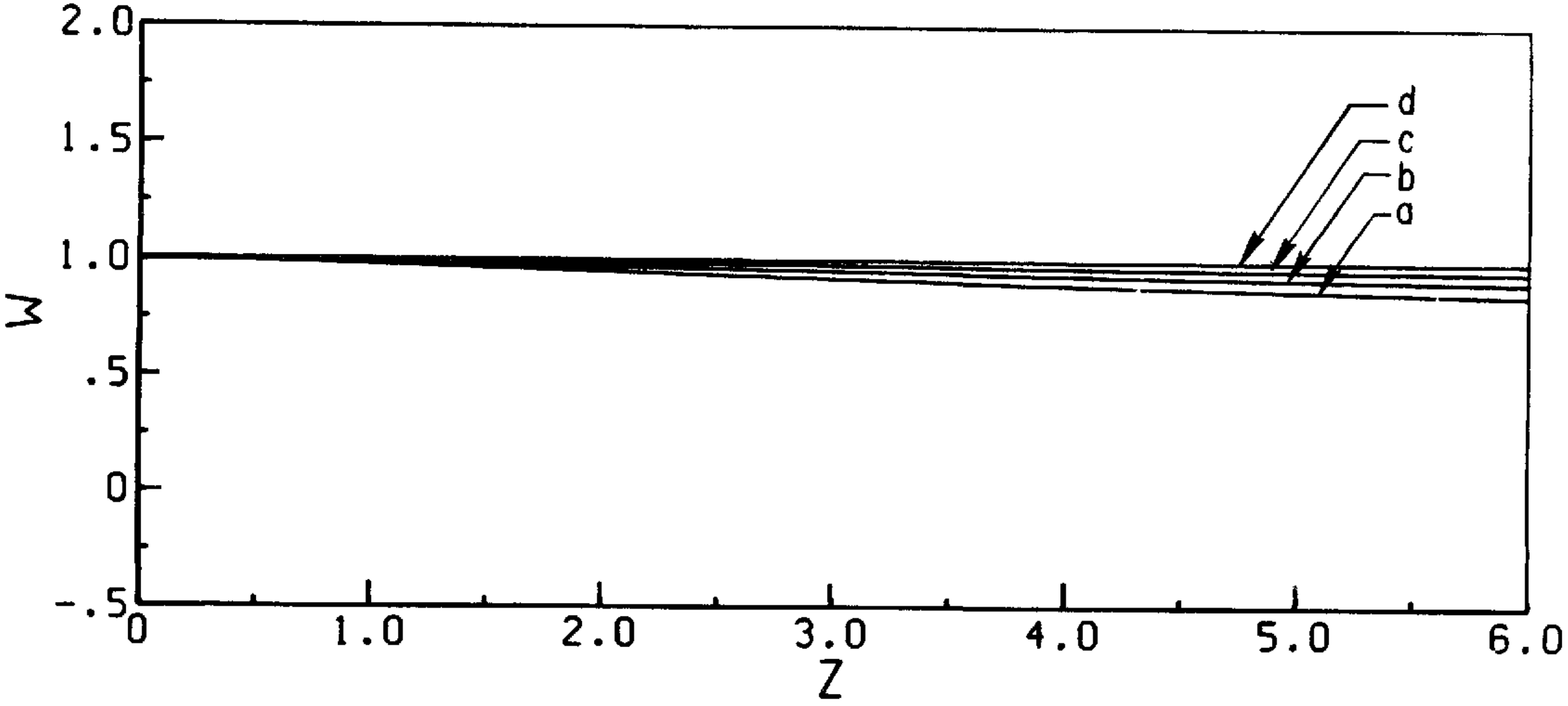

Fig. 5c. AXIAL VELOCITY VARIATION WITH z AT FIXED RADIAL POSITIONS -- Re = 200, $\alpha = 1.0$, V = 0.63
(a) r = 0 ; (b) r = 0.486 ; (c) r = 0.714 ; (d) r = 1.0

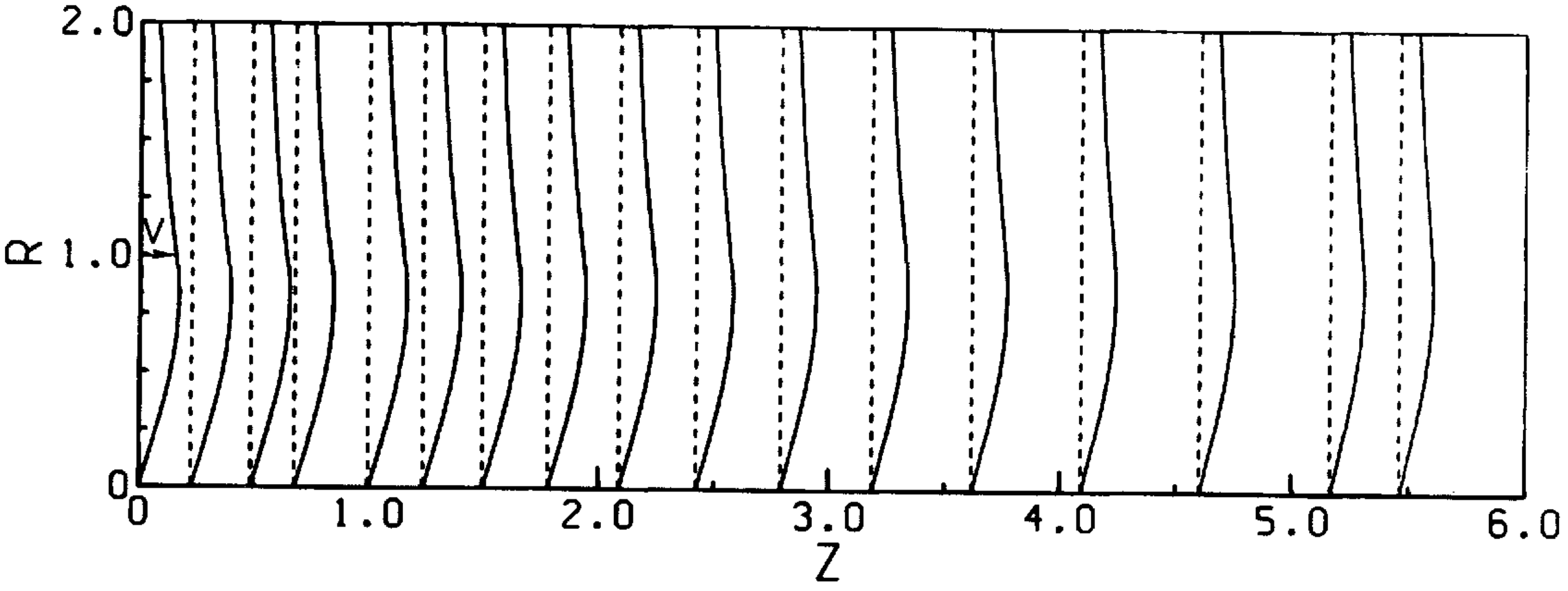

Fig. 5d. SWIRL VELOCITY PROFILES -- Re = 200, α = 1.0, V = 0.63

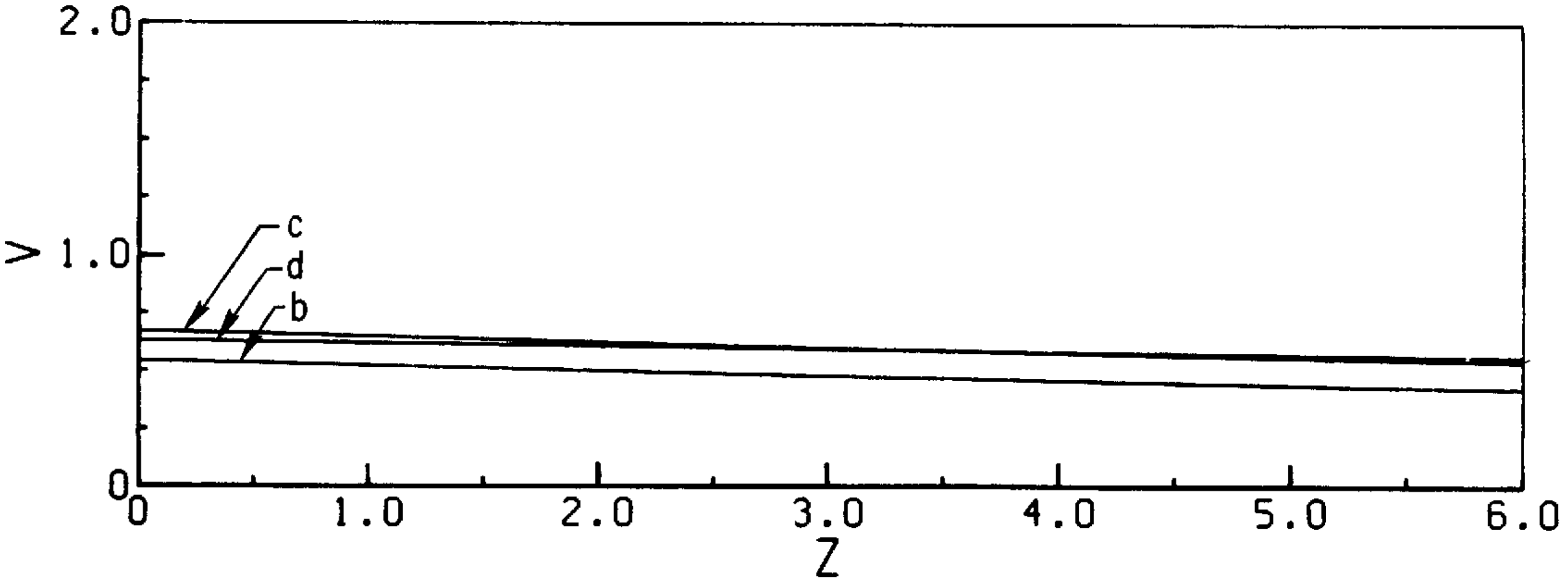

Fig. 5e. SWIRL VELOCITY VARIATION WITH z AT FIXED RADIAL POSITIONS -- Re = 200, α = 1.0, V = 0.63
(b) r = 0.486 ; (c) r = 0.714 ; (d) r = 1.0

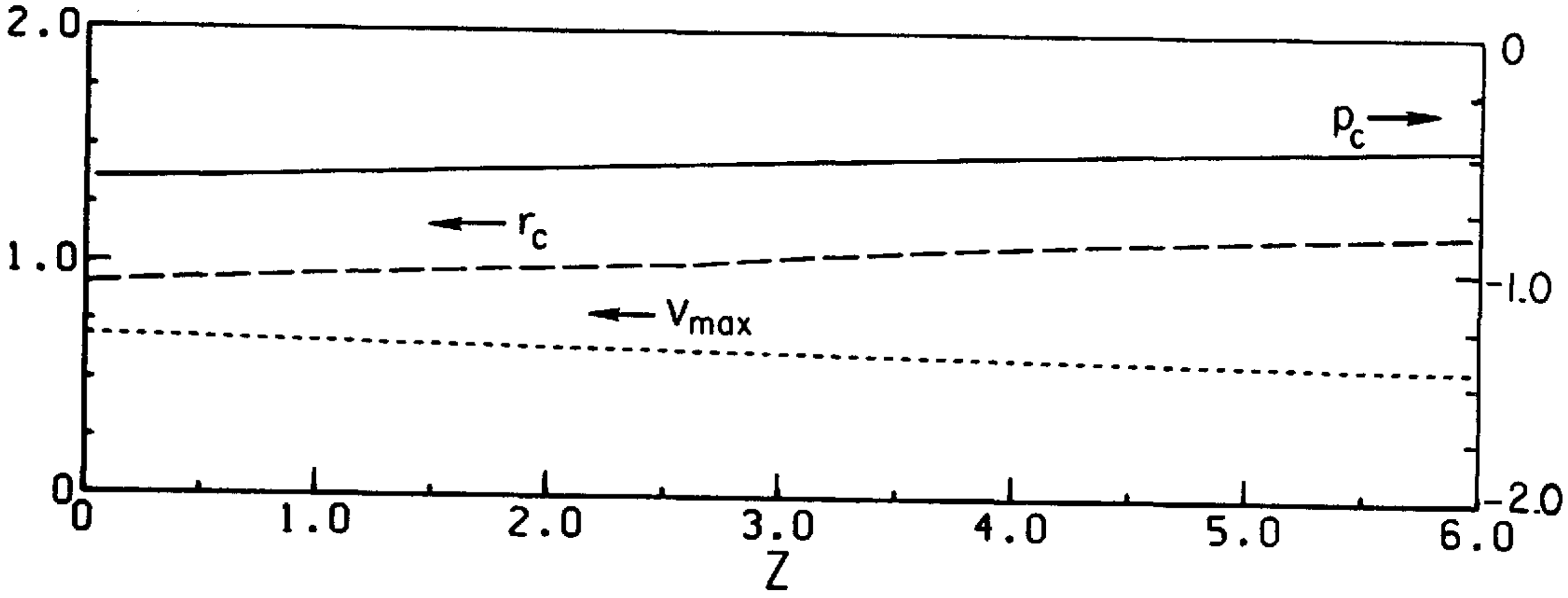

Fig. 5f. CORE PRESSURE NEAR AXIS, CORE RADIUS, AND MAXIMUM SWIRL VELOCITY vs. z
Re = 200, α = 1.0, V = 0.63

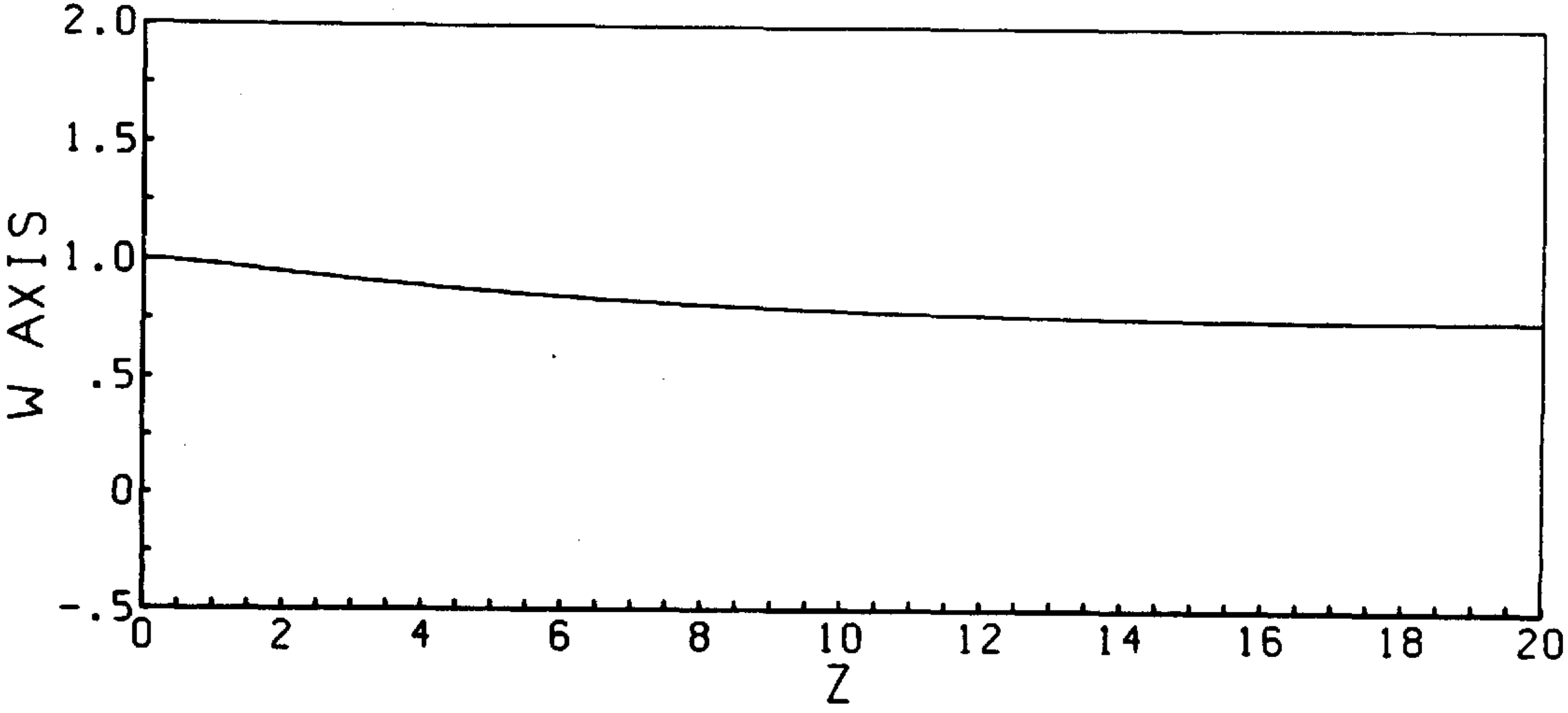

Fig. 5g. AXIAL VELOCITY ON AXIS vs. z -- Re = 200, α = 1.0, V = 0.63

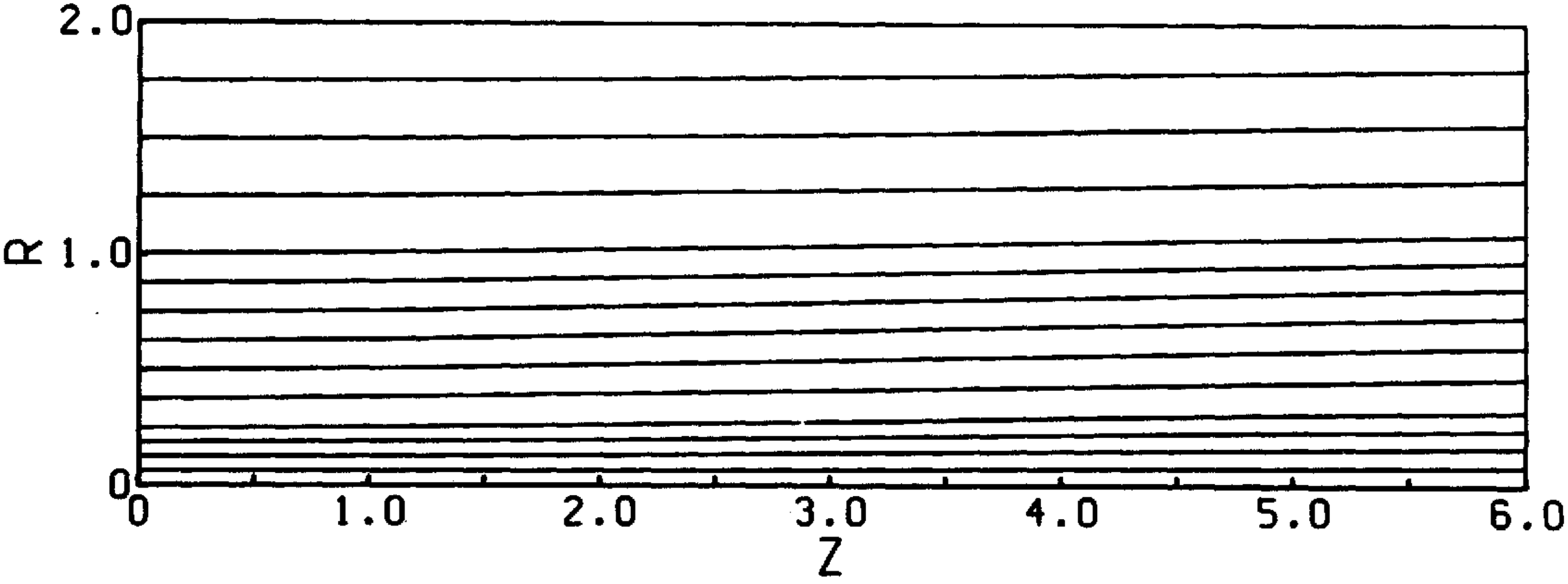

Fig. 6a. STREAM FUNCTION CONTOURS -- Re = 200, α = 1.0, V = 0.80

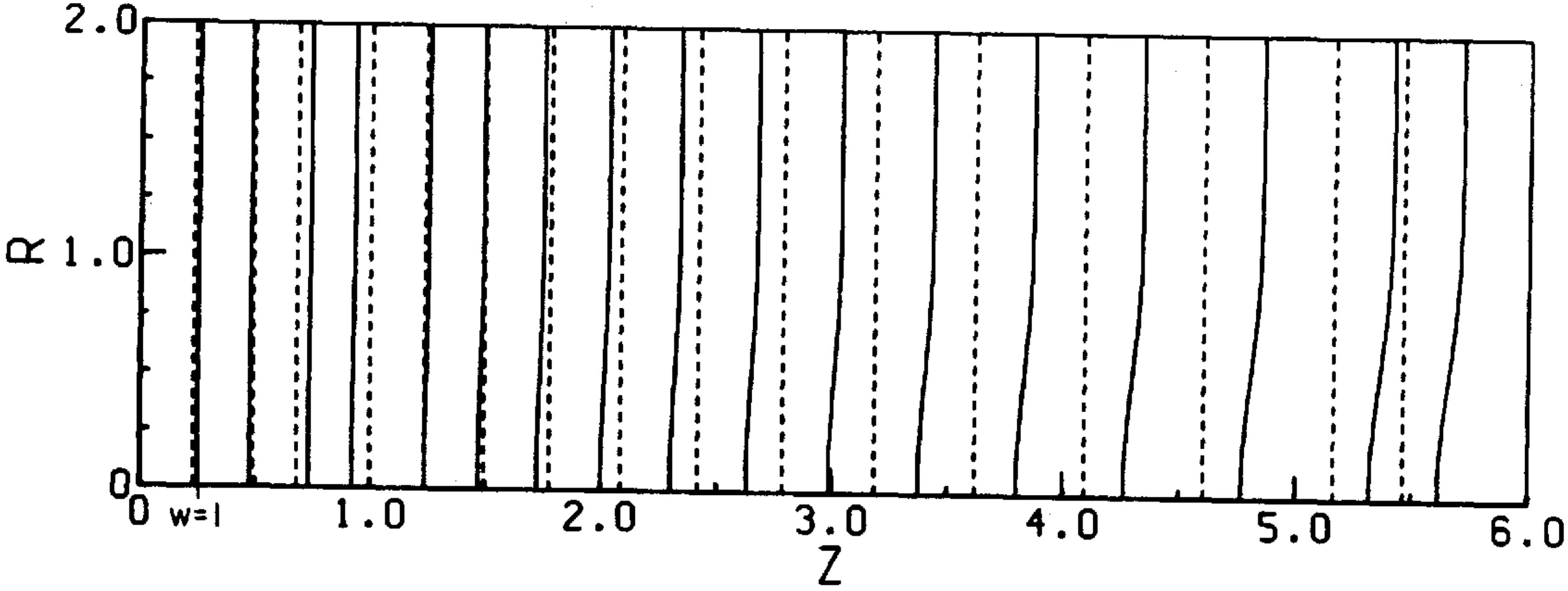

Fig. 6b. AXIAL VELOCITY PROFILES -- Re = 200, α = 1.0, V = 0.80

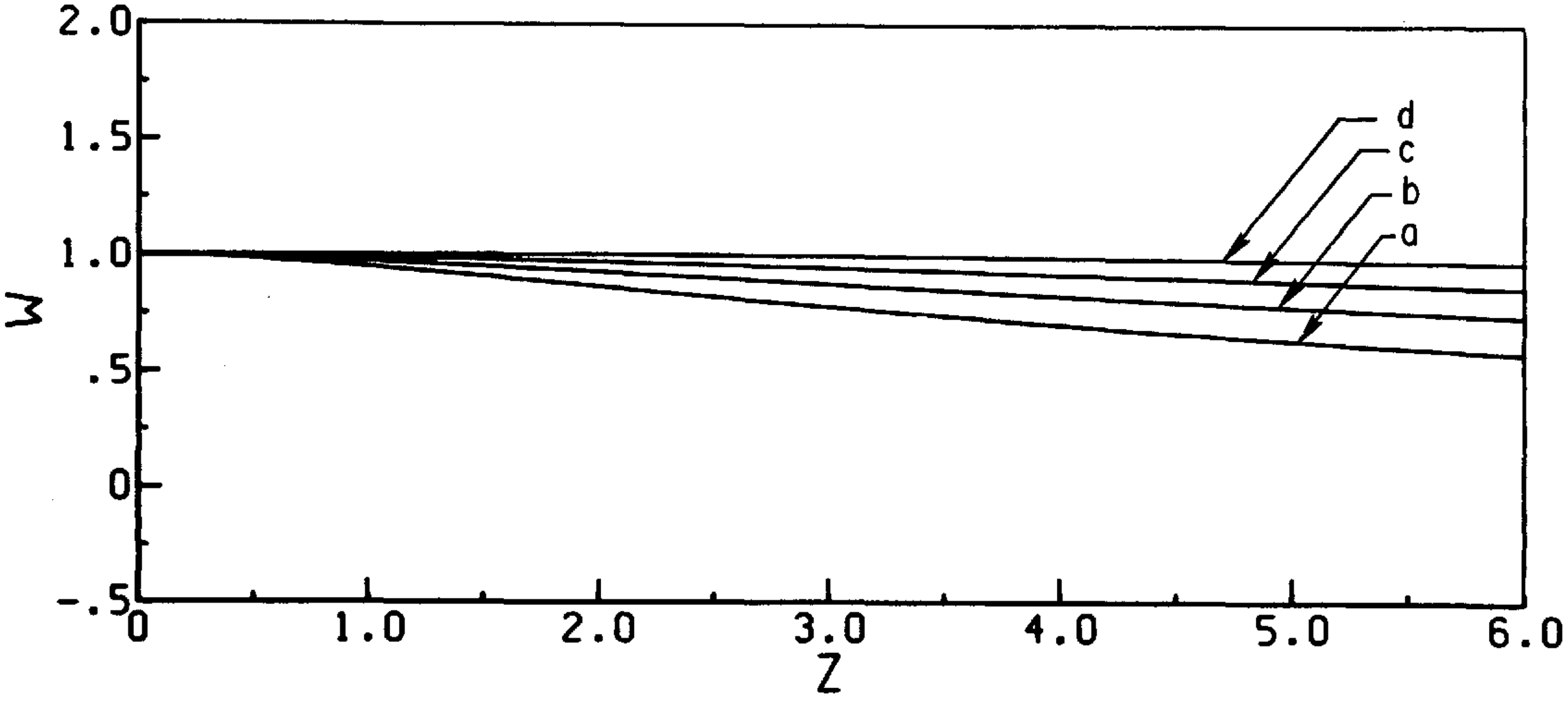

Fig. 6c. AXIAL VELOCITY VARIATION WITH z AT FIXED RADIAL POSITIONS -- Re = 200, α = 1.0, V = 0.80
(a) r = 0 ; (b) r = 0.486 ; (c) r = 0.714 ; (d) r = 1.0

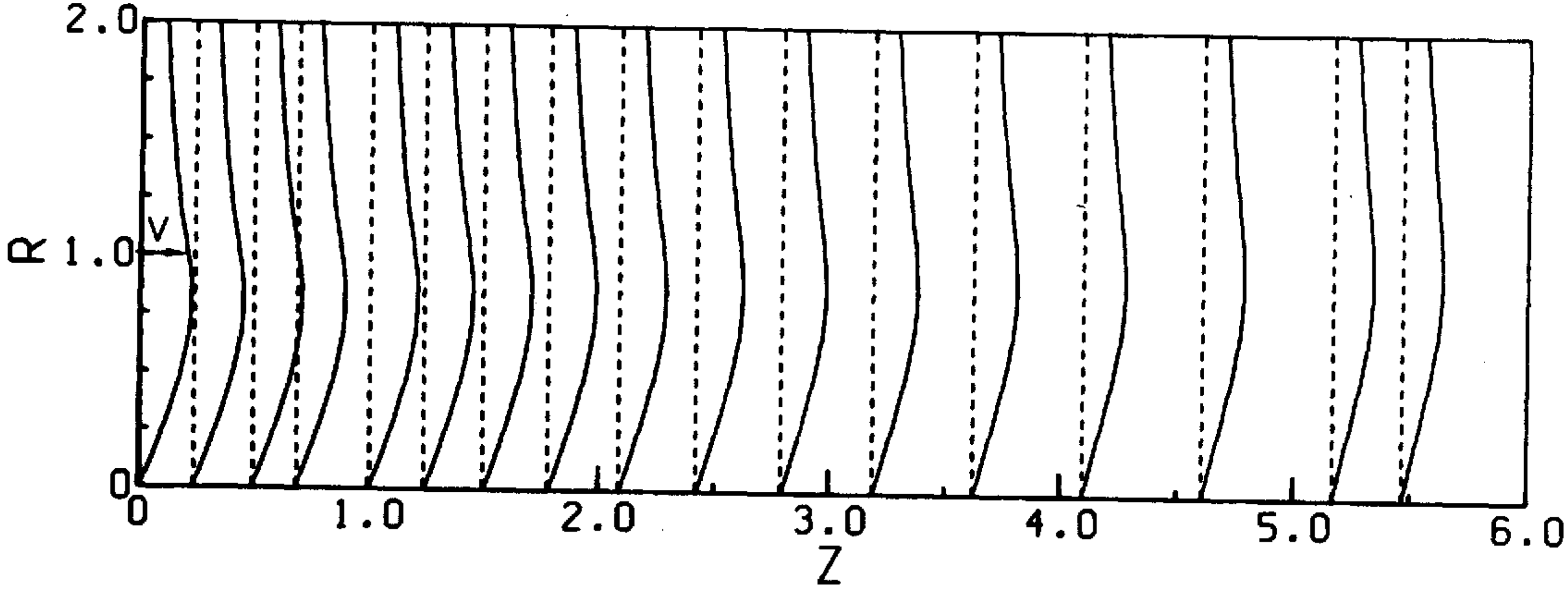

Fig. 6d. SWIRL VELOCITY PROFILES -- Re = 200, α = 1.0, V = 0.80

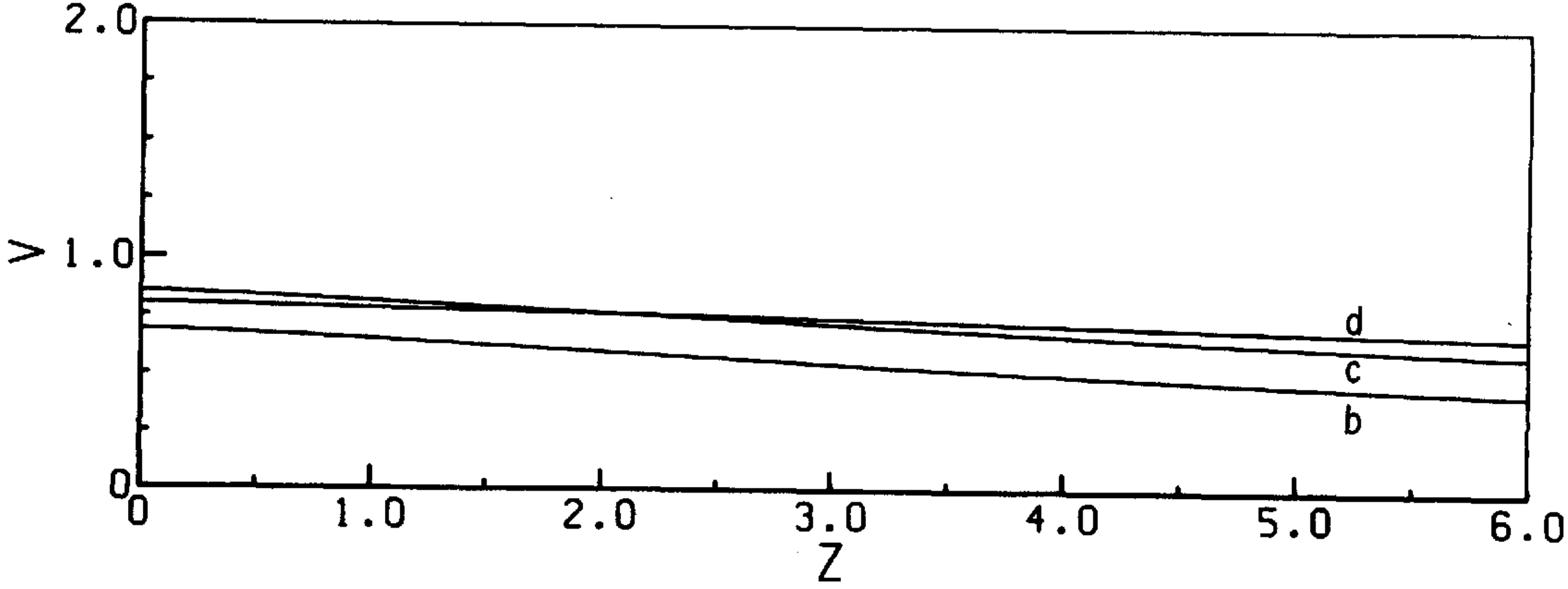

Fig. 6e. SWIRL VELOCITY VARIATION WITH z AT FIXED RADIAL POSITIONS -- Re = 200, α = 1.0, V = 0.80
(b) r = 0.486 ; (c) r = 0.714 ; (d) r = 1.0

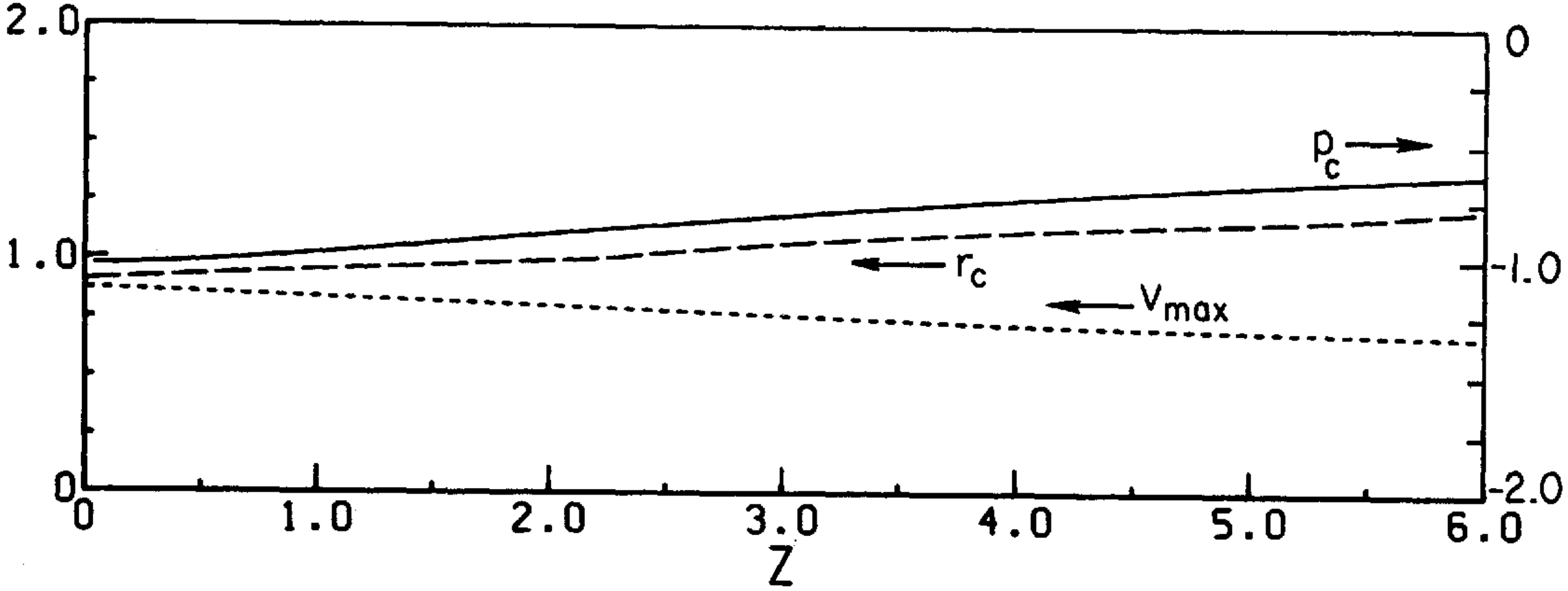

Fig. 6f. CORE PRESSURE NEAR AXIS, CORE RADIUS, AND MAXIMUM SWIRL VELOCITY vs. z

Re = 200, α = 1.0, V = 0.80

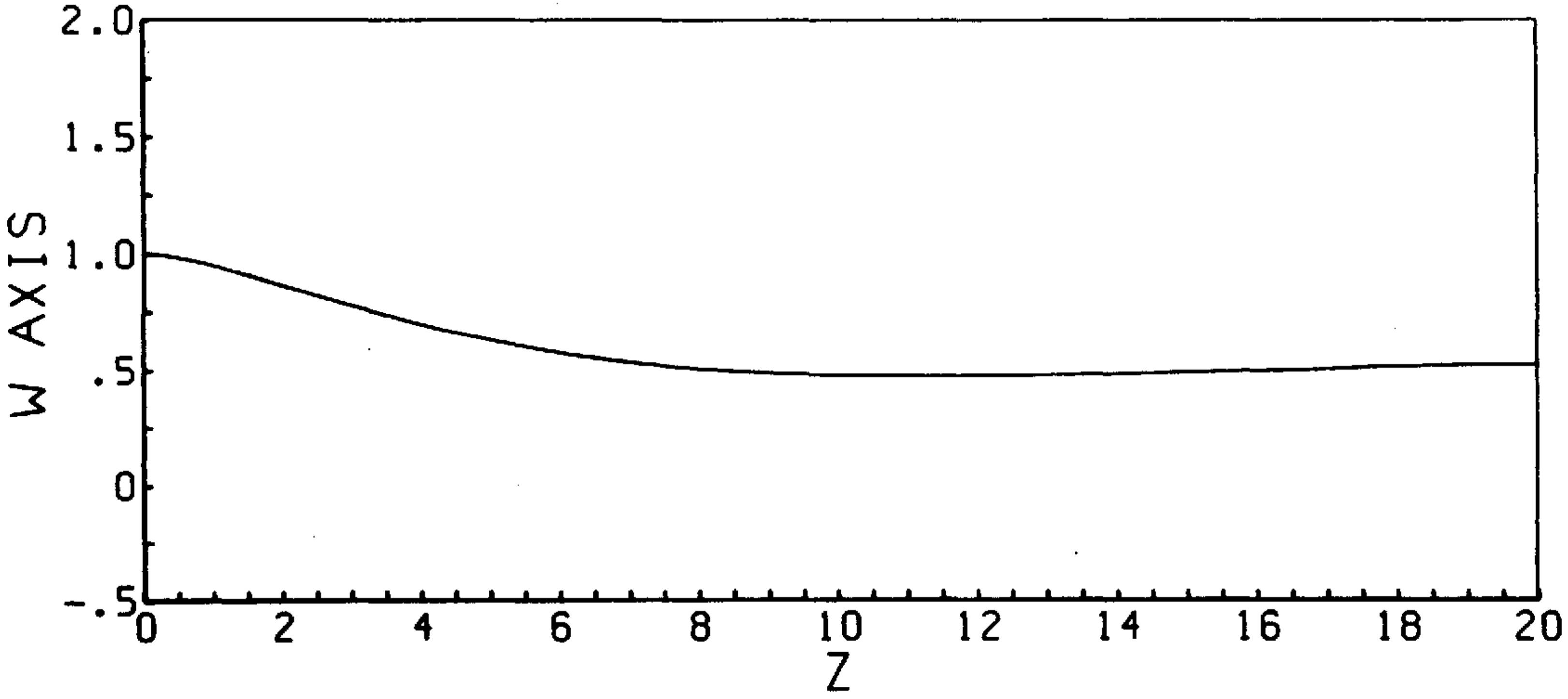

Fig. 6g. AXIAL VELOCITY ON AXIS vs. z -- Re = 200, α = 1.0, V = 0.80

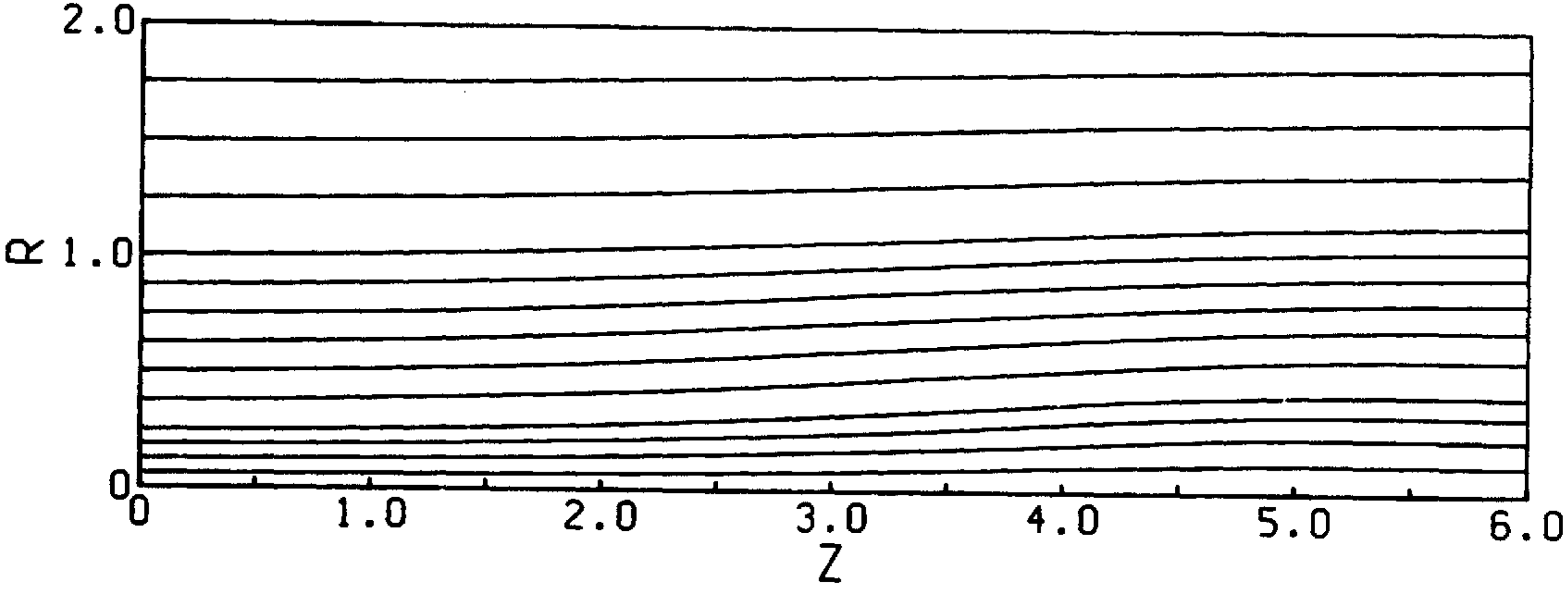

Fig. 7a. STREAM FUNCTION CONTOURS -- Re = 200, $\alpha = 1.0$, V = 0.85

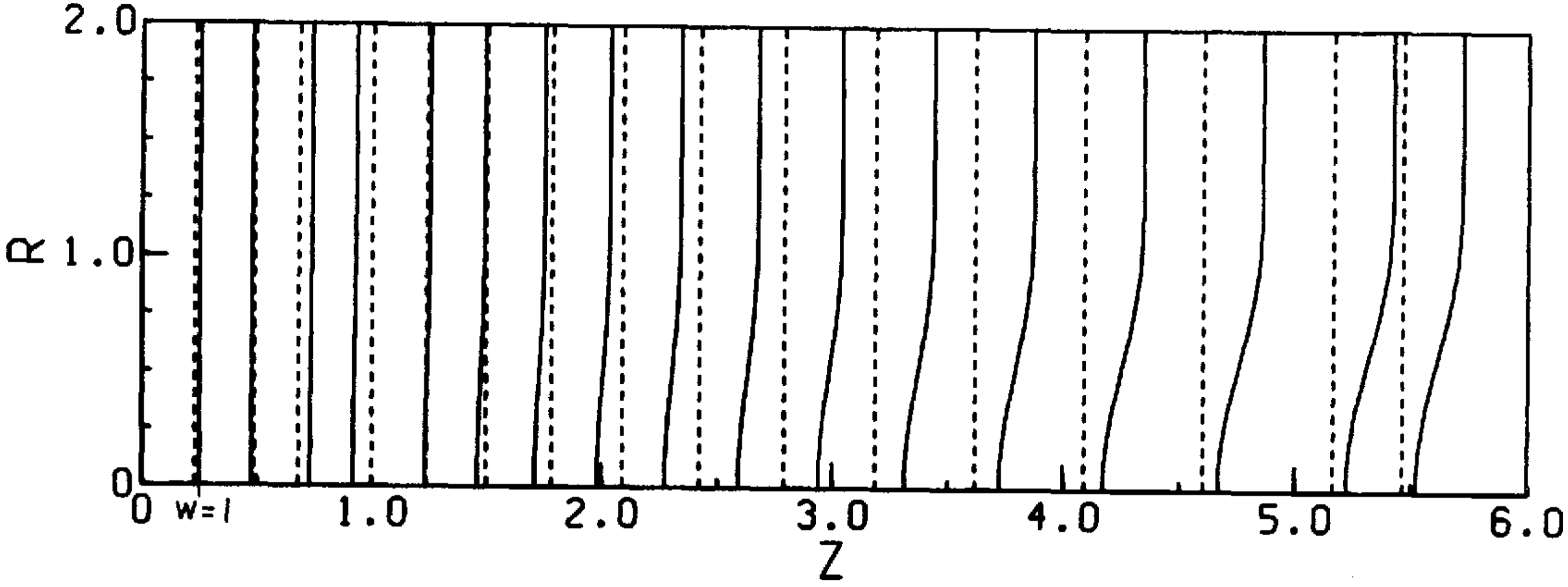

Fig. 7b. AXIAL VELOCITY PROFILES -- Re = 200, α = 1.0, V = 0.85

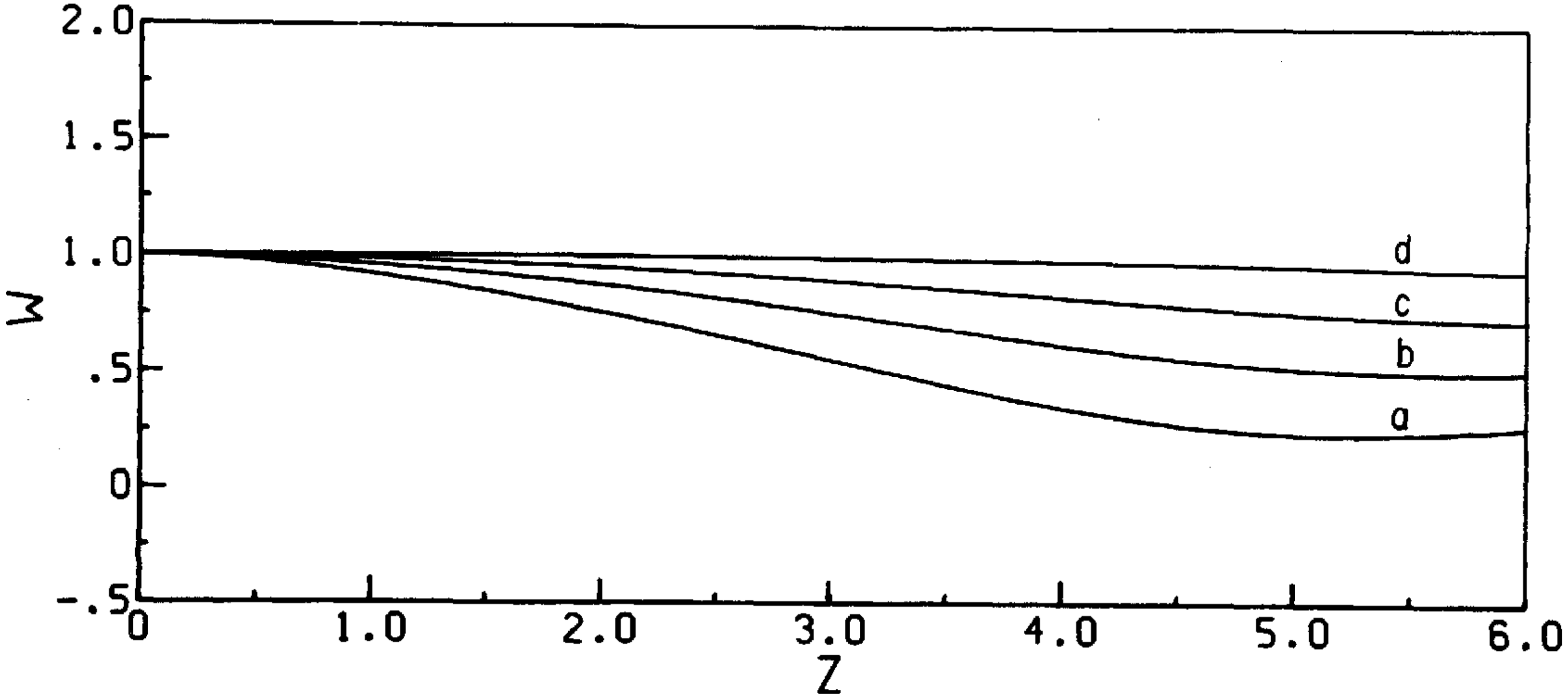

Fig. 7c. AXIAL VELOCITY VARIATION WITH z AT FIXED RADIAL POSITIONS -- Re = 200, α = 1.0, V = 0.85
(a) r = 0 ; (b) r = 0.486 ; (c) r = 0.714 ; (d) r = 1.0

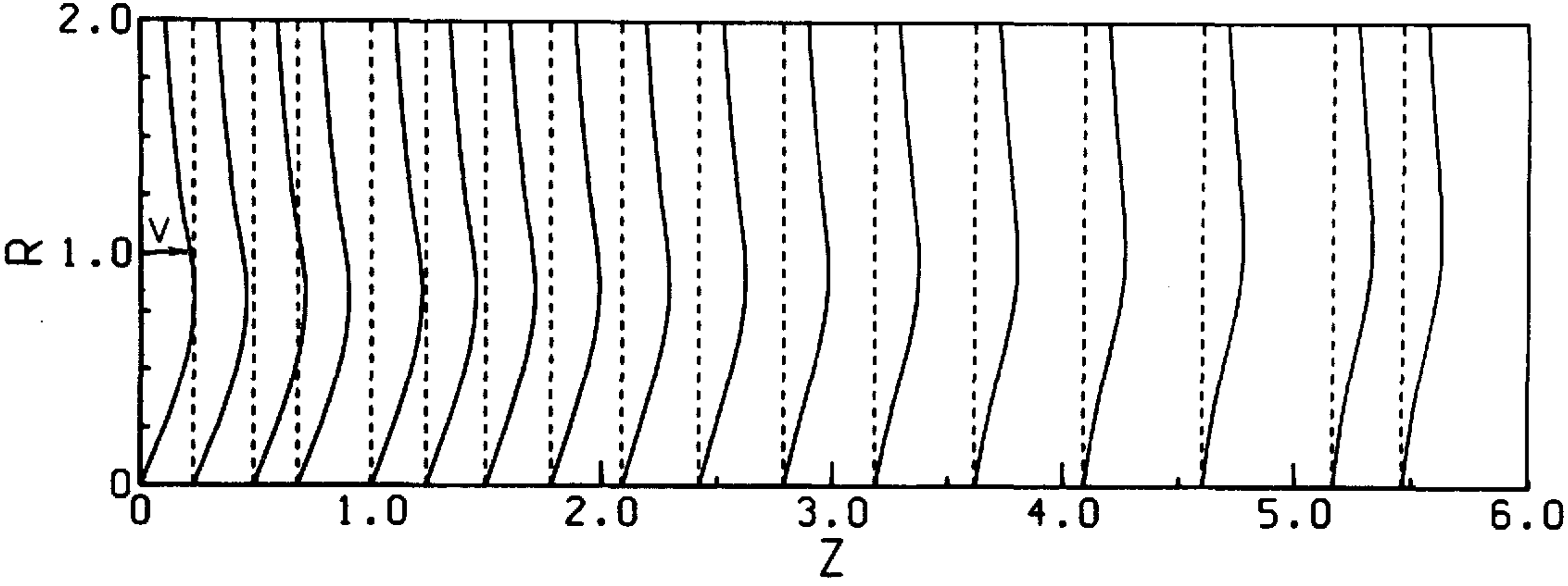

Fig. 7d. SWIRL VELOCITY PROFILES -- Re = 200, α = 1.0, V = 0.85

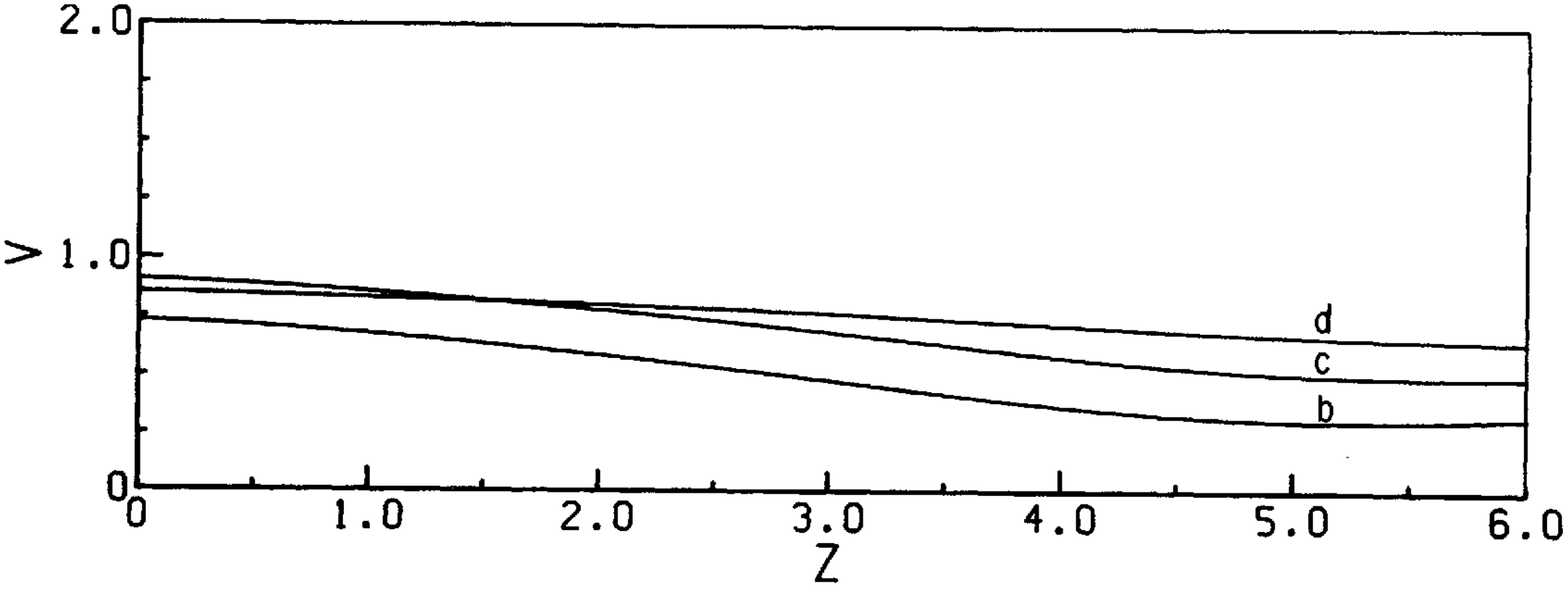

Fig. 7e. SWIRL VELOCITY VARIATION WITH z AT FIXED RADIAL POSITIONS -- Re = 200, α = 1.0, V = 0.85
(b) r = 0.486 ; (c) r = 0.714 ; (d) r = 1.0

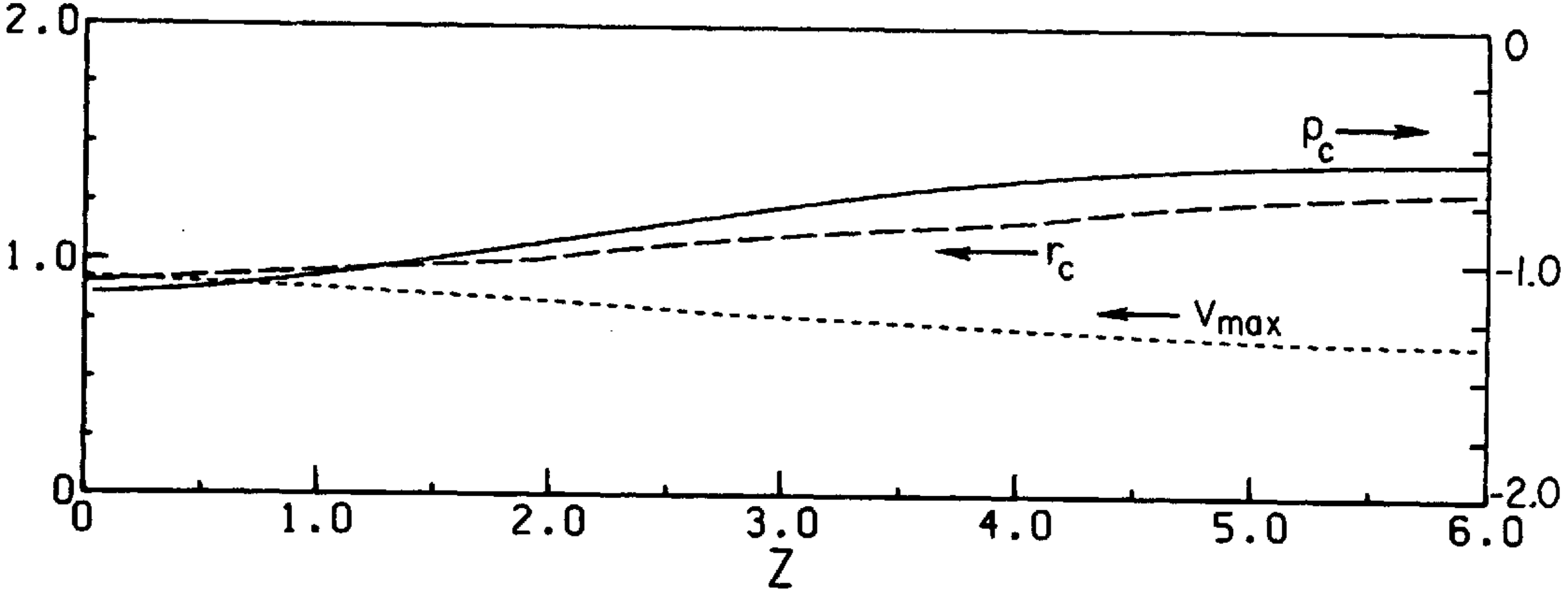

Fig. 7f. CORE PRESSURE NEAR AXIS, CORE RADIUS, AND MAXIMUM SWIRL VELOCITY vs. z
Re = 200, α = 1.0, V = 0.85

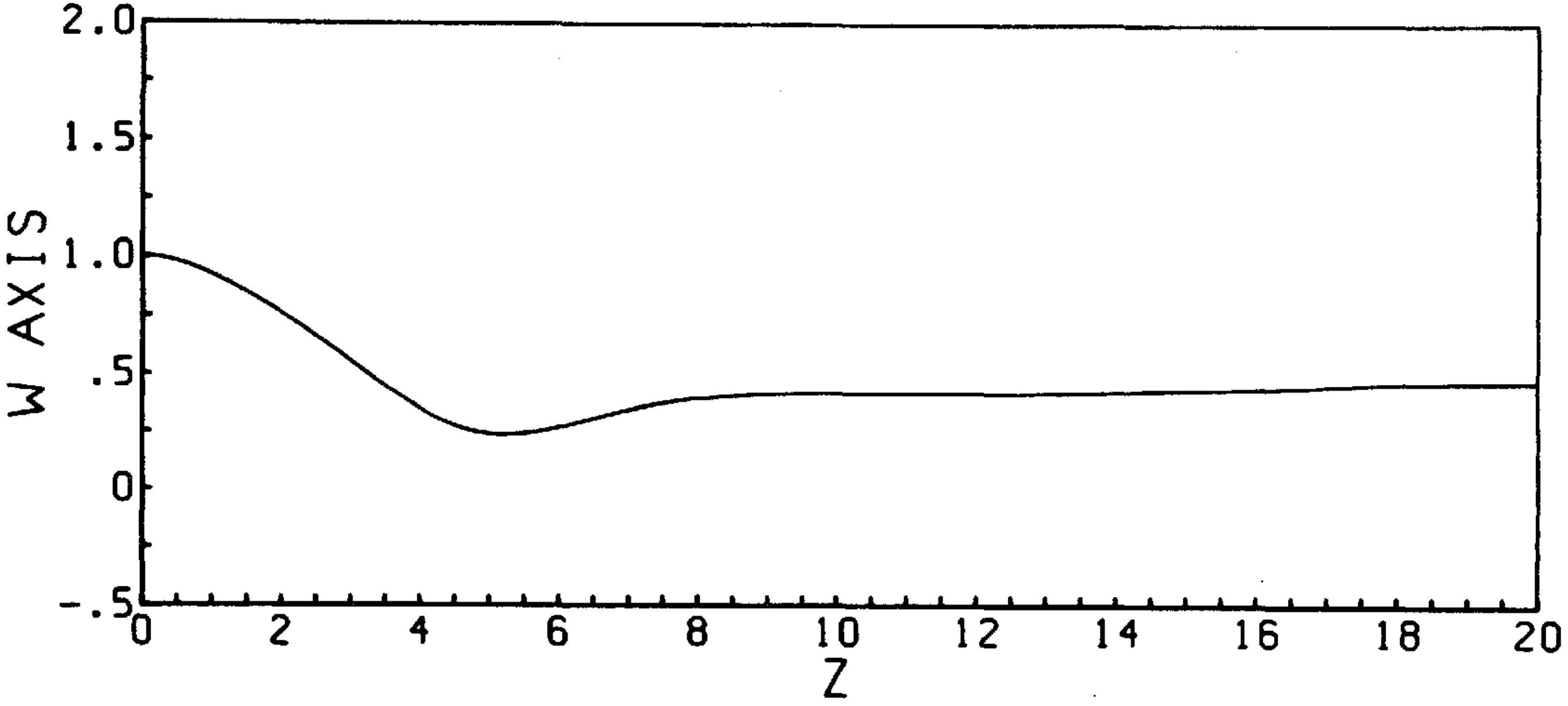

Fig. 7g. AXIAL VELOCITY ON AXIS vs. z -- Re = 200, α = 1.0, V = 0.85

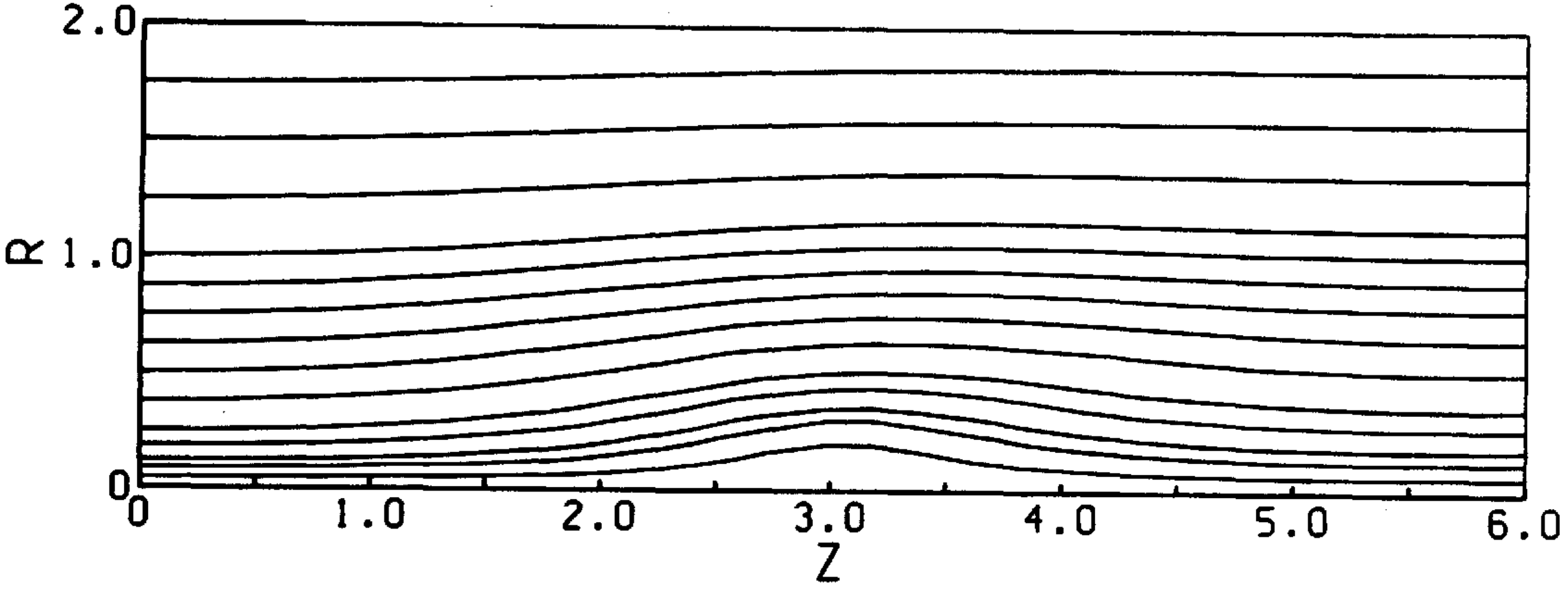

Fig. 8a. STREAM FUNCTION CONTOURS -- Re = 200, α = 1.0, V = 0.8944

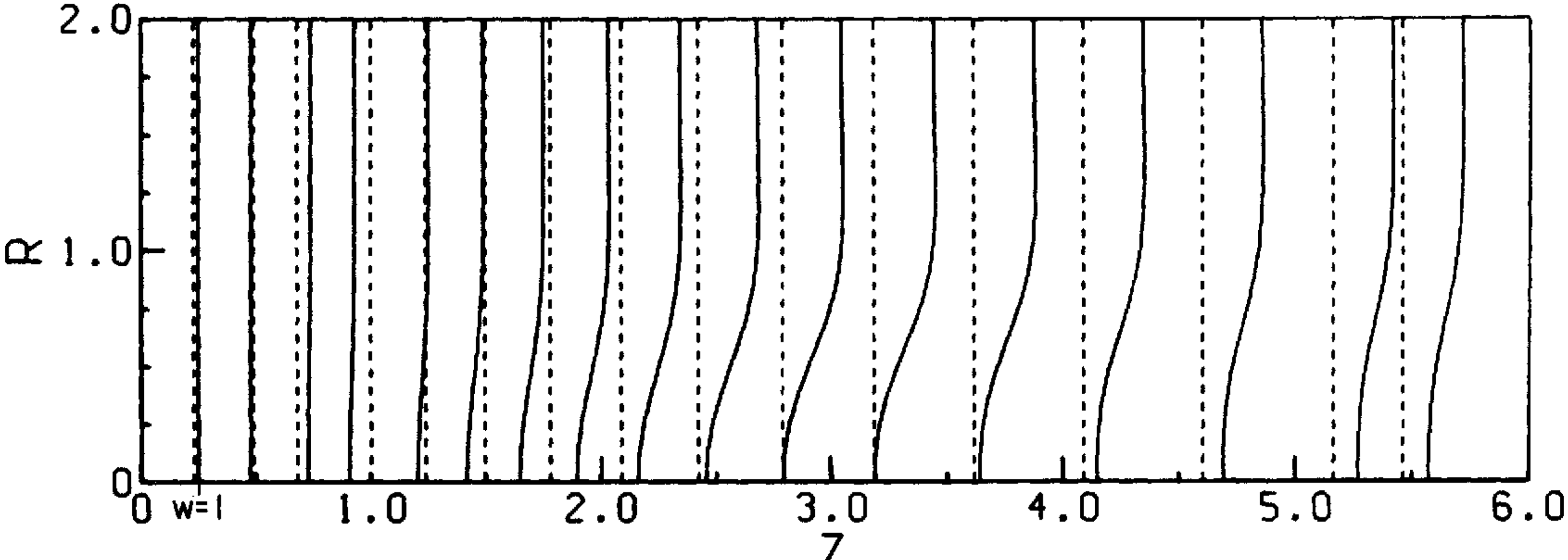

Fig. 8b. AXIAL VELOCITY PROFILES -- Re = 200, $\alpha = 1.0$, V = 0.8944

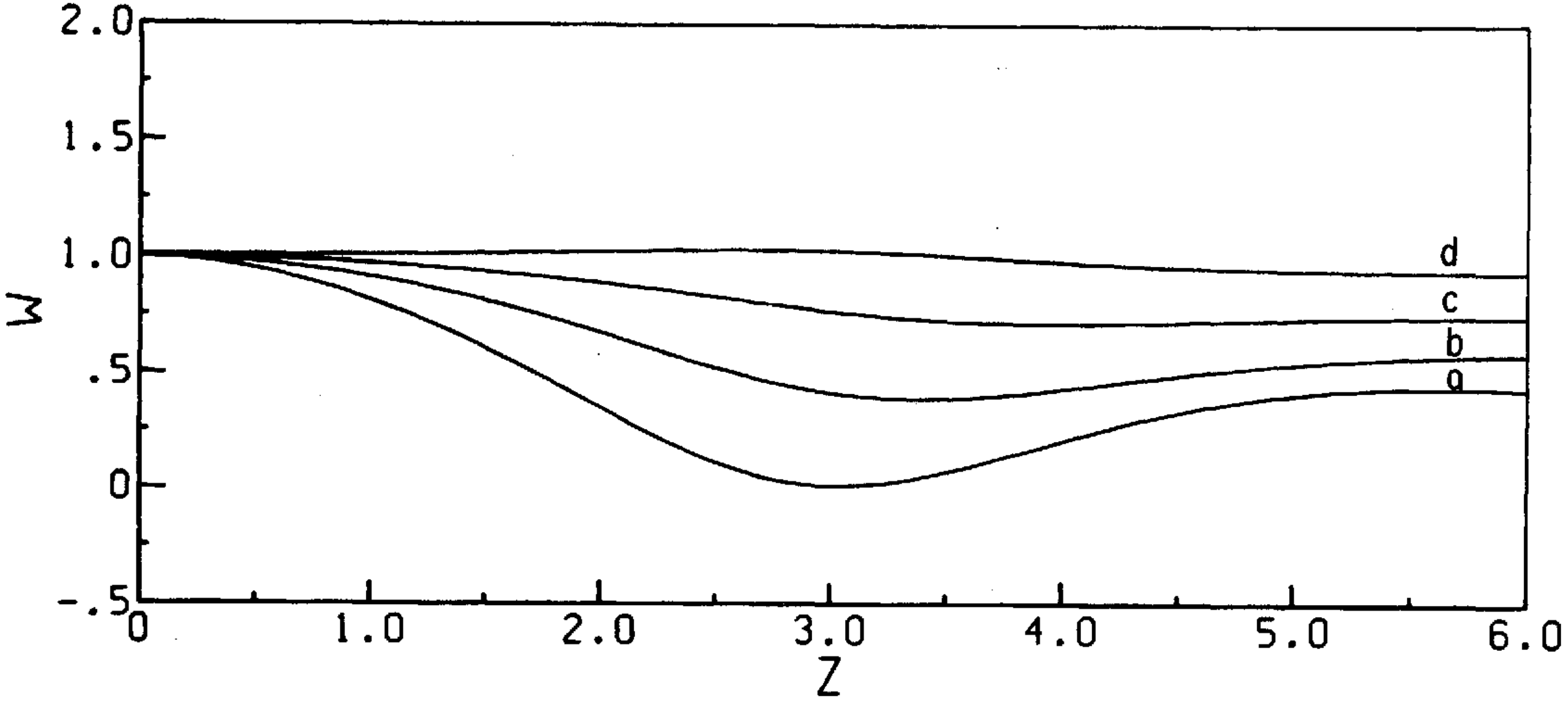

Fig. 8c. AXIAL VELOCITY VARIATION WITH z AT FIXED RADIAL POSITIONS -- Re = 200, α = 1.0, V = 0.8944
(a) r = 0 ; (b) r = 0.486 ; (c) r = 0.714 ; (d) r = 1.0

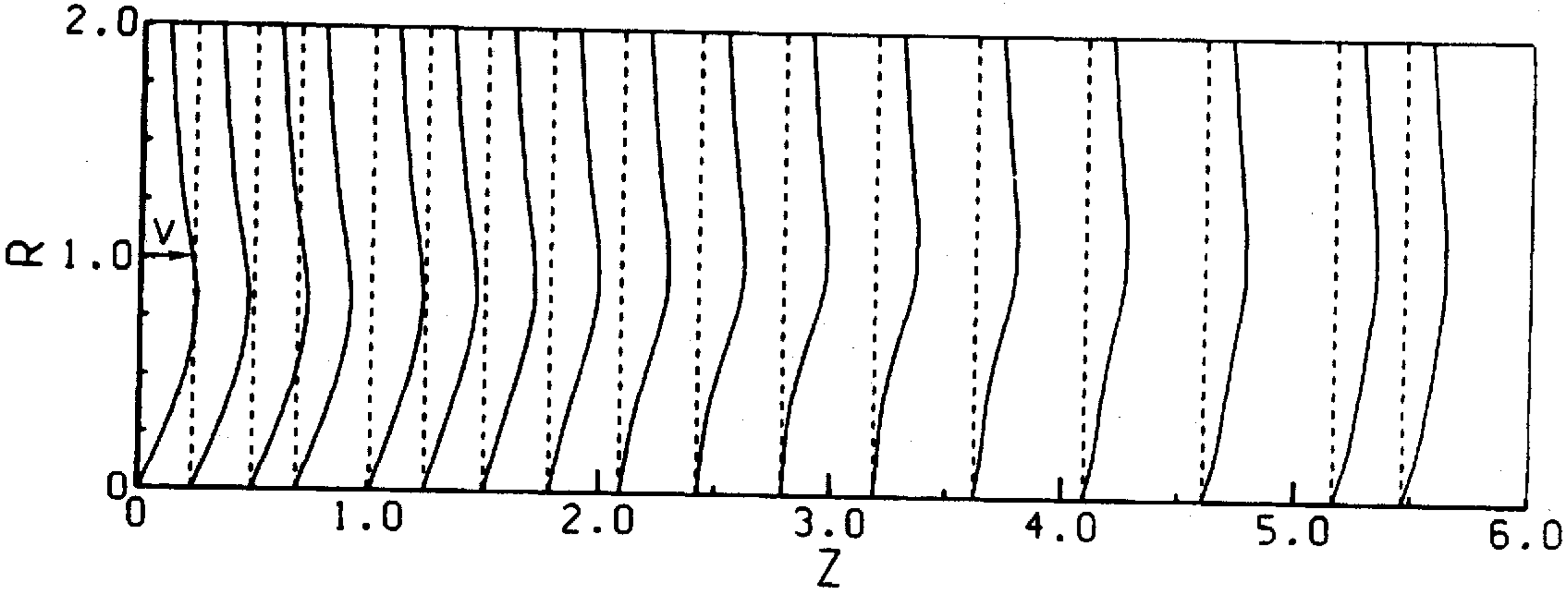

Fig. 8d. SWIRL VELOCITY PROFILES -- Re = 200, α = 1.0, V = 0.8944

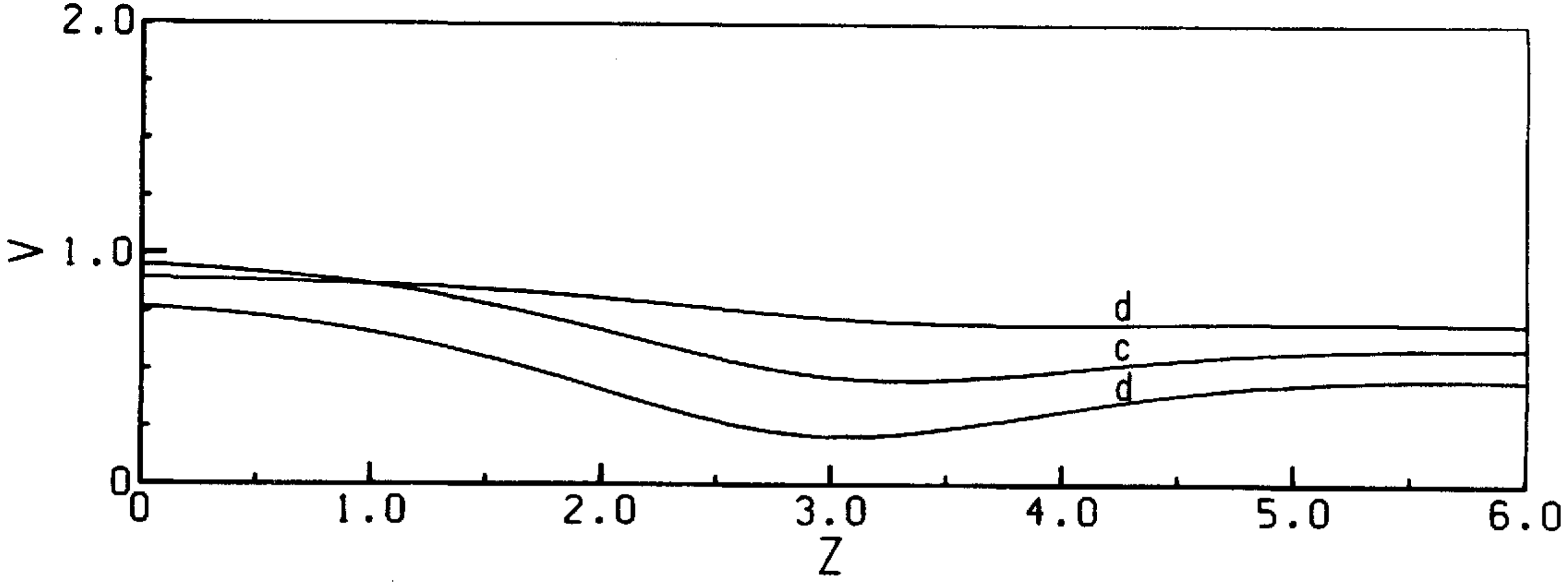

Fig. 8e. SWIRL VELOCITY VARIATION WITH z AT FIXED RADIAL POSITIONS -- Re = 200, α = 1.0, V = 0.894
(b) $r = 0.486$; (c) $r = 0.714$; (d) $r = 1.0$

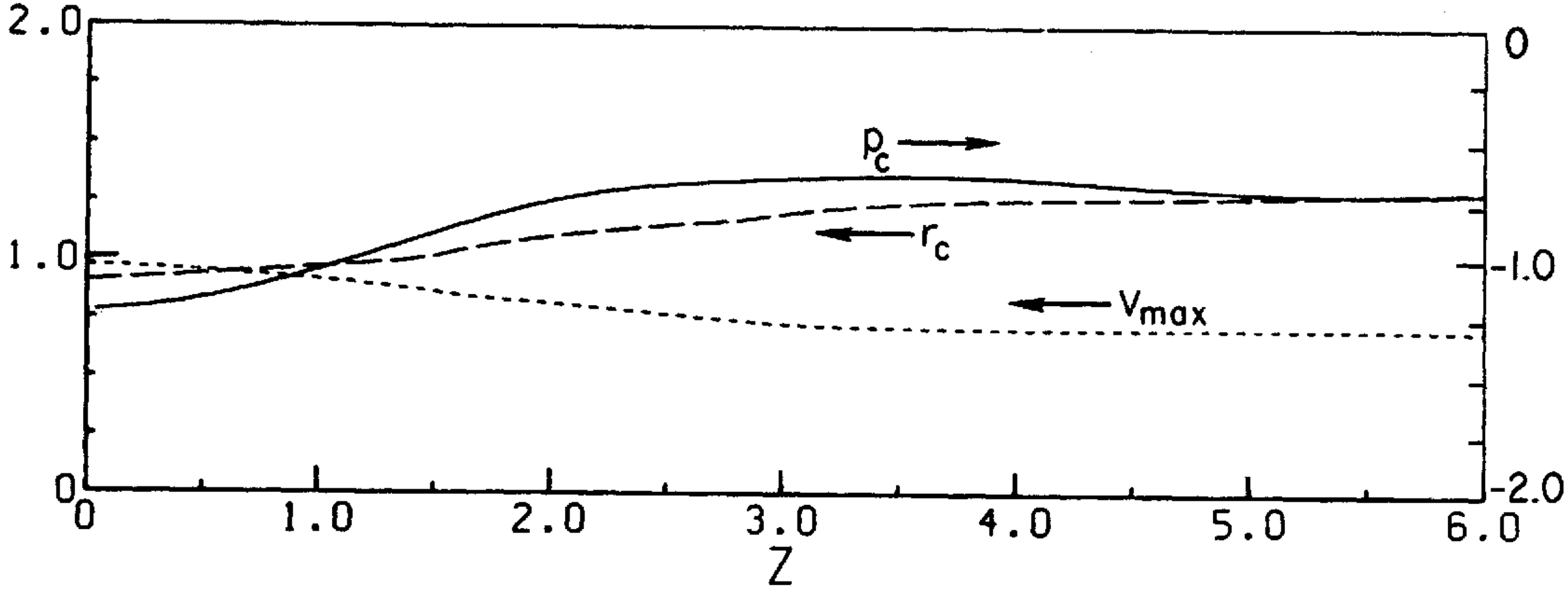

Fig. 8f. CORE PRESSURE NEAR AXIS, CORE RADIUS, AND MAXIMUM SWIRL VELOCITY vs. z

Re = 200, α = 1.0, V = 0.8944

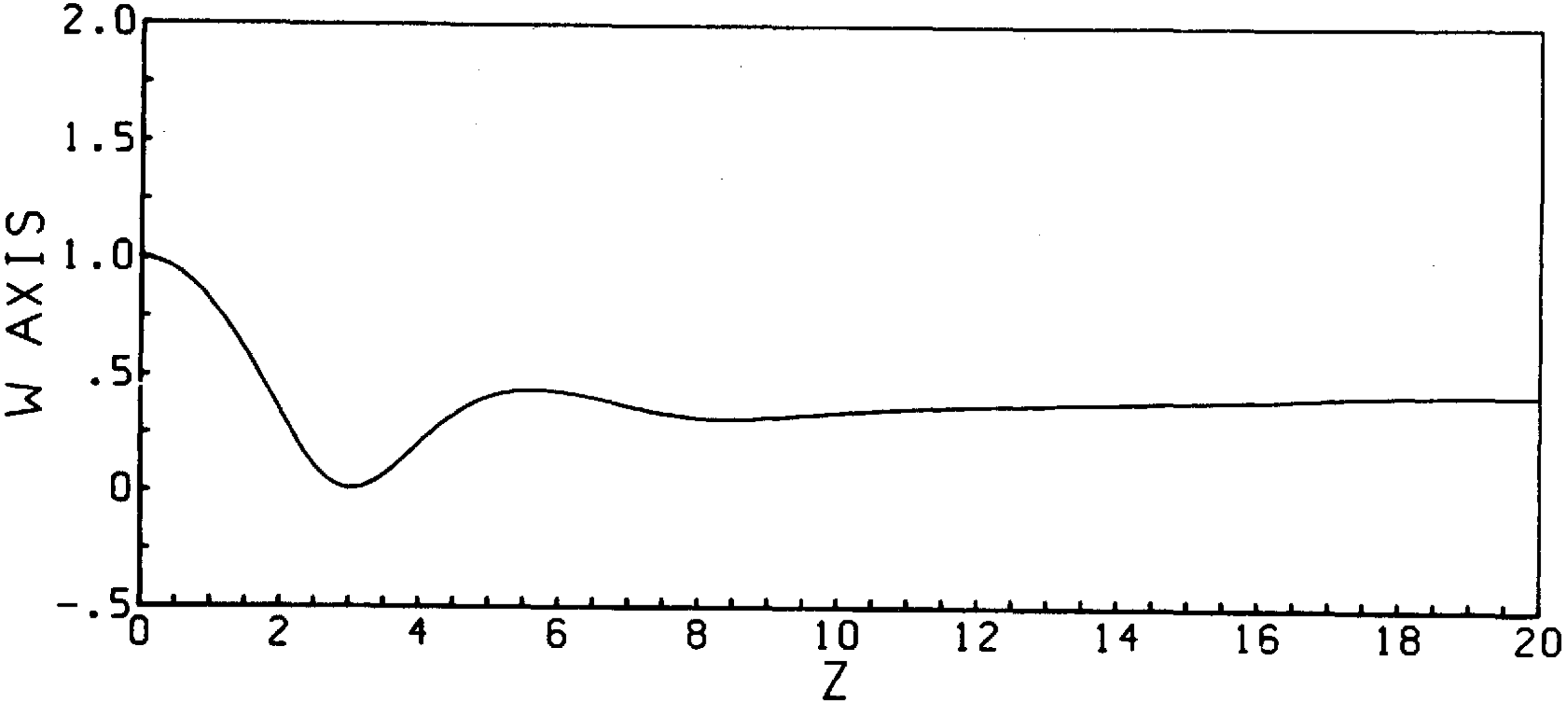

Fig. 8g. AXIAL VELOCITY ON AXIS vs z -- Re = 200, α = 1.0, V = 0.8944

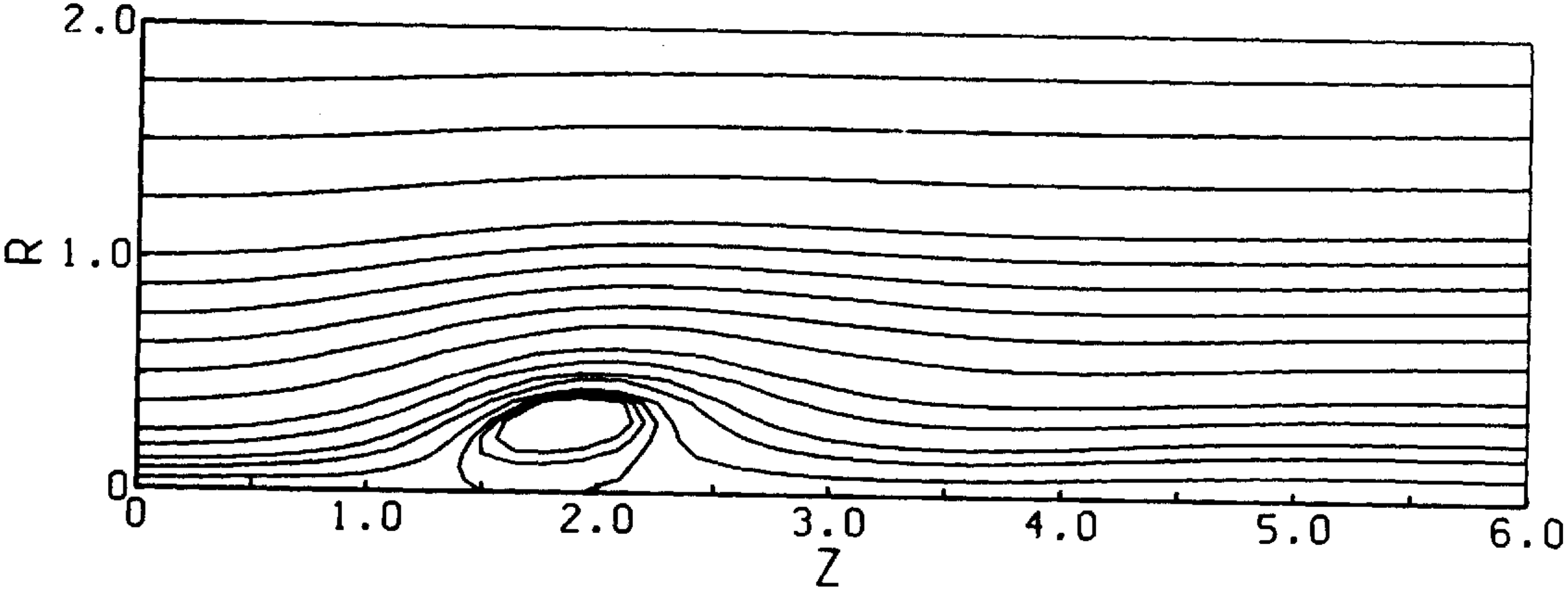

Fig. 9a. STREAM FUNCTION CONTOURS -- Re = 200, α = 1.0, V = 1.0

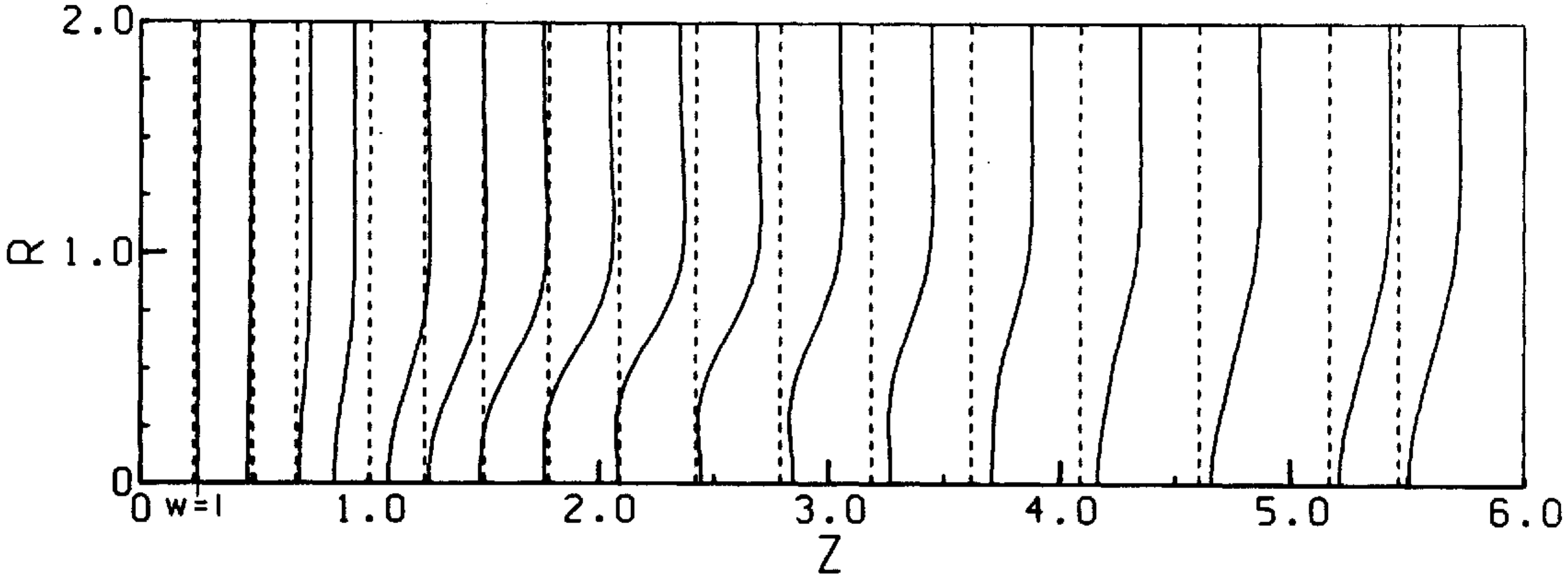

Fig. 9b. AXIAL VELOCITY PROFILES -- Re = 200, $\alpha = 1.0$, V = 1.0

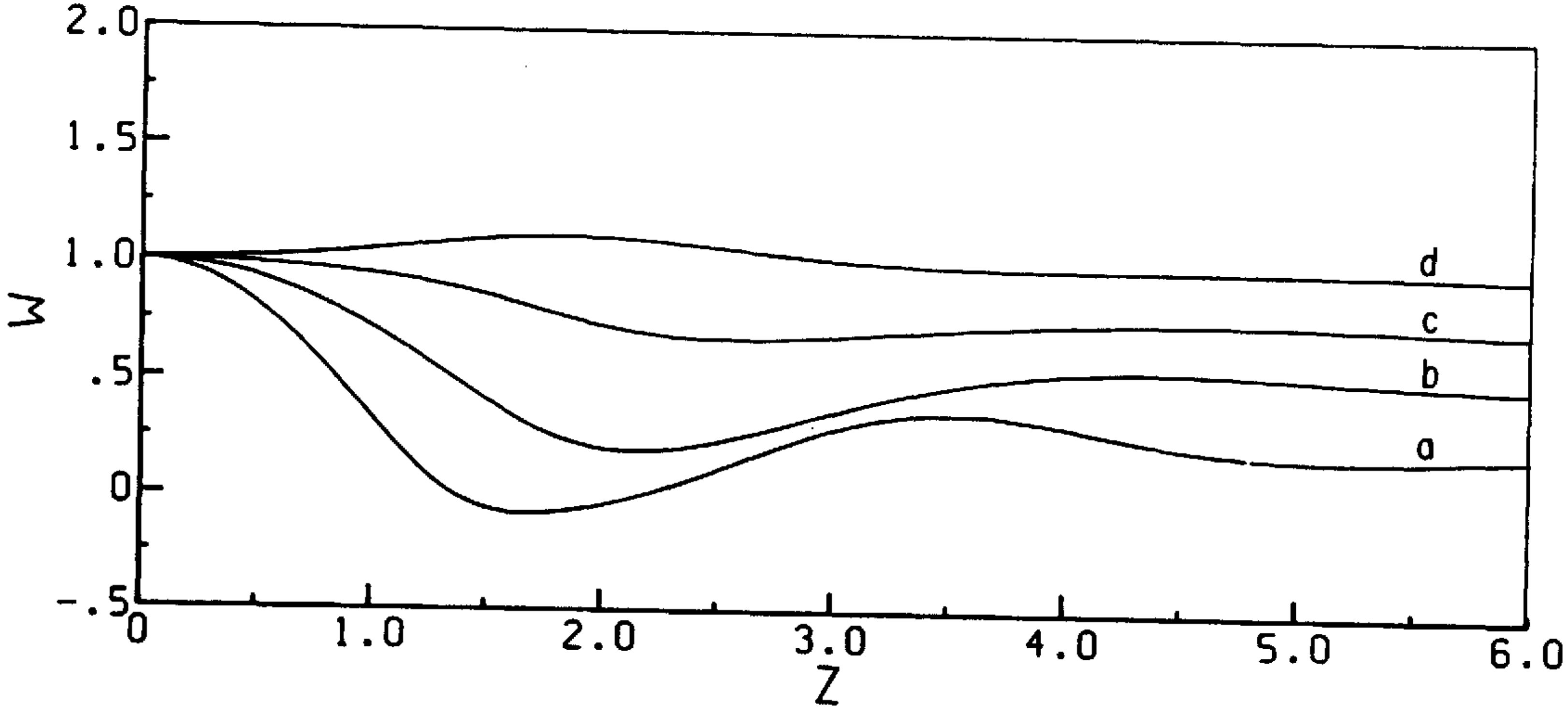

Fig. 9c. AXIAL VELOCITY VARIATION WITH z AT FIXED RADIAL POSITIONS -- $Re = 200$, $\alpha = 1.0$, $V = 1.0$
(a) $r = 0$; (b) $r = 0.486$; (c) $r = 0.714$; (d) $r = 1.0$

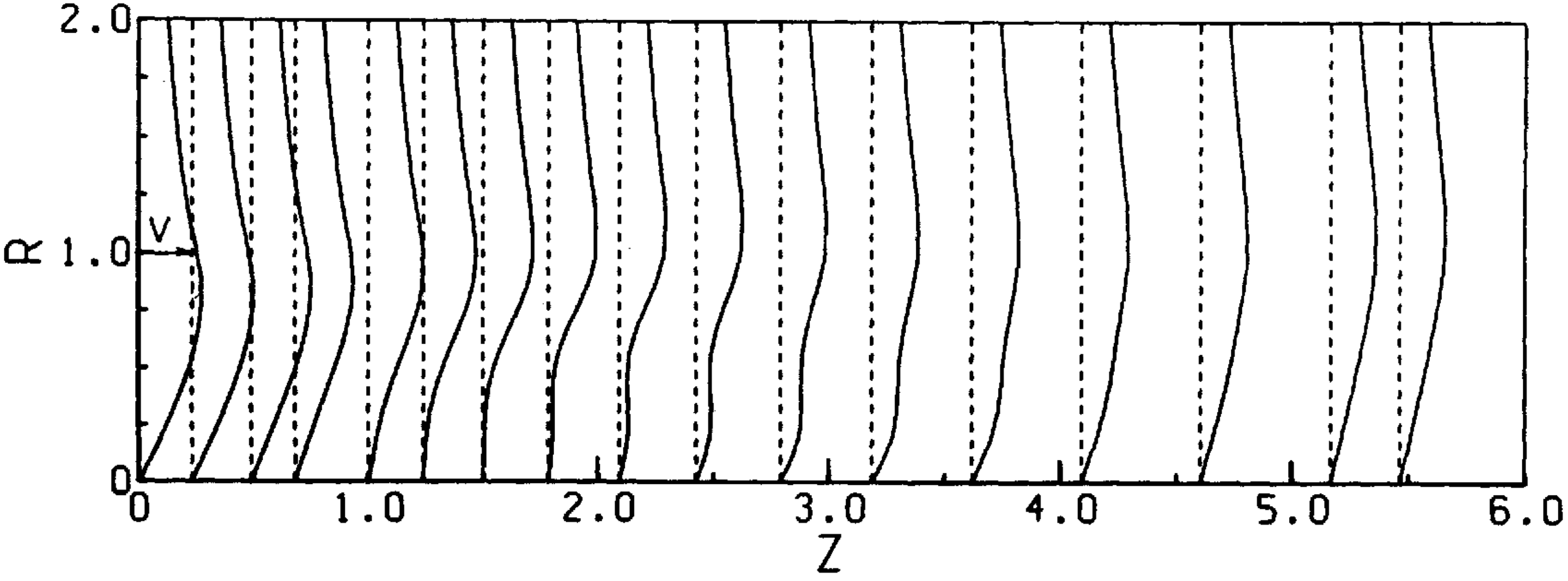

Fig. 9d. SWIRL VELOCITY PROFILES -- Re = 200, α = 1.0, V = 1.0

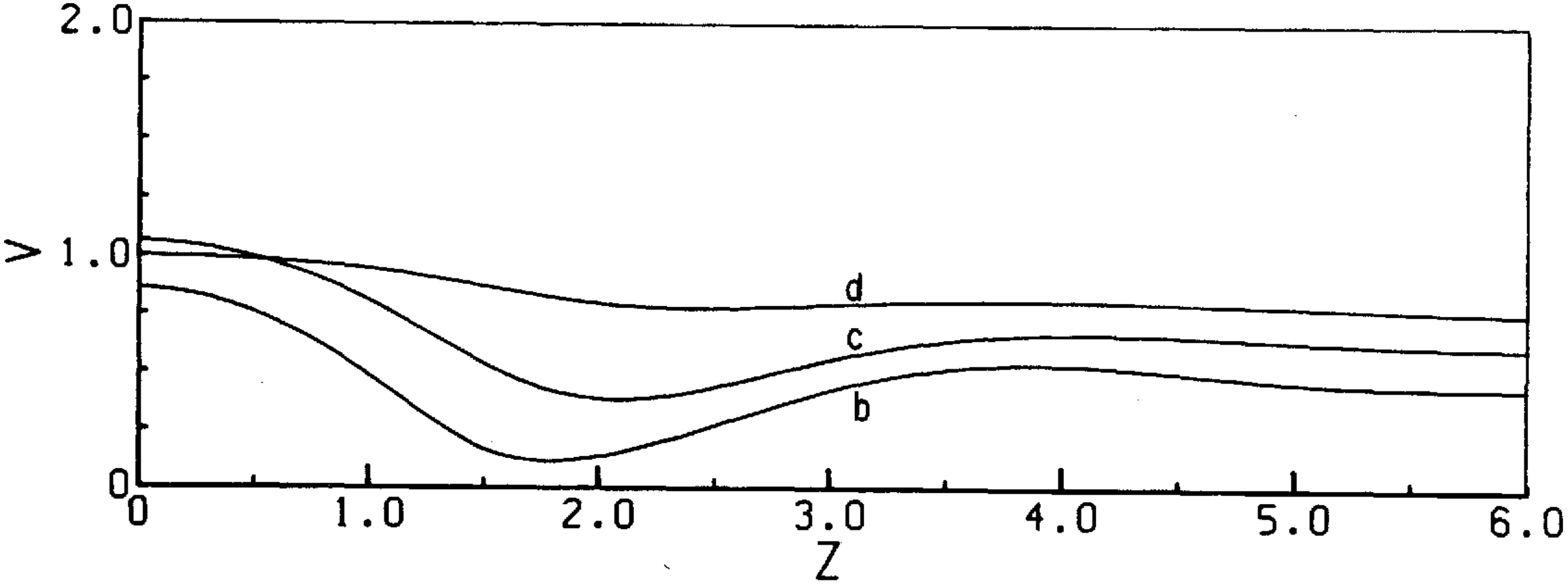

Fig. 9e. SWIRL VELOCITY VARIATION WITH z AT FIXED RADIAL POSITIONS -- Re = 200, α = 1.0, V = 1.0
(b) r = 0.486 ; (c) r = 0.714 ; (d) r = 1.0

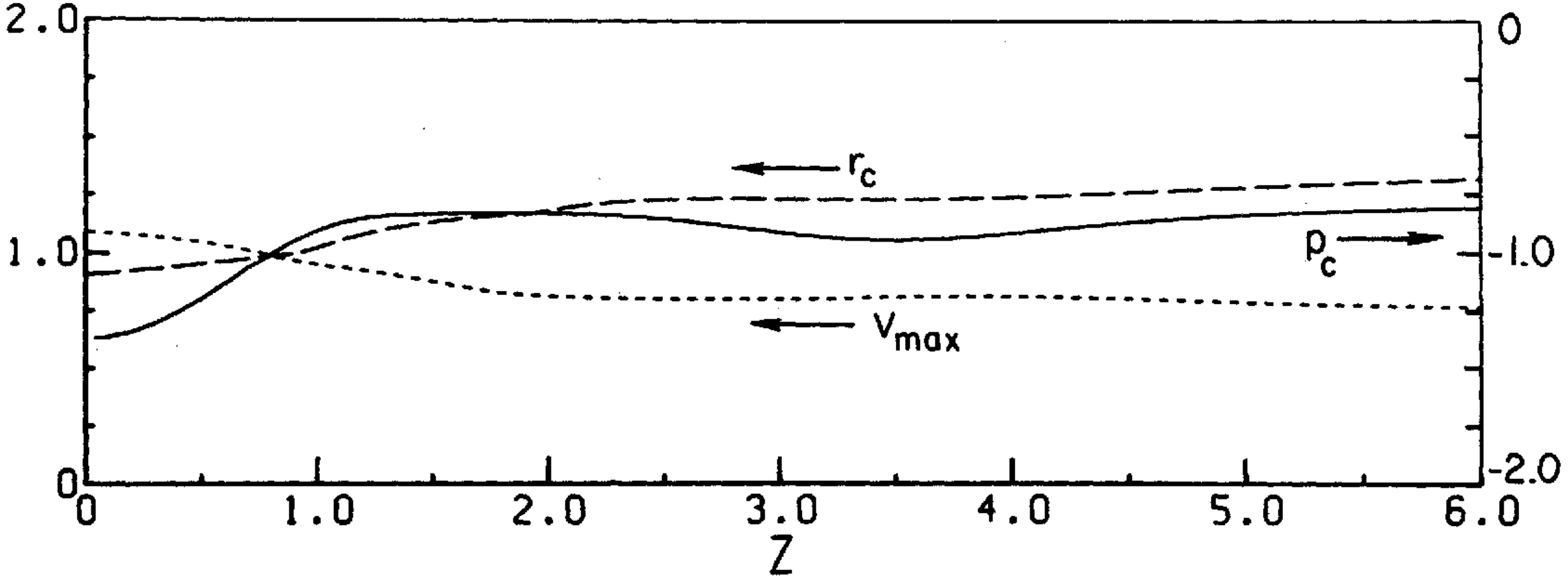

Fig. 9f. CORE PRESSURE NEAR AXIS, CORE RADIUS, AND MAXIMUM SWIRL VELOCITY vs. z
Re = 200,R α = 1.0, V = 1.0

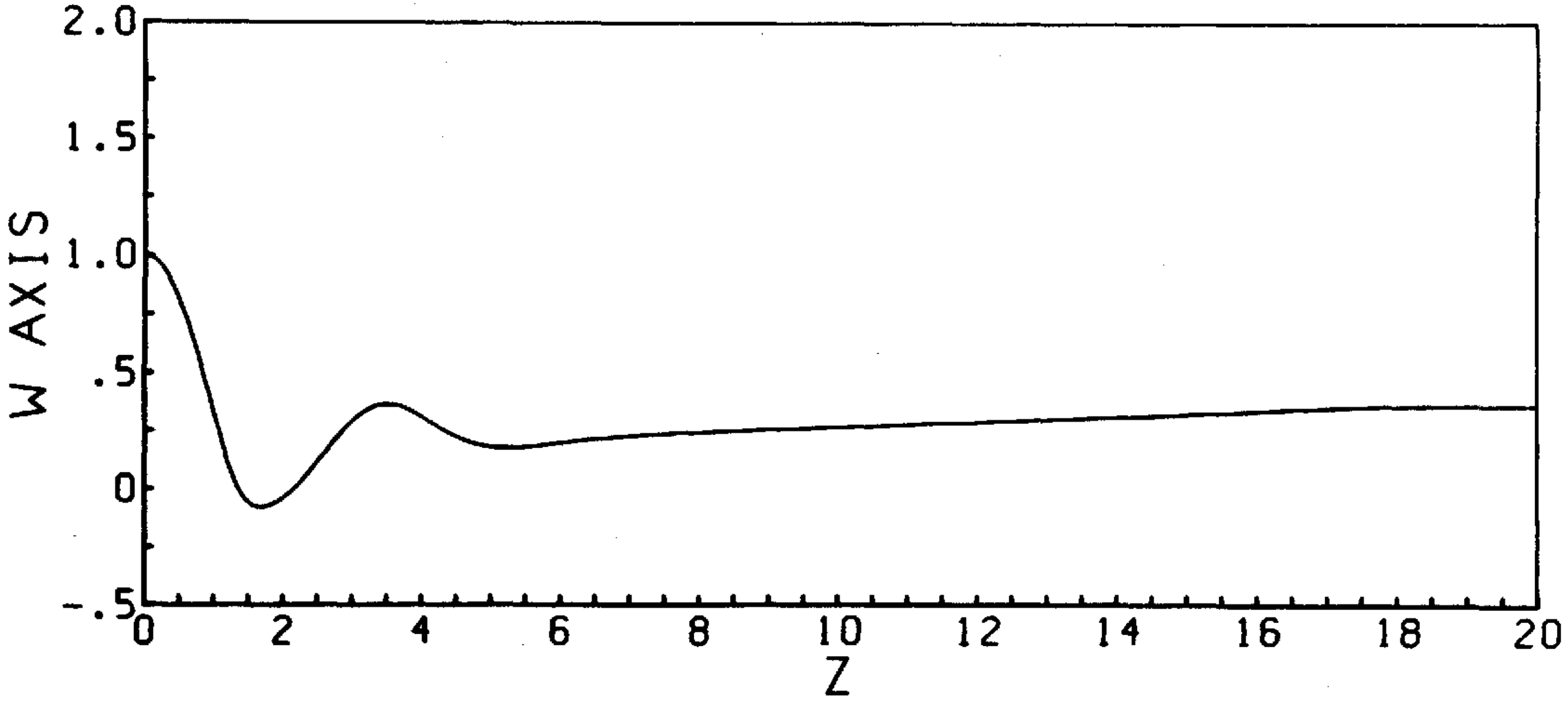

Fig. 9g. AXIAL VELOCITY ON AXIS vs. z -- Re = 200, α = 1.0, V = 1.0

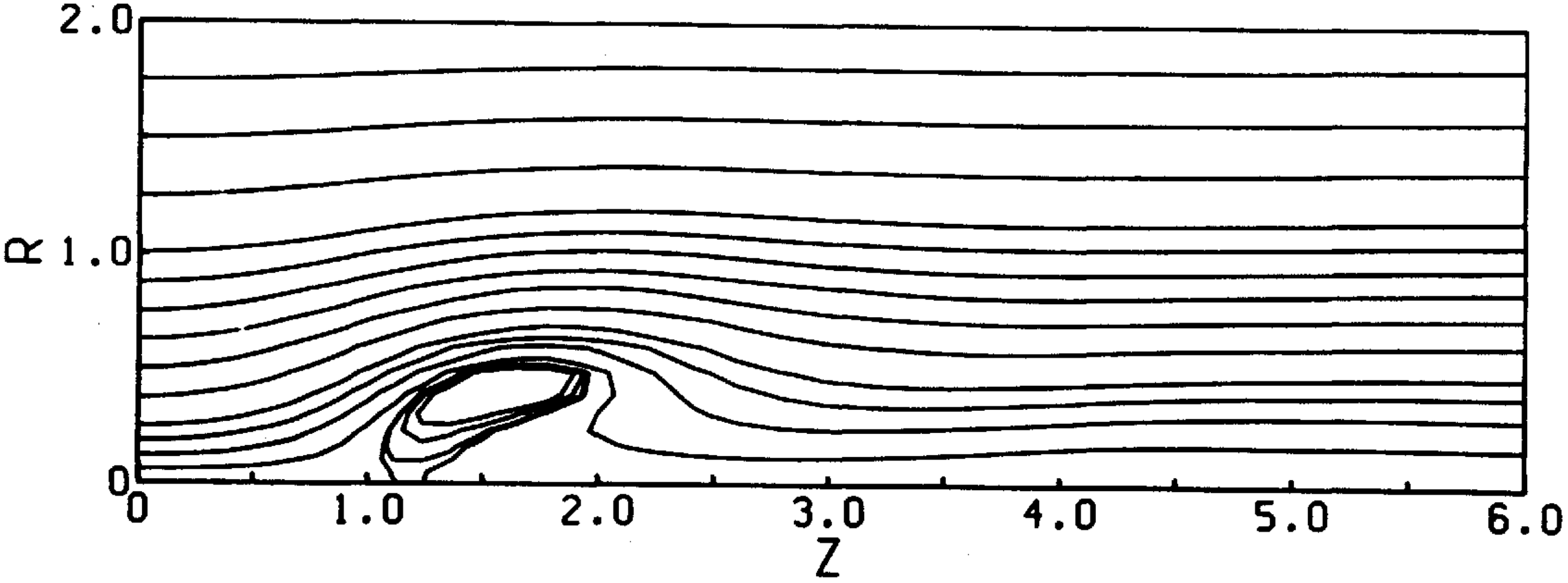

Fig. 10a. STREAM FUNCTION CONTOURS -- Re = 200, α = 1.0, V = 1.095

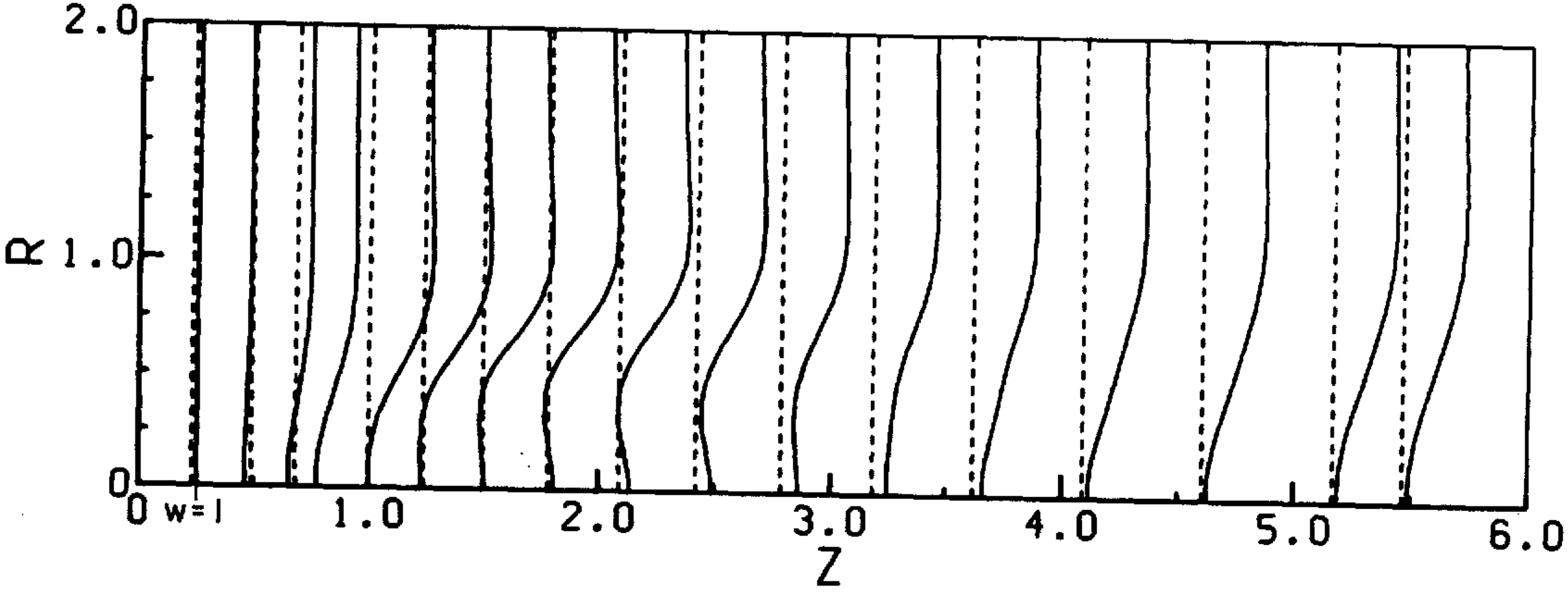

Fig. 10b. AXIAL VELOCITY PROFILES -- Re = 200, α = 1.0, V = 1.095

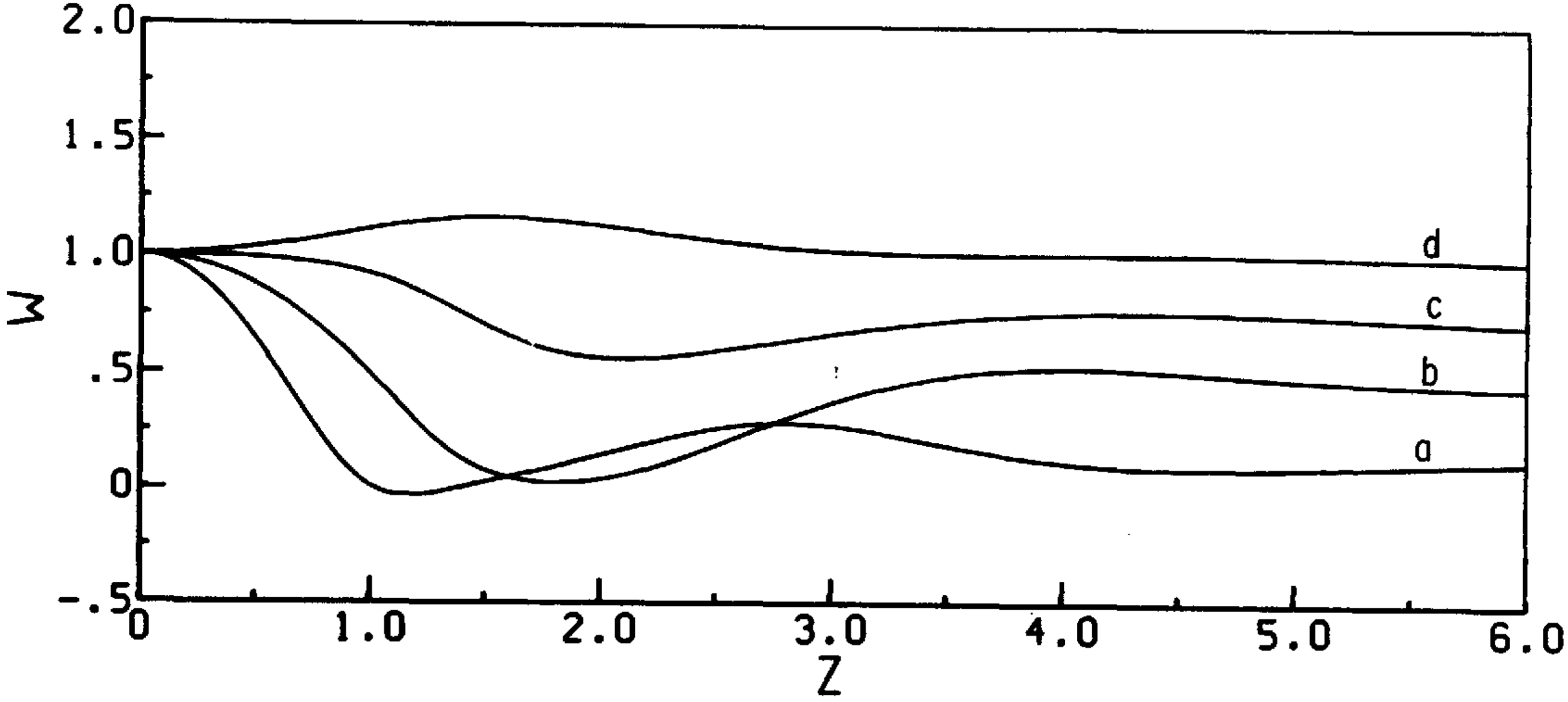

Fig. 10c. AXIAL VELOCITY VARIATION WITH z AT FIXED RADIAL POSITIONS -- Re = 200, α = 1.0, V = 1.095
(a) r = 0 ; (b) r = 0.486 ; (c) r = 0.714 ; (d) r = 1.0

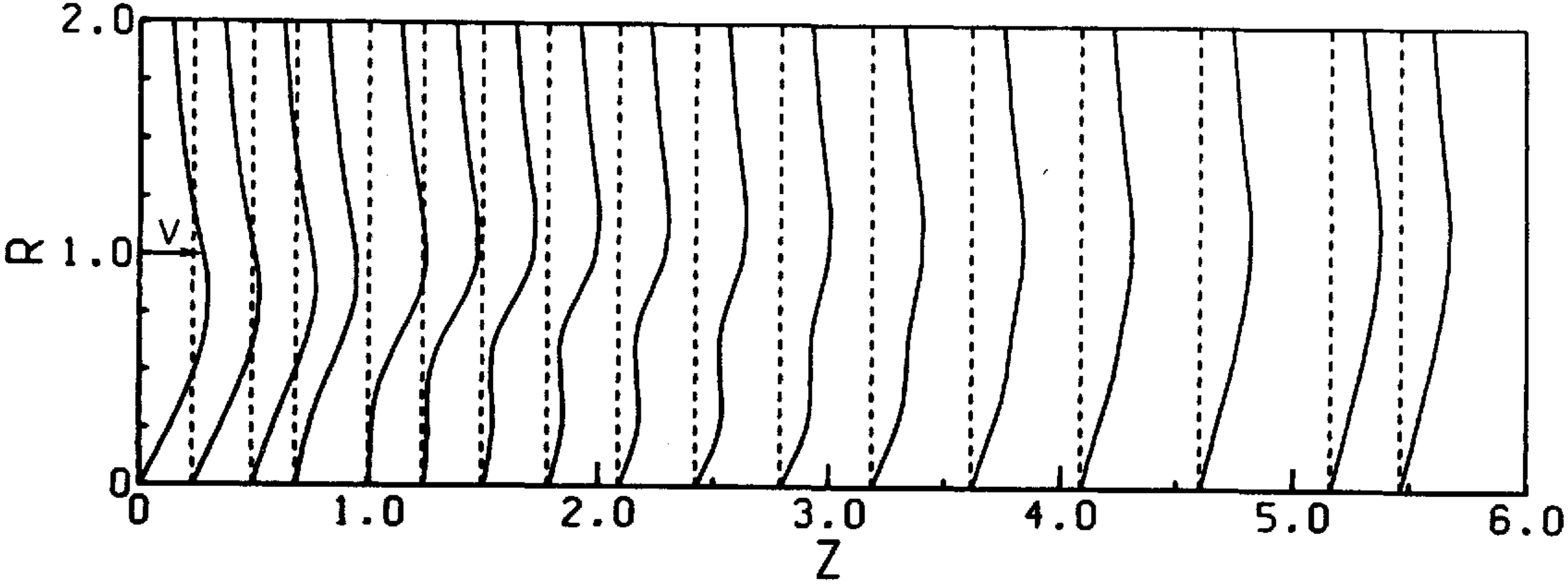

Fig. 10d. SWIRL VELOCITY PROFILES -- Re = 200, α = 1.0, V = 1.095

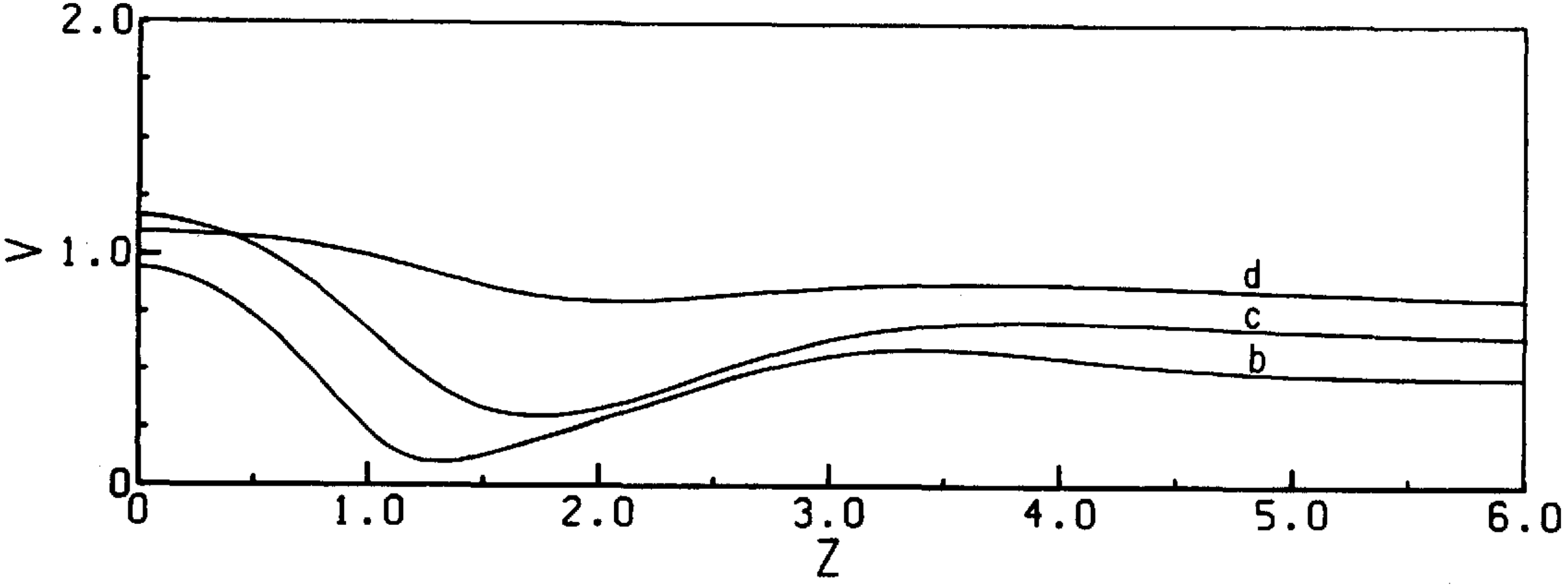

Fig. 10e. SWIRL VELOCITY VARIATION WITH z AT FIXED RADIAL POSITIONS -- Re = 200, α = 1.0, V = 1.095
(b) = 0.486 ; (c) r = 0.714 ; (d) r = 1.0

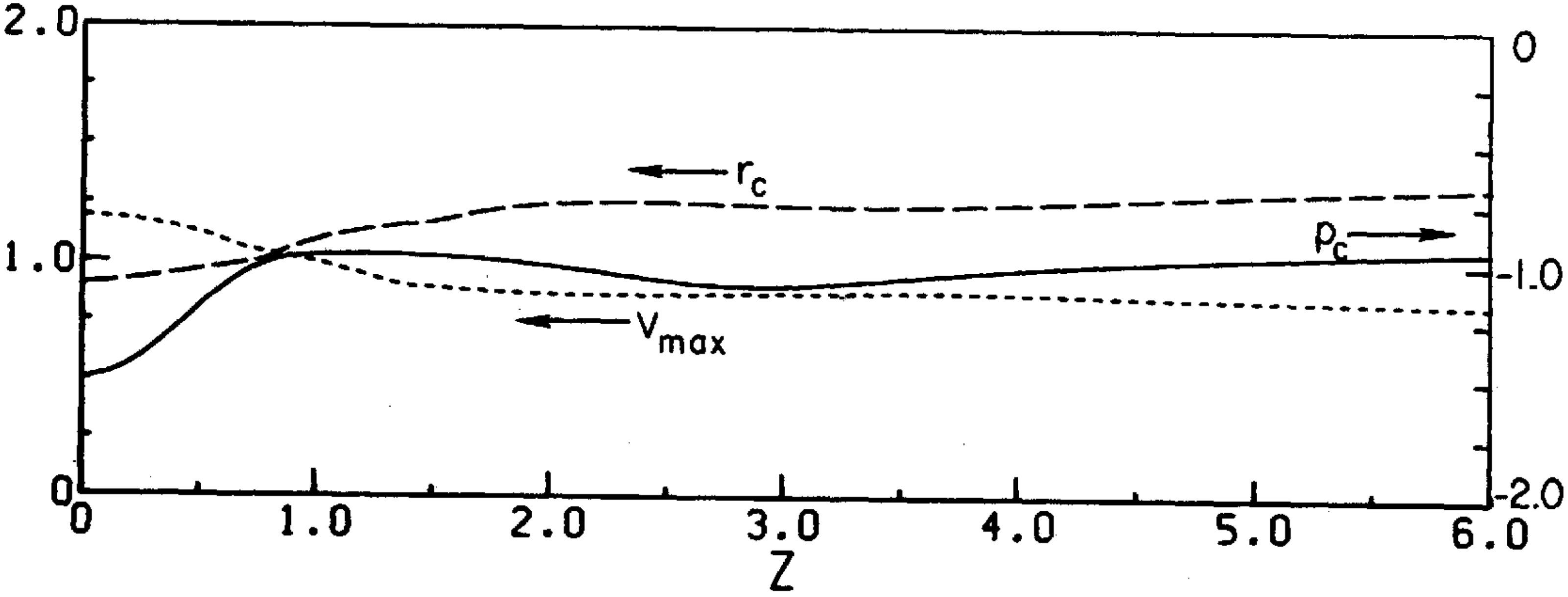

Fig. 10f. CORE PRESSURE NEAR AXIS, CORE RADIUS, AND MAXIMUM SWIRL VELOCITY vs. z
Re = 200, α = 1.0, V = 1.095

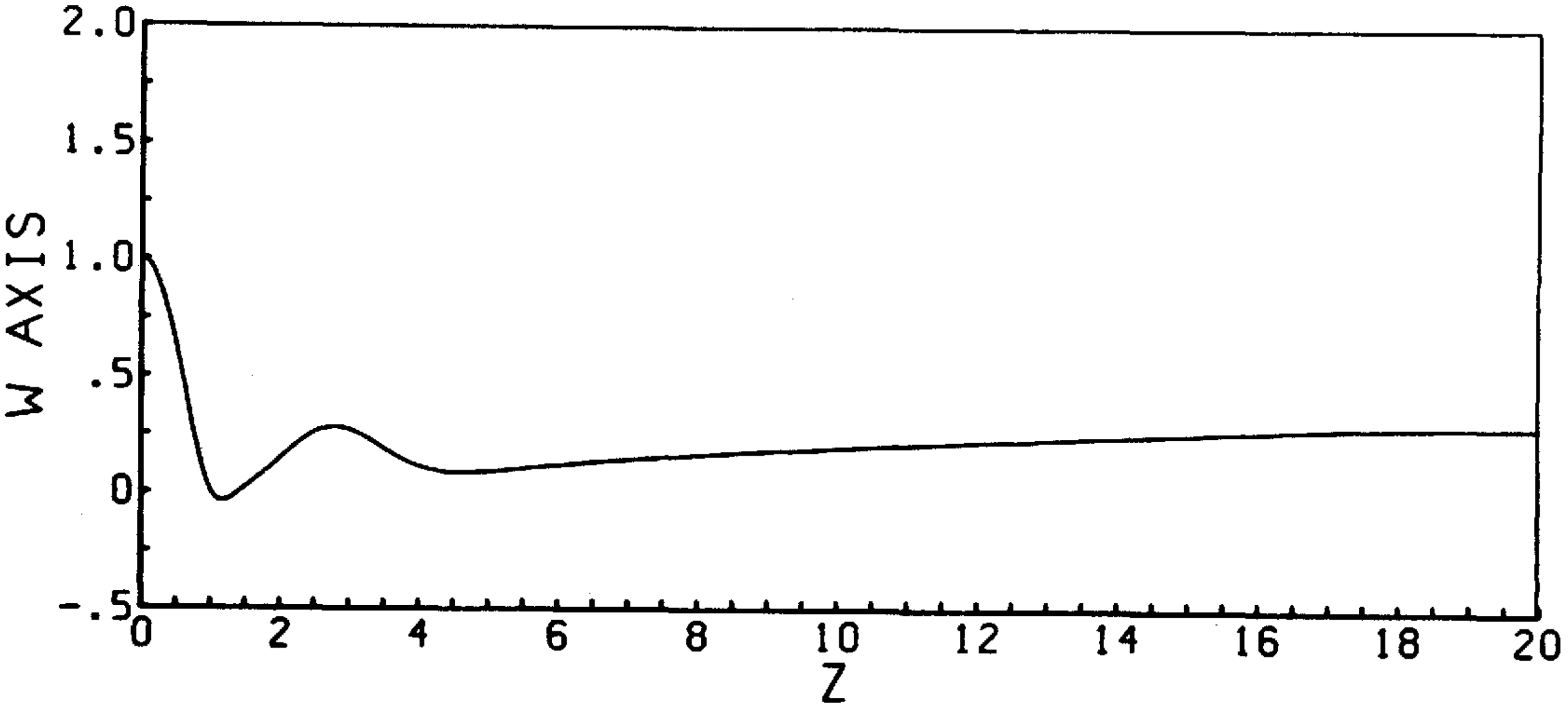

Fig. 10g. AXIAL VELOCITY ON AXIS vs. z -- Re = 200, $\alpha = 1.0$, V = 1.095

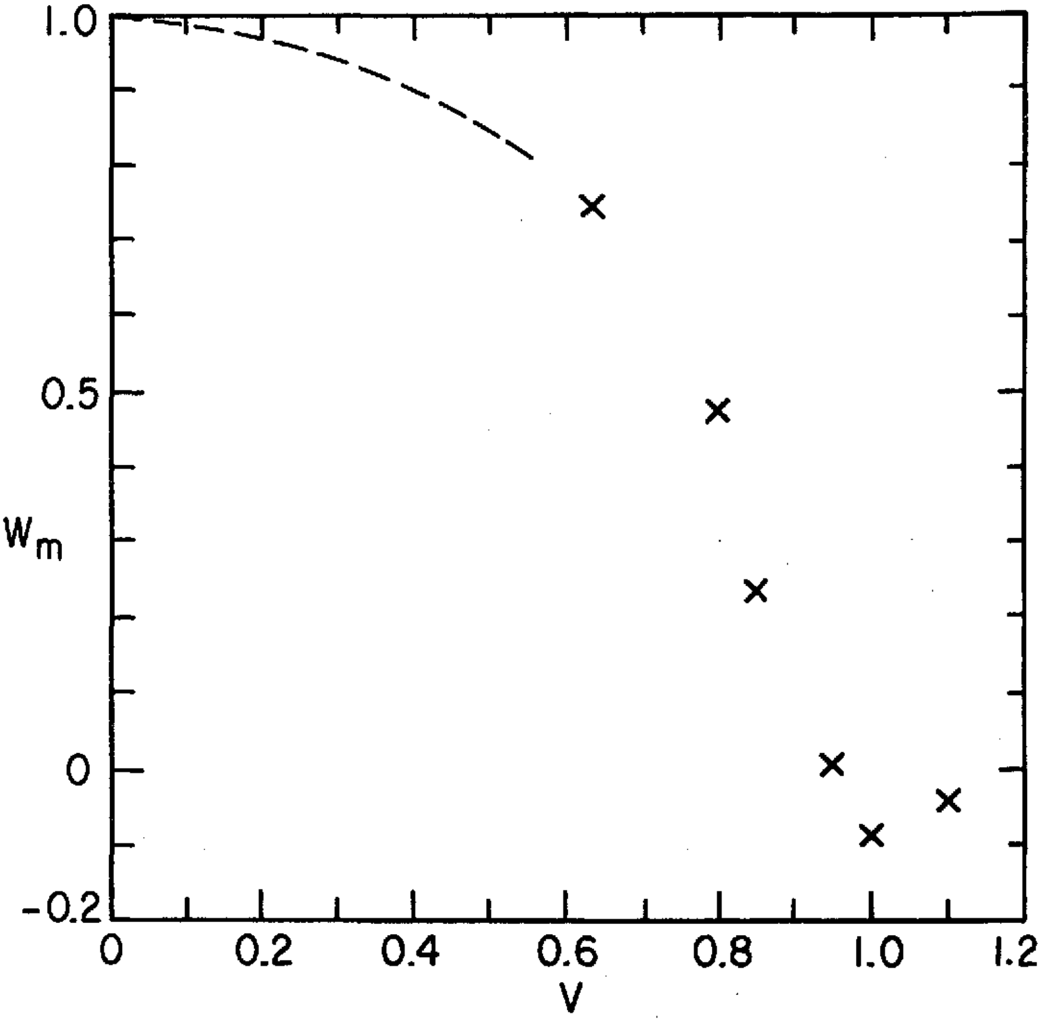

MINIMUM AXIAL VELOCITY AT AXIS VS. V
Re = 200, $\alpha = 1$

Fig. 11.

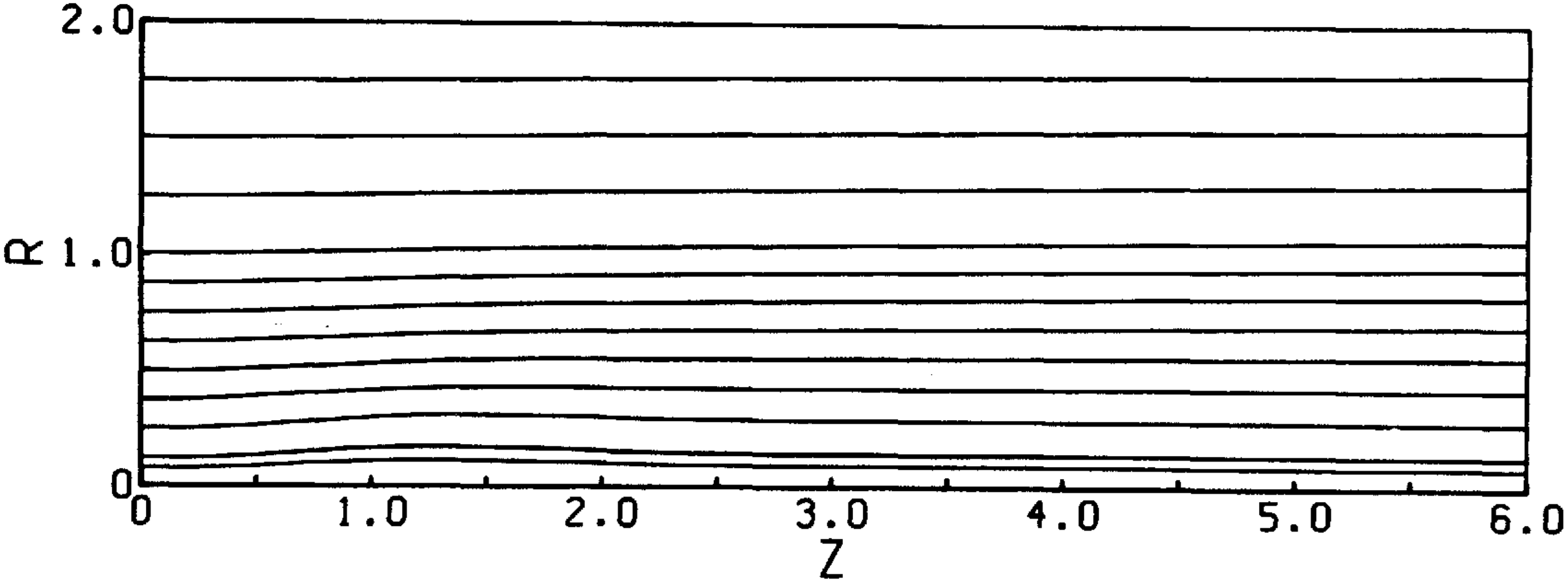

Fig. 12. STREAM FUNCTION CONTOURS -- Re = 200, $\alpha = 0.3$, V = 0.774

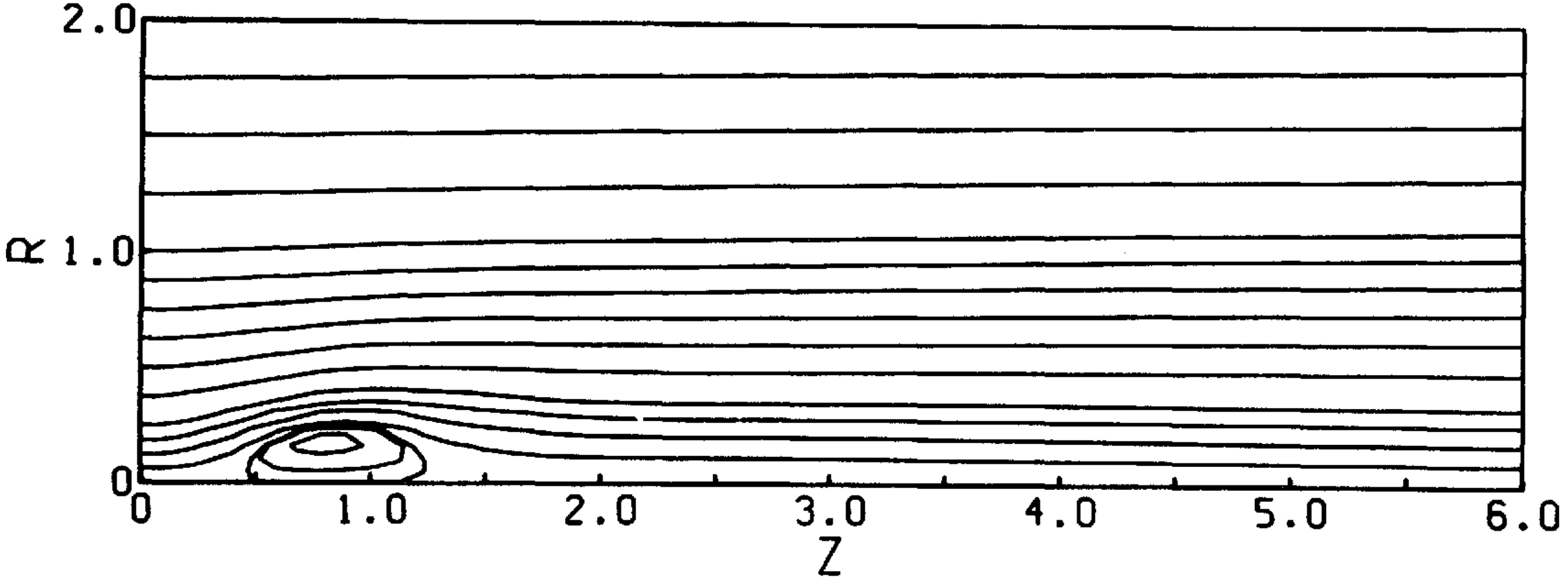

Fig. 13. STREAM FUNCTION CONTOURS -- Re = 200, α = 0.3, V = 0.8944

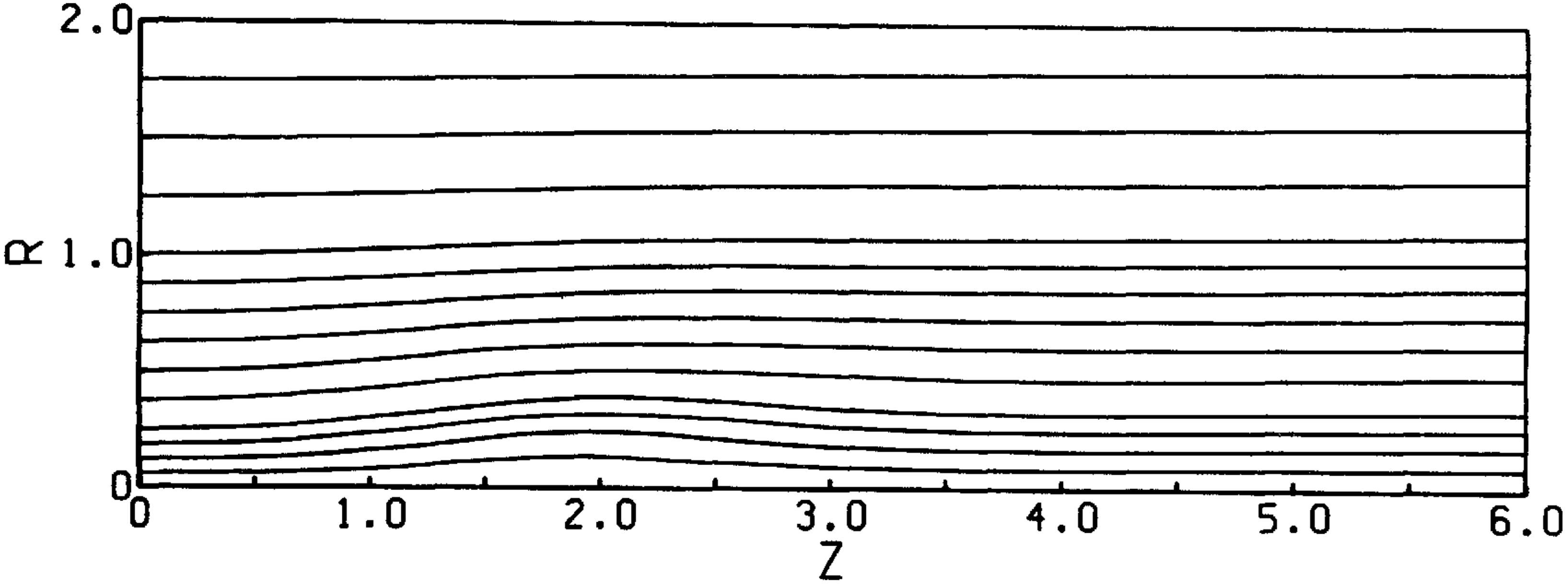

Fig. 14. STREAM FUNCTION CONTOURS -- Re = 200, α = 0.6, V = 0.82

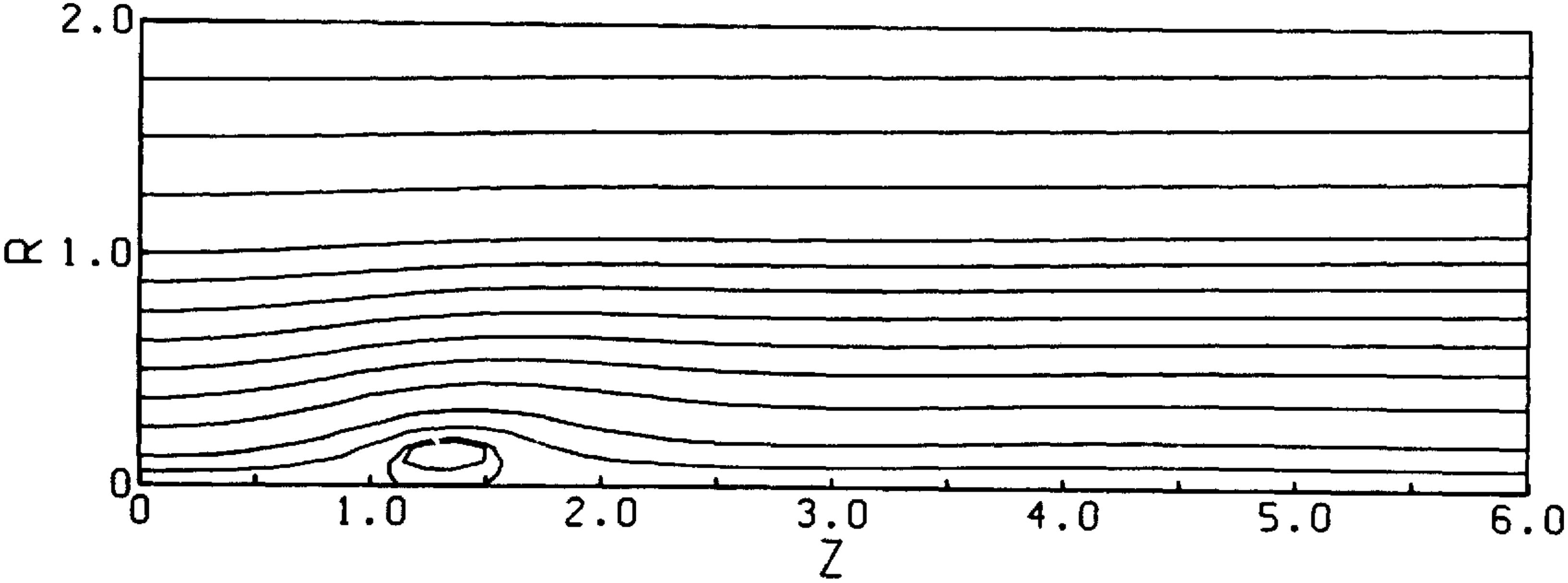

Fig. 15. STREAM FUNCTION CONTOURS -- Re = 200, $\alpha \approx 0.6$, V = 0.8944

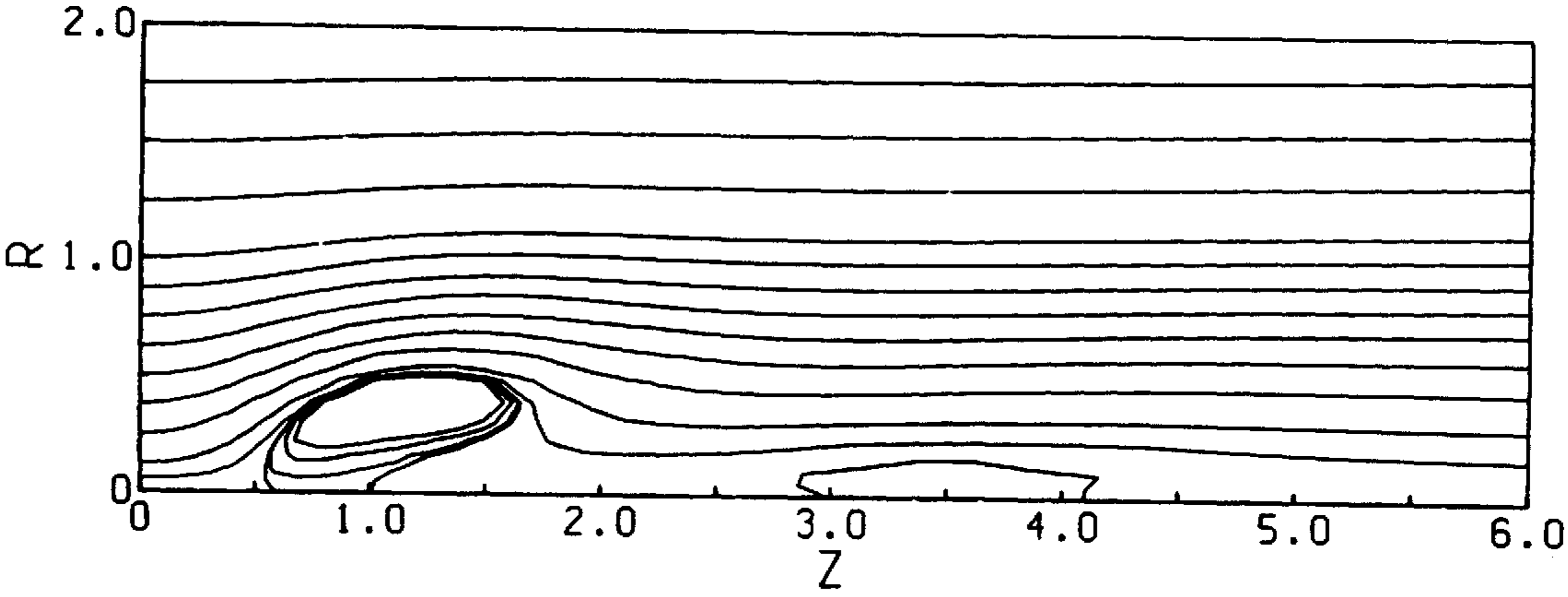

Fig. 16a. STREAM FUNCTION CONTOURS -- Re = 200, $\alpha = 0.6$, V = 1.095

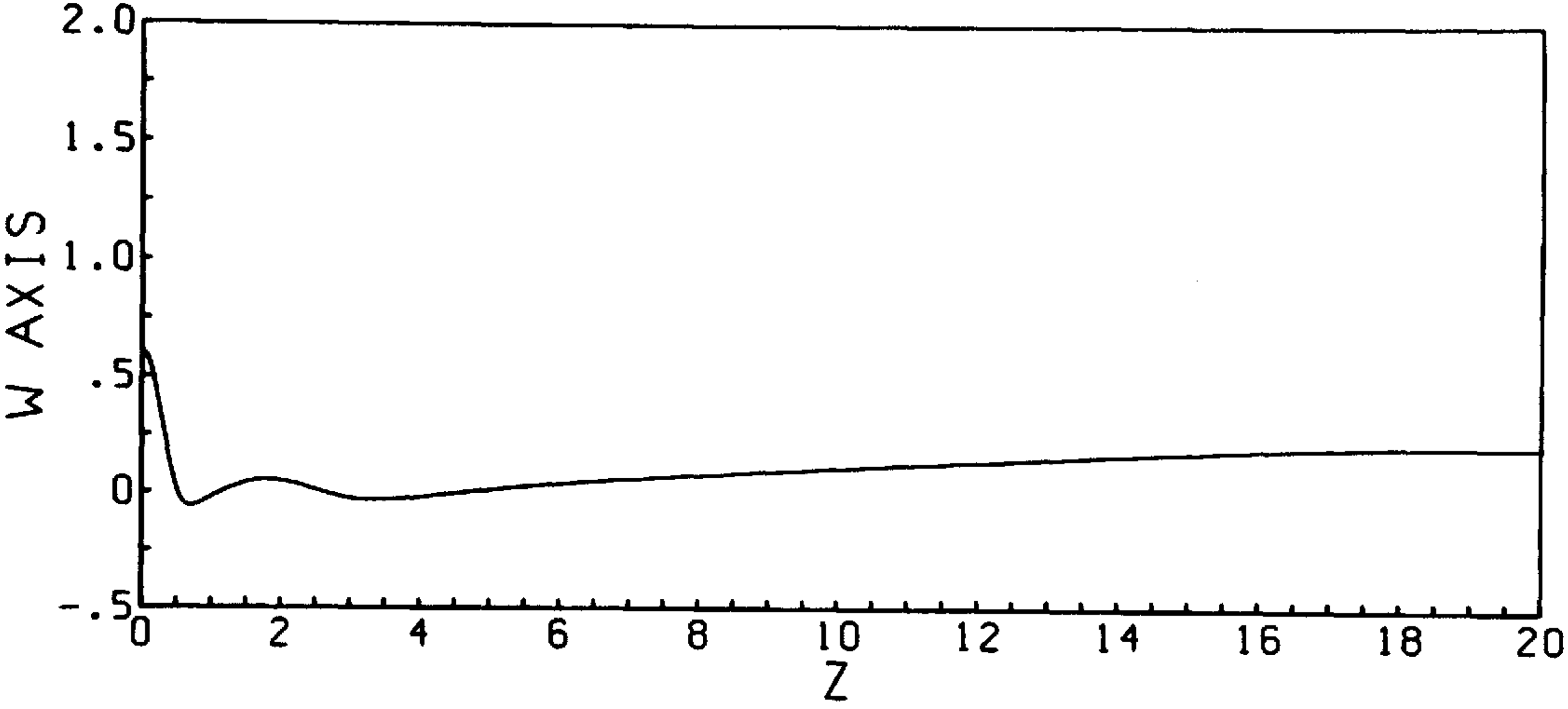

Fig. 16b. AXIAL VELOCITY ON AXIS vs. z -- Re = 200, $\alpha = 0.6$, V = 1.095

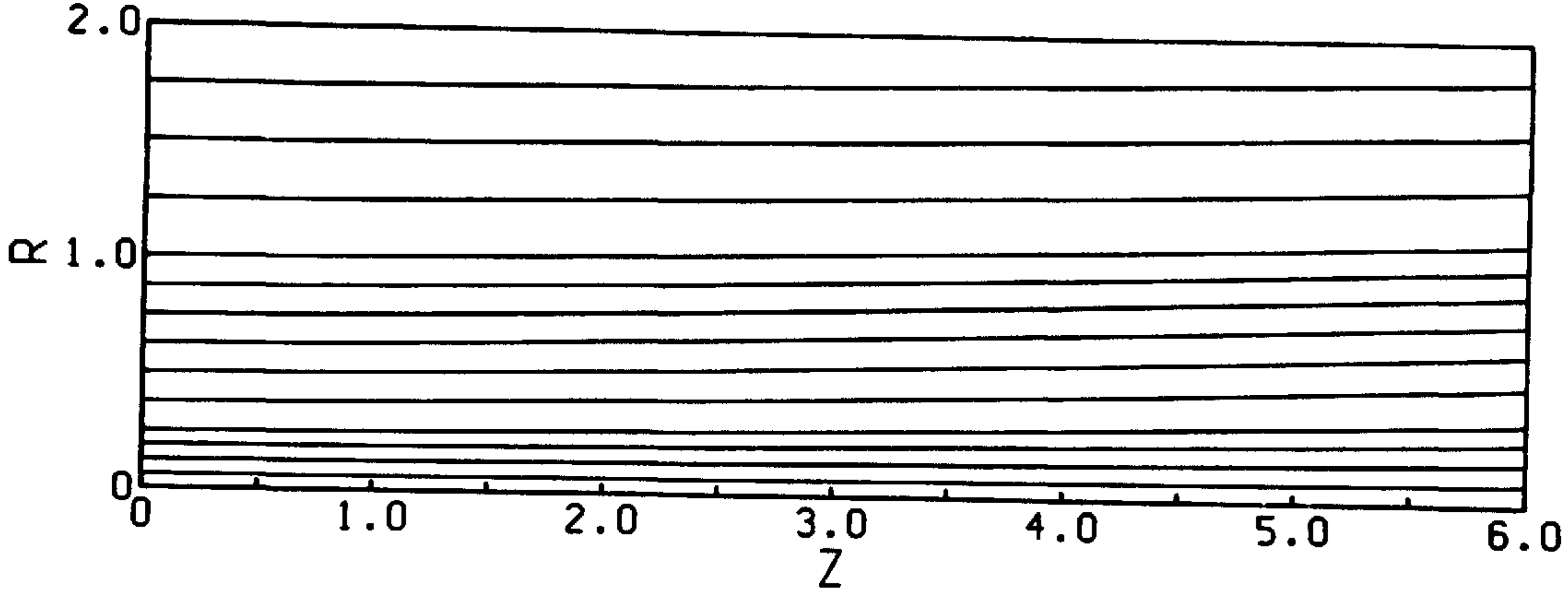

Fig. 17. STREAM FUNCTION CONTOURS -- Re = 200, α = 1.4, V = 0.95

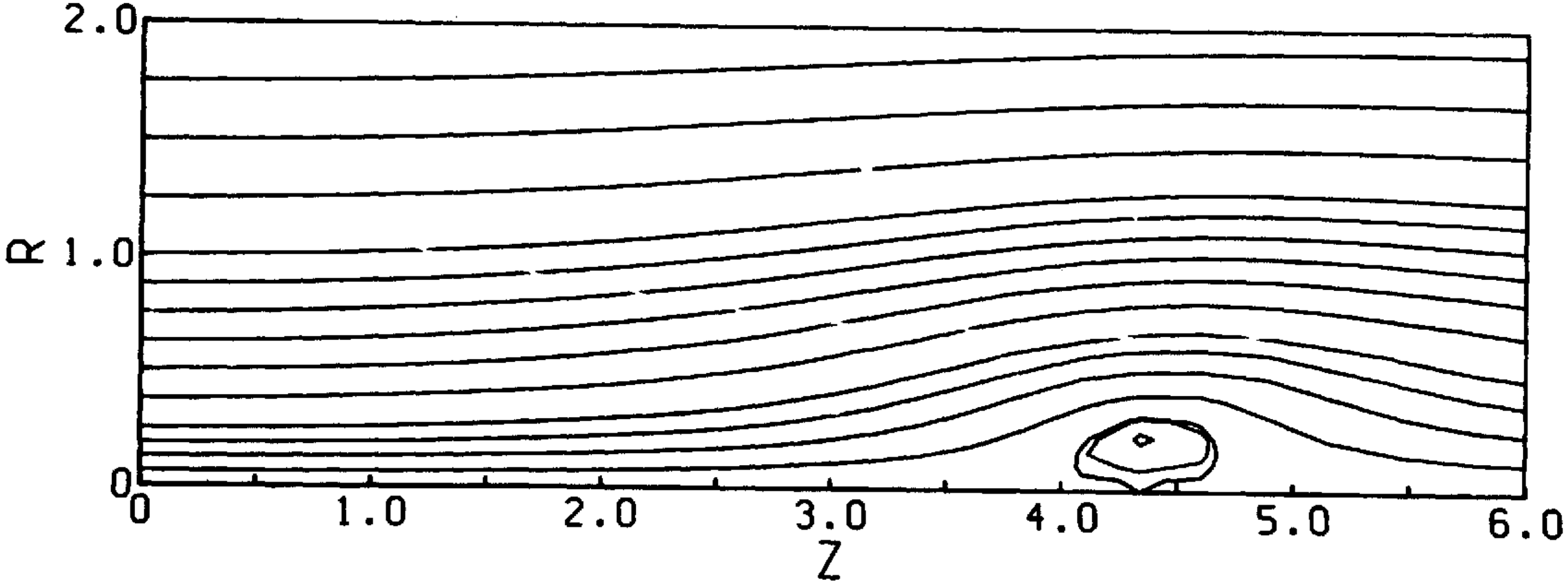

Fig. 18. STREAM FUNCTION CONTOURS -- Re = 200, $\alpha = 1.4$, V = 1.0

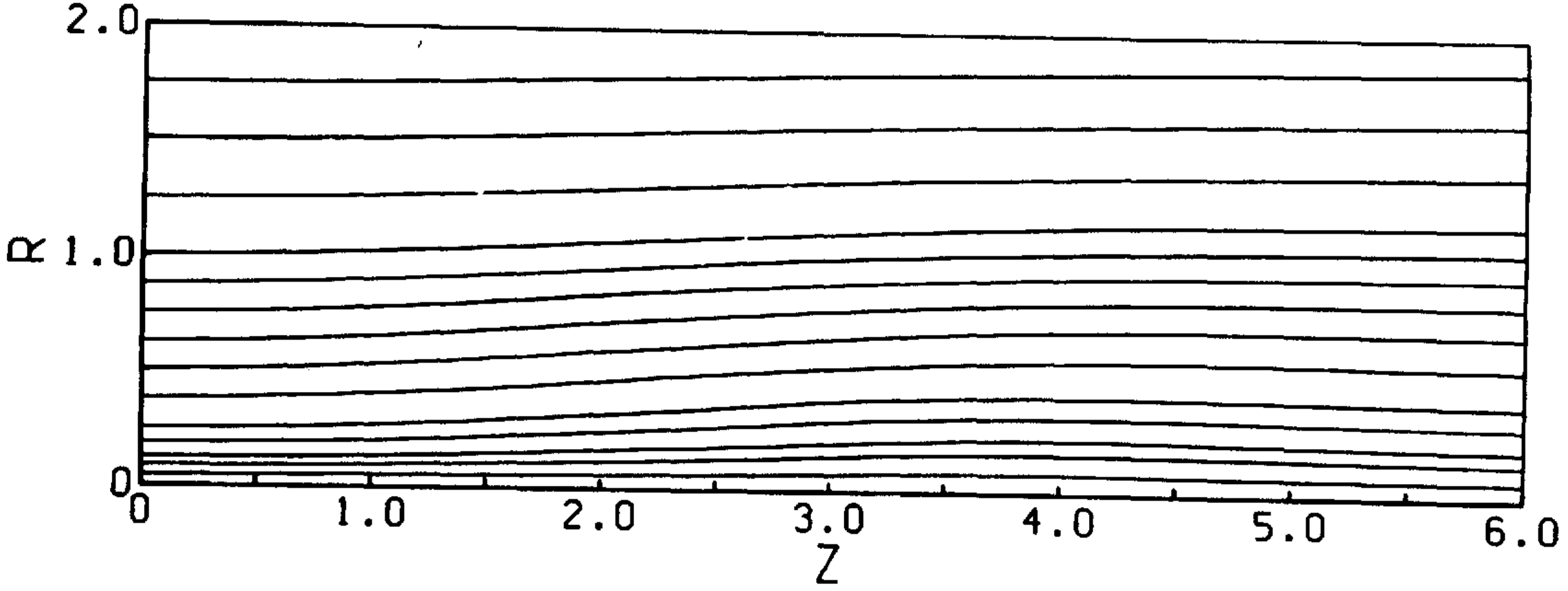

Fig. 19a. STREAM FUNCTION CONTOURS -- Re = 100, α = 1.0, V = 0.8944

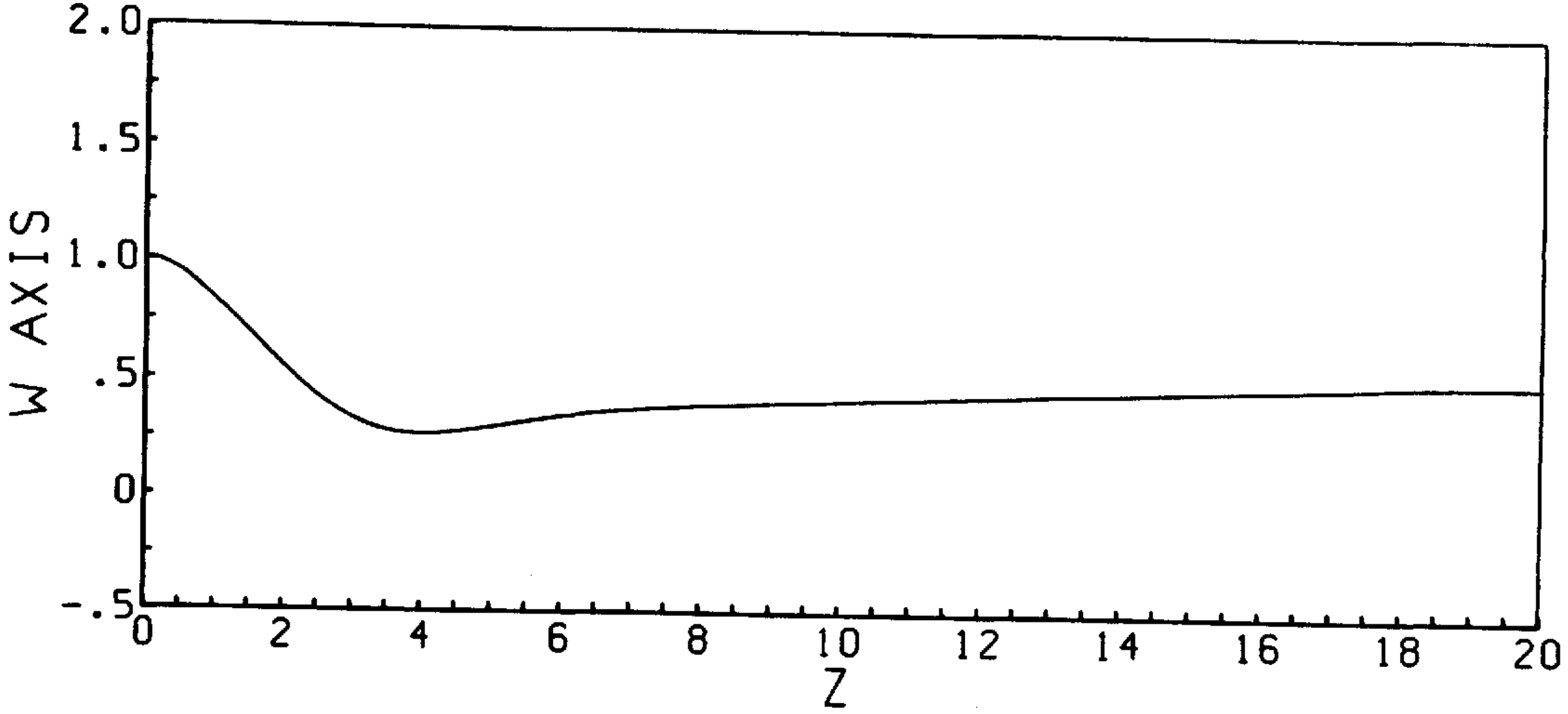

Fig. 19b. AXIAL VELOCITY ON AXIS vs. z -- Re = 100, α = 1.0, V = 0.8944

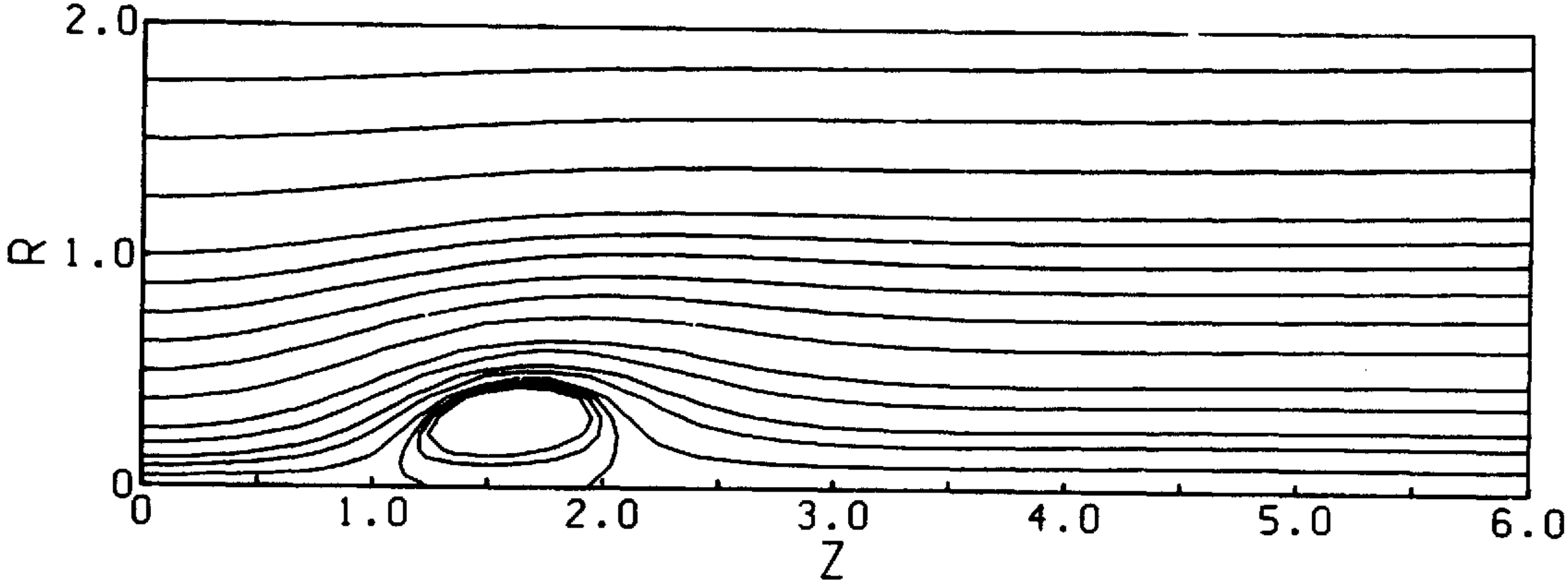

Fig. 20a. STREAM FUNCTION CONTOURS -- Re = 100, α = 1.0, V = 1.095

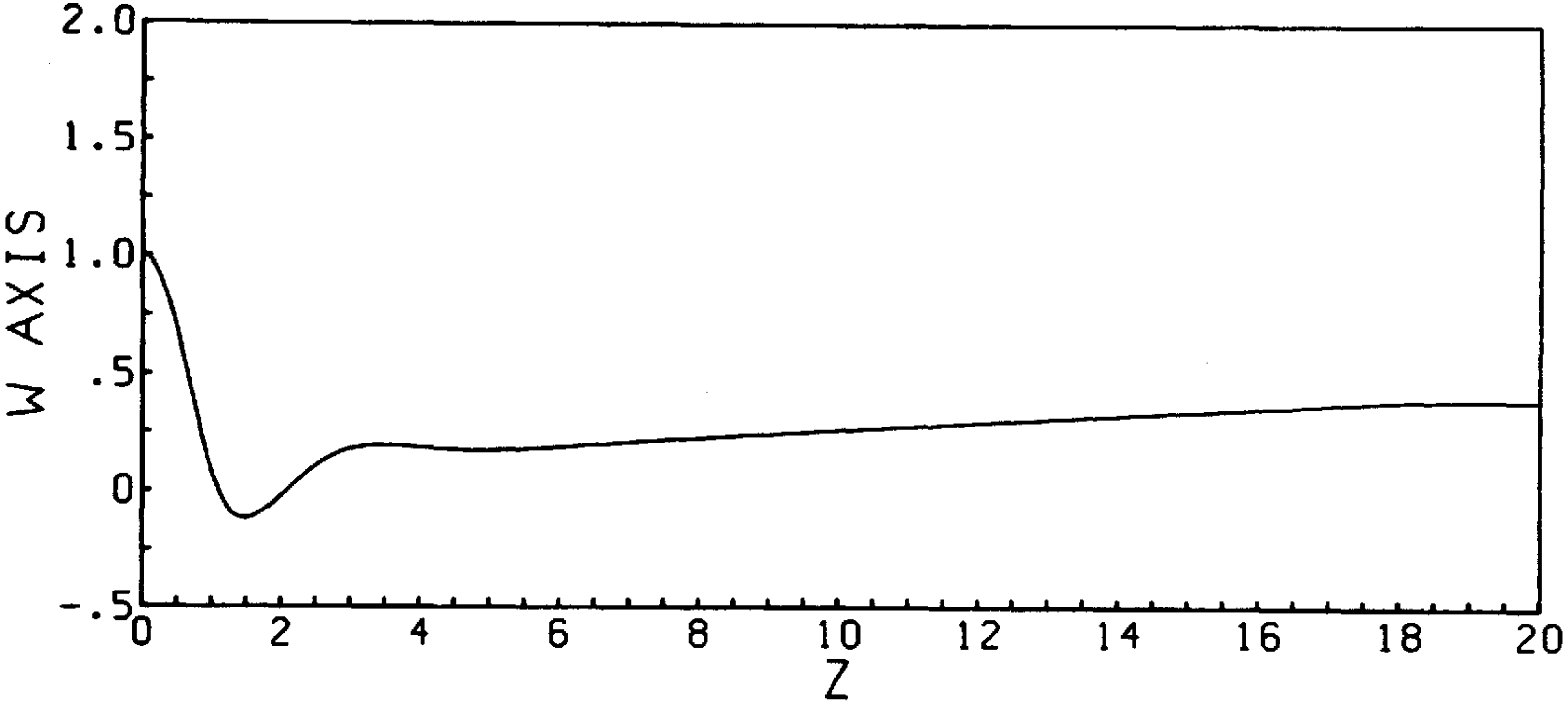

Fig. 20b. AXIAL VELOCITY ON AXIS vs z -- Re = 100, α = 1.0, V = 1.095

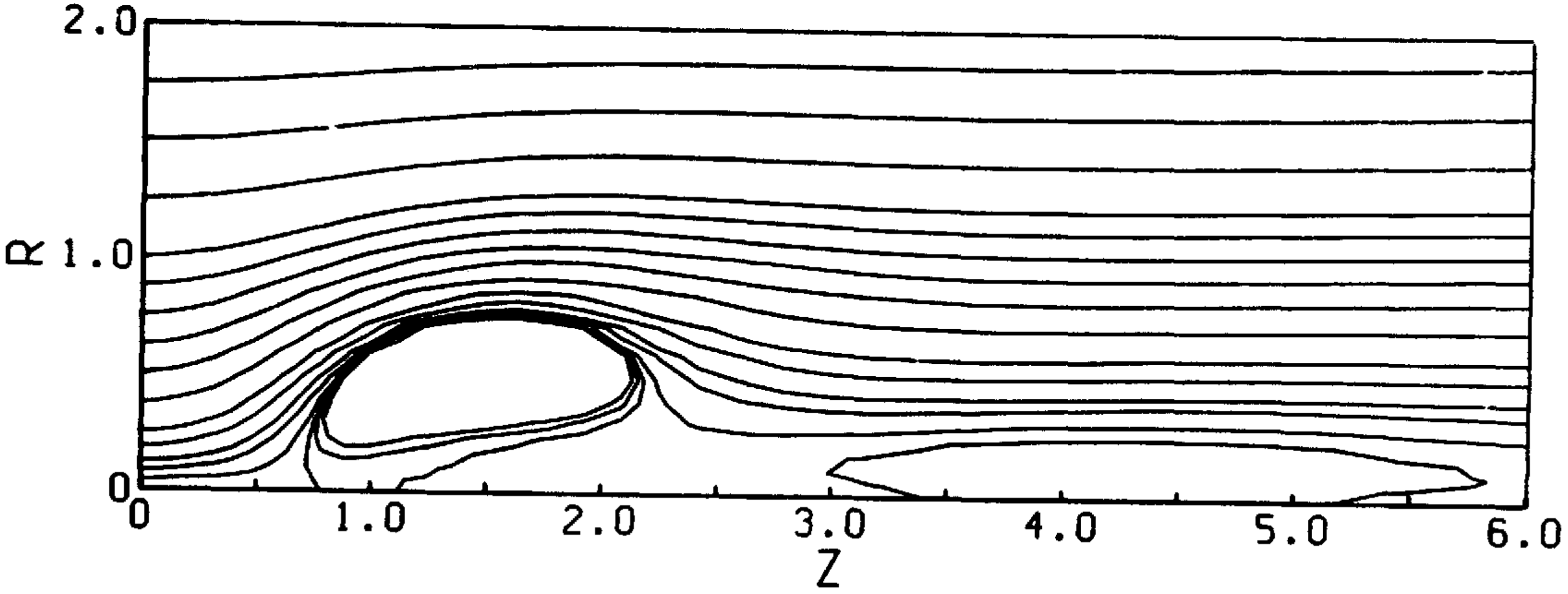

Fig. 21a. STREAM FUNCTION CONTOURS -- Re = 100, α = 1.0, V = 1.342

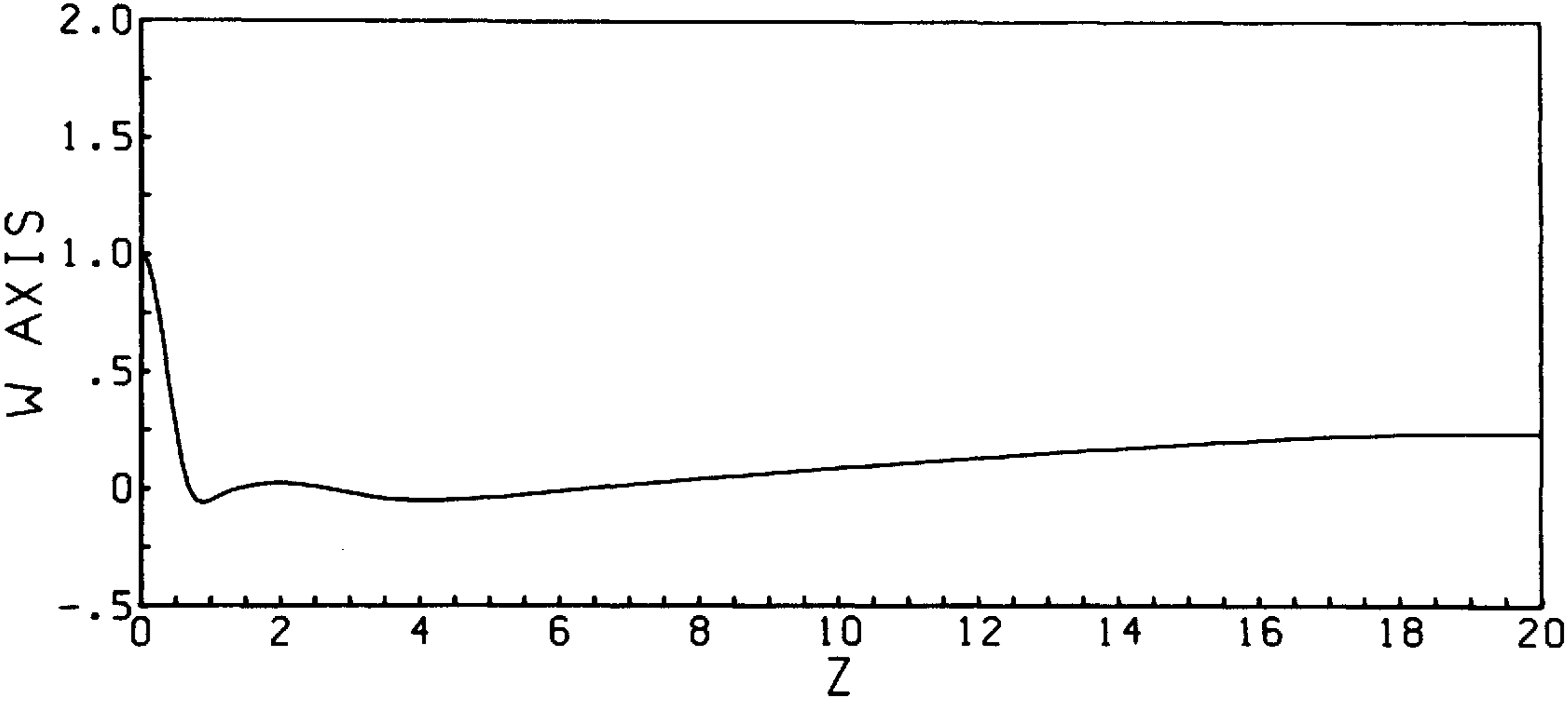

Fig. 21b. AXIAL VELOCITY ON AXIS vs. z -- Re = 100, α = 1.0, V = 1.342

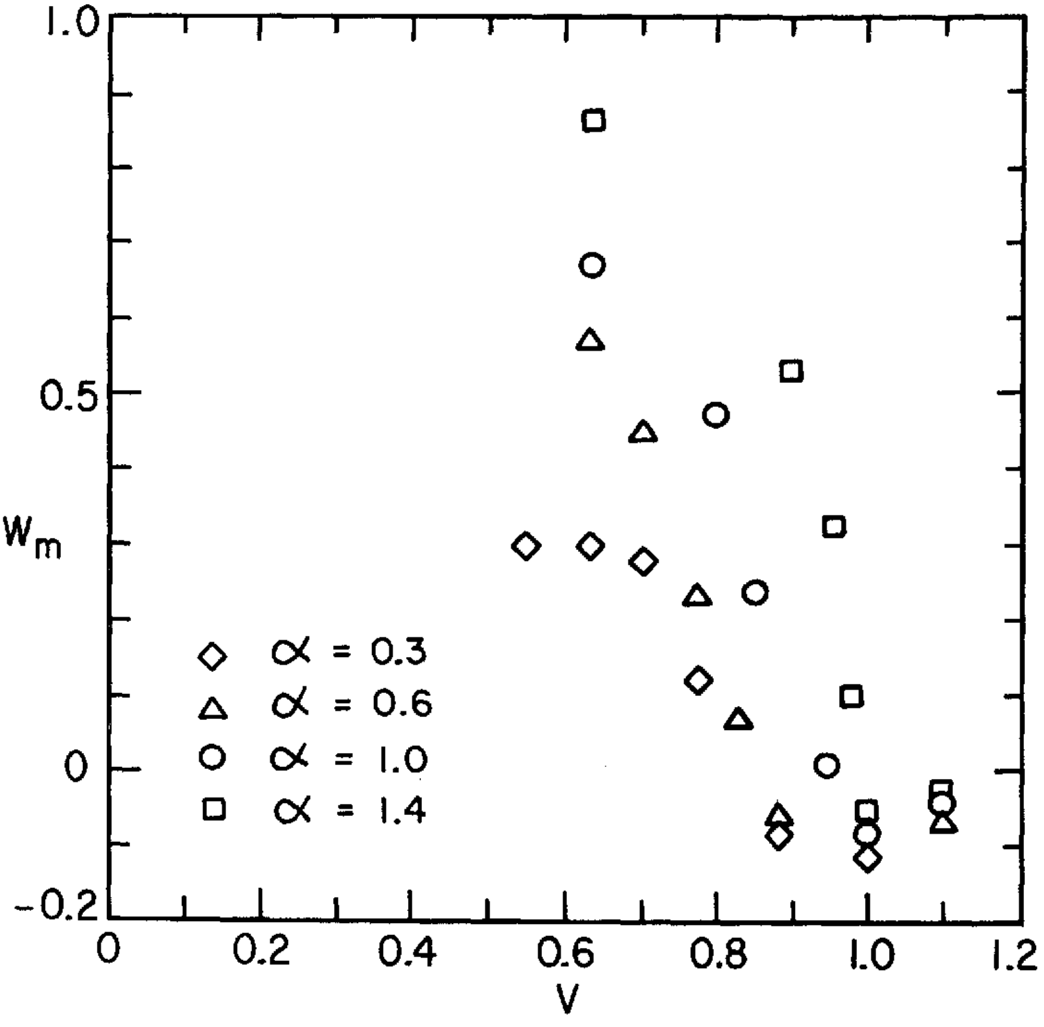

MINIMUM AXIAL VELOCITY AT AXIS VS. V
Re = 200

Fig. 22.

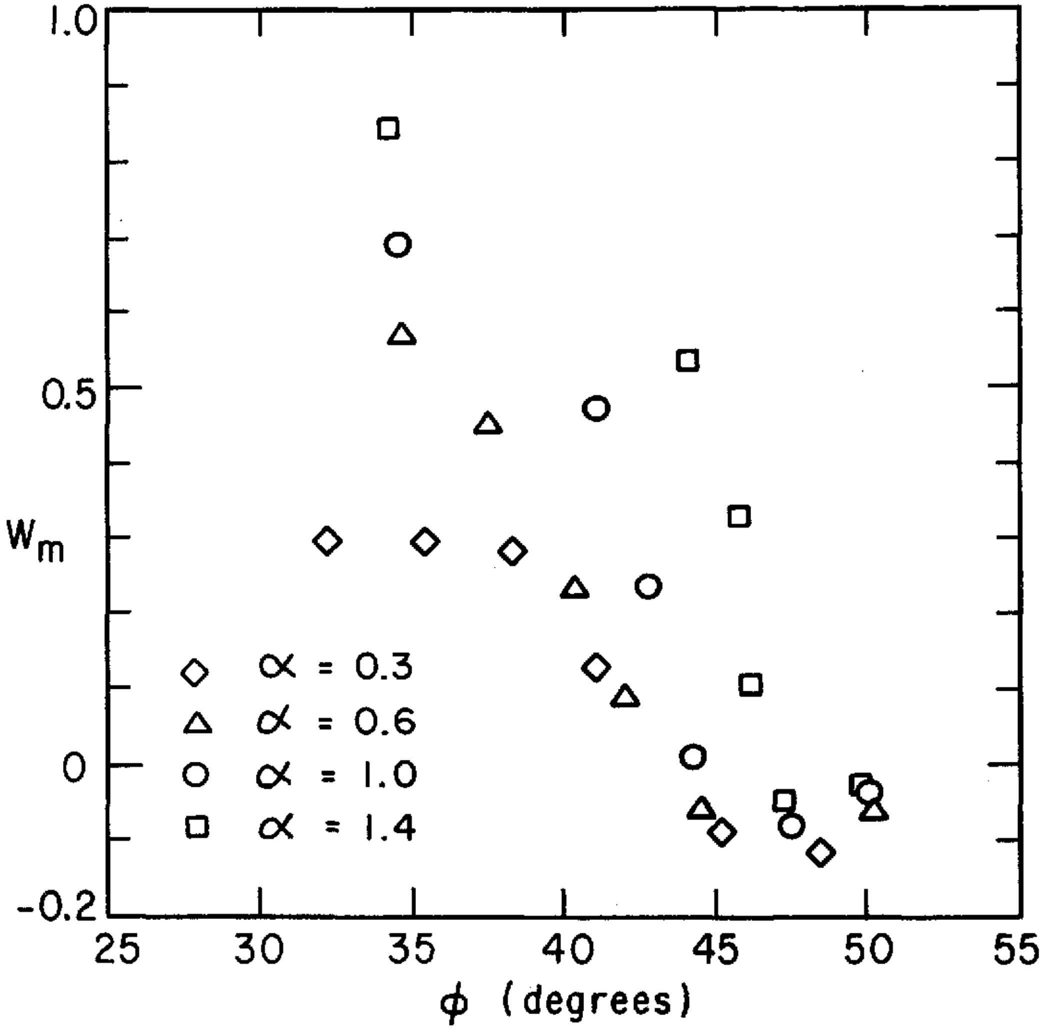

MINIMUM AXIAL VELOCITY AT AXIS
VS. SWIRL ANGLE ϕ

Fig. 23.

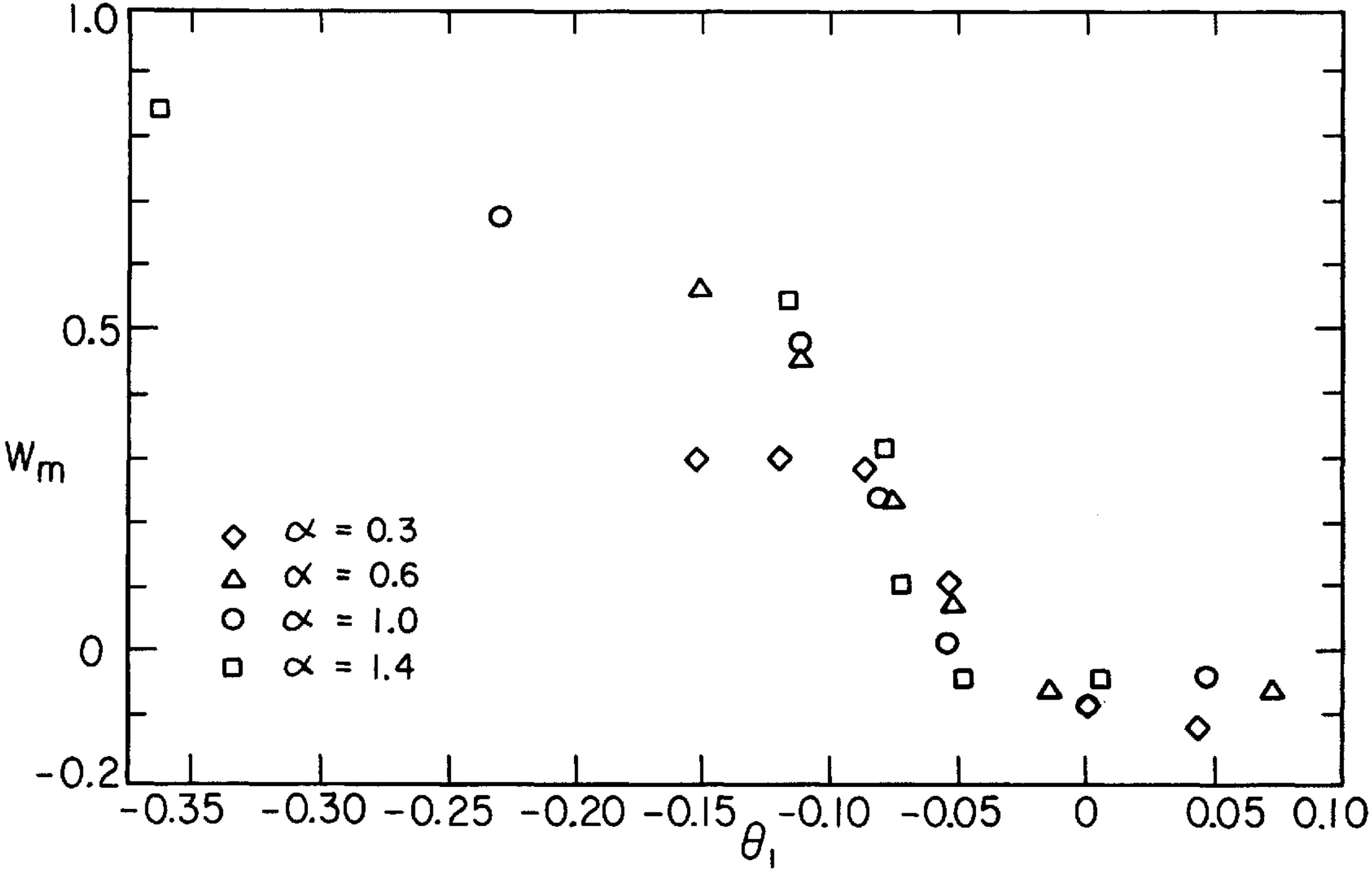

Fig. 24. MINIMUM AXIAL VELOCITY AT AXIS VS. θ_1
Re = 200

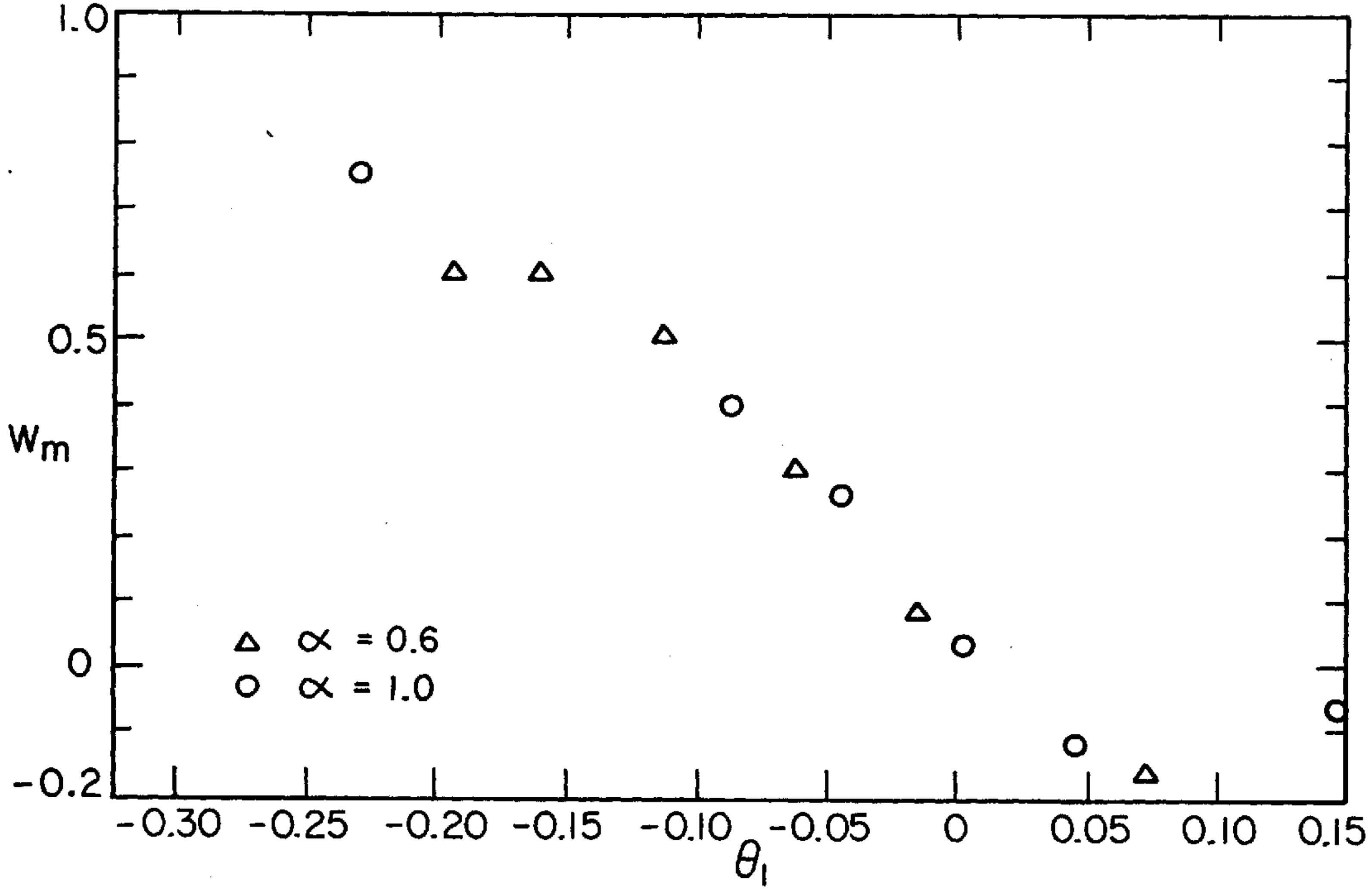

Fig. 25. MINIMUM VELOCITY AT AXIS VS. θ_1
Re = 100

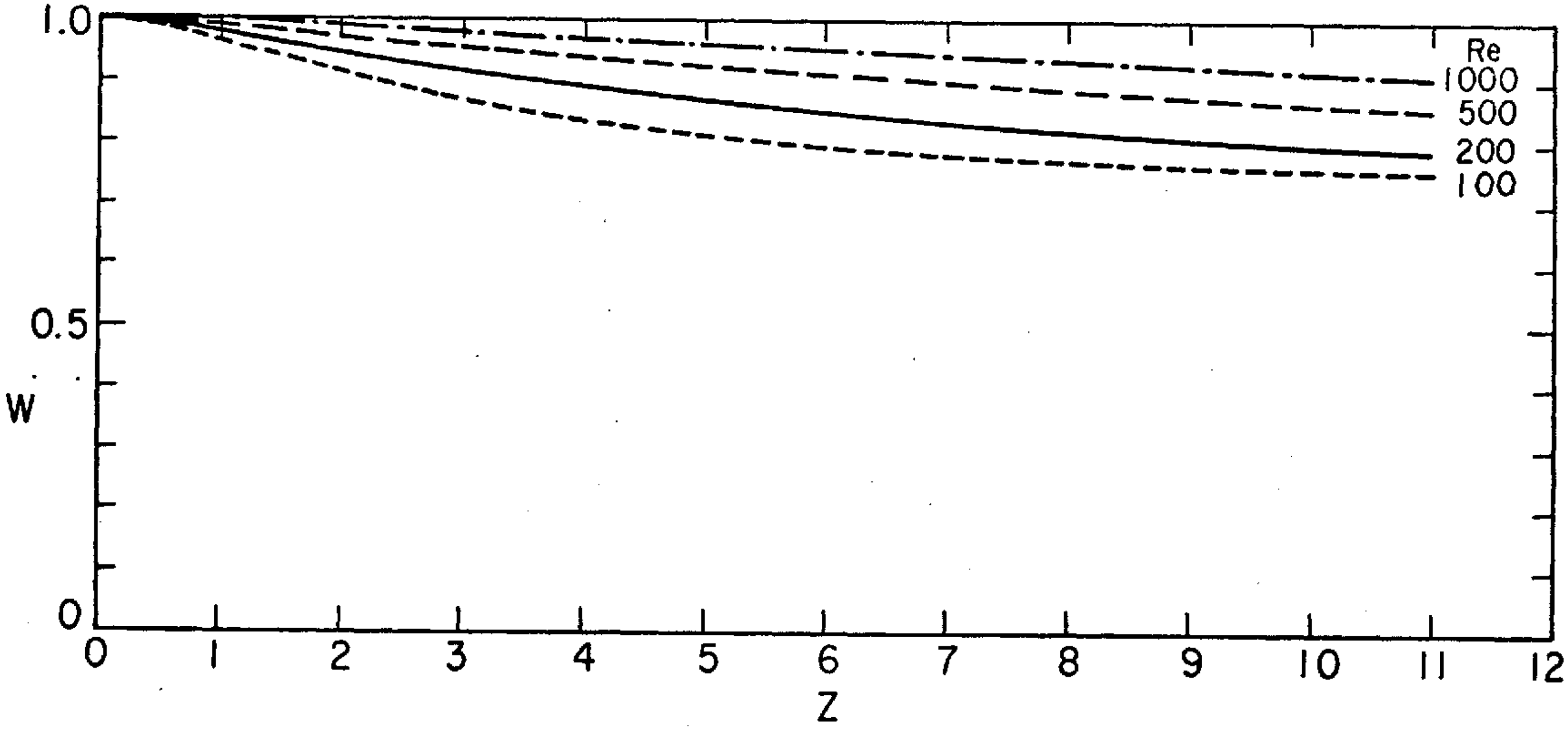

Fig. 26. AXIAL VELOCITY ON AXIS VS. Z
$\alpha = 1.0$ $V = 0.63$

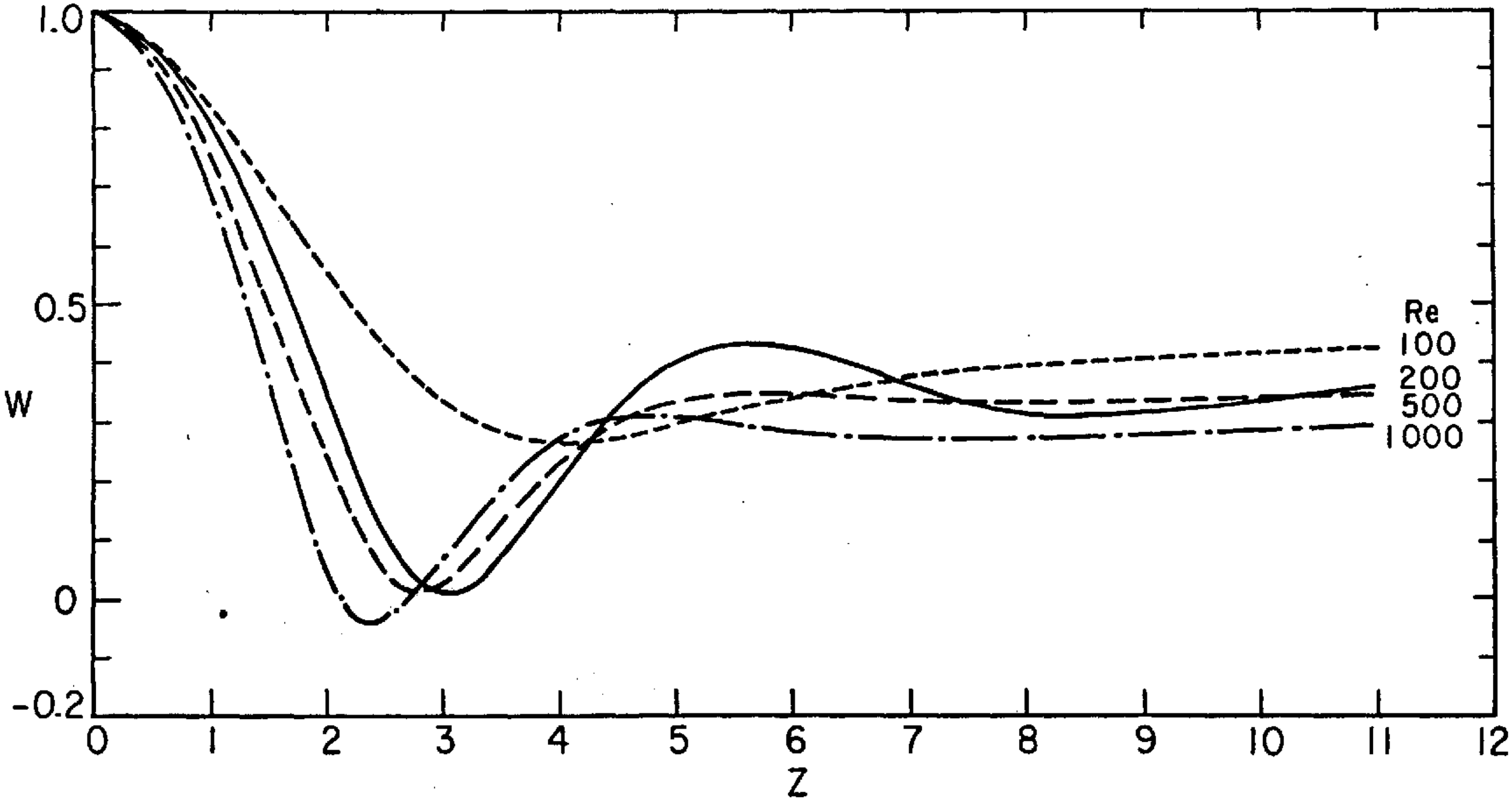

Fig. 27. AXIAL VELOCITY ON AXIS VS. Z
$\alpha = 1.0$ $V = 0.8944$

APPENDIX A

APPLICATION OF COORDINATE TRANSFORMATIONS

To write equations (2.5) through (2.8) in terms of the variables x and y, defined by the transformation equations (3.5) and (3.6), the following relations derived from the chain rule are required:

$$\frac{\partial}{\partial r} = \frac{\partial}{\partial y}\frac{dy}{dr} \tag{B-1}$$

$$\frac{\partial^2}{\partial r^2} = \frac{\partial^2}{\partial y^2}\left(\frac{dy}{dr}\right)^2 + \frac{\partial}{\partial y}\frac{d^2y}{dr^2} \tag{B-2}$$

$$\frac{\partial}{\partial z} = \frac{\partial}{\partial x}\frac{dx}{dz} \tag{B-3}$$

$$\frac{\partial^2}{\partial z^2} = \frac{\partial^2}{\partial x^2}\left(\frac{dx}{dz}\right)^2 + \frac{\partial}{\partial x}\frac{d^2x}{dz^2} \tag{B-4}$$

where, from equations (3-5) and (3-6),

$$\frac{dy}{dr} = \frac{e^{-ay}}{ab} \qquad \frac{d^2y}{dr^2} = -\frac{e^{-2ay}}{ab^2} \tag{B-5,6}$$

$$\frac{dx}{dz} = \frac{e^{-cx}}{cd} \qquad \frac{d^2x}{cz^2} = -\frac{e^{-2cx}}{cd^2} \tag{B-7,8}$$

Replacing derivatives in equations (2.5), (2.6), (2.7), and (2.8) by derivatives with respect to y and x using (B-1) through (B-4), while letting

$$f(y) = \frac{dy}{dr}\ , \quad y(y) = \frac{d^2y}{dr^2}\ , \quad s(x) = \frac{dx}{dz}\ ,$$

$$\text{and} \quad t(x) = \frac{d^2y}{dz^2}$$

yields the transformed equations (3.7), (3.8), (3.9), and (3.10).

APPENDIX B

FINITE DIFFERENCE FORMULATION

DIFFERENCE EQUATIONS

The ADI scheme applied to the momentum equations (3-7), (3-8), and (3-9), and the simple explicit scheme for the pressure equation (3-10) are explained as follows. The region $0 \leq x \leq 1$, $0 \leq y \leq 1/2$ in which a solution is to be obtained is overlaid with a grid system of N points in the x direction and M in the y direction. The location (x,y) of any grid point is given by the indices i,j with $x = (i-1)h$, $y = (j-1)k$, where h and k are the uniform mesh width in the x and y directions (Fig. 3). $u(x,y,t)$, $v(x,y,t)$ and $w(x,y,t)$ are represented by the functions u^n_{ij}, v^n_{ij} and w^n_{ij} defined at each grid point i,j. Superscript n is the number of time steps of length τ which are equivalent to t. $p(x,y,t)$ is represented by the function $p^n_{i+1/2,j+1/2}$ defined on a second grid staggered with respect to the first by a half mesh width in both coordinate directions.

Centered differences are used for all spatial derivatives with the notation

$$D_{01}\, V_{ij} \equiv \frac{V_{i+1j} - V_{i-1j}}{2h}$$

$$D_{+1}\, D_{-1}\, V_{ij} \equiv \frac{V_{i+1j} + V_{i-1j} - 2V_{ij}}{h^2}$$

$$D_{02}\, V_{ij} \equiv \frac{V_{ij+1} - V_{ij-1}}{2k}$$

$$D_{+2}\, D_{-2}\, V_{ij} \equiv \frac{V_{ij+1} + V_{ij-1} - 2V_{ij}}{k^2}$$

where V_{ij} can be u^n_{ij}, v^n_{ij} or w^n_{ij}. These difference forms approximate the first and second derivatives in the x and the y directions, respectively. The pressure derivatives in the momentum equations at a point ij are approximated by an averaged differencing on the staggered grid so that

$$D^*_{01}\, p_{ij} \equiv \frac{(p_{i+1/2,j+1/2}-p_{i-1/2,j+1/2})+(p_{i+1/2,j-1/2}-p_{i-1/2,j-1/2})}{2h}$$

$$D^*_{02}\, p_{ij} \equiv \frac{(p_{i+1/2,j+1/2}-p_{i+1/2,j-1/2})+(p_{i-1/2,j+1/2}-p_{i-1/2,j-1/2})}{2k}$$

represent $\partial p/\partial x$ and $\partial p/\partial y$ at i,j. Similarly, the velocity derivatives required to compute the pressure at a staggered grid point from the auxiliary continuity equation $i + 1/2$, $j + 1/2$ are approximated by the averaged differences

$$D^*_{01}\, w_{i+1/2,j+1/2}$$

$$\equiv \frac{(w_{i+1,j+1})+(w_{i+1,j}-w_{ij})}{2h}$$

$$D^*_{02}(u/e)_{i+1/2,j+1/2}$$

$$\equiv \frac{[(u/e)_{i+1,j+1}-(u/e)_{i+1,j}]+[(u/e)_{i,j+1}-(u/e)_{ij}]}{2k}$$

With $e_j = e(y)$, $f_j = f(y)$, $g_j = g(y)$, $s_i = s(x)$, $t_i = t(x)$, and using the definitions

$$u_{ij} \equiv u^n_{ij}$$

$$u'_{ij} \equiv u^{n+1/2}_{ij}$$

$$u''_{ij} \equiv u^{n+1}_{ij}$$

the finite difference equation for the two ADI sweeps, with the pressure computation are

First Sweep

$$\frac{u'_{ij}-u_{ij}}{\tau/2} + f_j u_{ij} D_{02} u_{ij} + s_i w_{ij} D_{01} u'_{ij} - v_{ij}^2 e_j$$

$$= - f_j D^*_{02} p_{ij} + \frac{1}{Re} [f_j^2 D_{+2} D_{-2} u_{ij} + (g_j + e_j f_j) D_{02} u_{ij}$$

$$+ s_i^2 D_{+1} D_{-1} u'_{ij} + t_i D_{01} u'_{ij} - u_{ij} e_j^2]$$

$$\frac{v'_{ij}-v_{ij}}{\tau/2} + f_j u_{ij} D_{02} v_{ij} + s_i w_{ij} D_{01} v'_{ij} + u_{ij} v_{ij} e_j$$

$$= \frac{1}{Re} [f_j^2 D_{+2} D_{-2} v_{ij} + (g_j + e_j f_j) D_{02} v_{ij}$$

$$+ s_i^2 D_{+1} D_{-1} v'_{ij} + t_i D_{01} v'_{ij} - v_{ij} e_j^2]$$

$$\frac{w'_{ij}-w_{ij}}{\tau/2} + f_j u_{ij} D_{02} w_{ij} + s_i w_{ij} D_{01} w'_{ij}$$

$$= - s_i D^*_{01} p_{ij} + \frac{1}{Re} [f_j^2 D_{+2} D_{-2} w_{ij} + (g_j + e_j f_j) D_{02} w_{ij}$$

$$+ s_i^2 D_{+1} D_{-1} w'_{ij} + t_i D_{01} w'_{ij}]$$

$$\frac{p'_{i+1/2,j+1/2} - p_{i+1/2,j+1/2}}{\tau/2}$$

$$= - [e_{j+1/2} f_{j+1/2} D^*_{02} (u/e)_{i+1/2,j+1/2}$$

$$+ s_{i+1/2} D^*_{01} w_{i+1/2,j+1/2}]/\delta$$

Second Sweep

$$\frac{u''_{ij}-u'_{ij}}{\tau/2} + f_j u'_{ij} D_{02} u''_{ij} + s_i w'_{ij} D_{01} u'_{ij} - v'^{2}_{ij}\, e_j$$

$$= - f_j \overset{*}{D}_{02} p'_{ij} + \frac{1}{Re}\,[f_j^2 D_{+2} D_{-2} u''_{ij} + (g_j + e_j f_j) D_{02} u''_{ij}$$

$$+ s_i^2 D_{+1} D_{-1} u'_{ij} + t_i D_{01} u'_{ij} - u''_{ij} e_j^2]$$

$$\frac{v''_{ij}-v'_{ij}}{\tau/2} + f_j u'_{ij} D_{02} v''_{ij} + s_i w'_{ij} D_{0k} v'_{ij} + u'_{ij} v'_{ij} e_j$$

$$= \frac{1}{Re}\,[f_j^2 D_{+2} D_{-2} v''_{ij} + (g_j + e_j f_j) D_{02} v''_{ij}$$

$$+ s_i^2 D_{+1} D_{-1} v'_{ij} + t_i D_{01} v'_{ij} - v''_{ij} e_j^2]$$

$$\frac{w''_{ij}-w'_{ij}}{\tau/2} + f_j u'_{ij} D_{02} w''_{ij} + s_i w'_{ij} D_{01} w'_{ij}$$

$$= - s_i \overset{*}{D}_{01} p'_{ij} + \frac{1}{Re}\,[f_j^2 D_{+2} D_{-2} w''_{ij} + (g_j + e_j f_j) D_{02} w''_{ij}$$

$$+ s_i^2 D_{+1} D_{-1} w'_{ij} + t_i D_{01} w'_{ij}]$$

$$\frac{p''_{i+1/2,j+1/2} - p'_{i+1/2,j+1/2}}{\tau/2}$$

$$= - [e_{j+1/2} f_{j+1/2} \overset{*}{D}_{02} (u'/e)_{i+1/2,j+1/2}$$

$$+ s_{i+1/2} \overset{*}{D}_{01} w'_{i+1/2,j+1/2}]/\delta$$

When rearranged, the finite difference momentum equations are of the form

$$A_i U_{i-1} + B_i U_i + C_i U_{i+1} = D_i \qquad \text{(B-1)}$$

$$2 \leq i \leq N-1$$

U_i is obtained, therefore, by the inversion of a tridiagonal matrix. The criterion that such a matrix be well-conditioned, $B_i > -(A_i+C_i)$, is always satisfied. Methods for inverting tridiagonal matrices when U_1 and U_N are specified are well known (Richtmyer and Morton, 1967). Extensions to other boundary conditions have been given by Roache (1972).

The existence of two vectors E_i and F_i may be postulated such that

$$U_i = F_i + E_i\, U_{i+1} \qquad \text{(B-2)}$$

Combining (B-1) and (B-2) yields

$$U_i = \frac{D_i - A_i\, F_{i-1}}{B_i + A_i\, E_{i-1}} - \frac{C_i}{B_i + A_i\, E_{i-1}}\, U_{i+1}$$

Comparison with (B-2) results in the recursion relations

$$F_i = \frac{D_i - A_i\, F_{i-1}}{B_i + A_i\, E_{i-1}} \quad , \quad E_i = \frac{-\,C_i}{B_i + A_i\, E_{i-1}} \qquad \text{(B-3),(B-4)}$$

A_i, B_i, C_i and D_i are all known and application of the boundary condition at $i = 1$ yields E_1 and F_1, as follows.

Equation (B-2) at $i = 1$ is

$$U_1 = F_1 + E_1 U_2 \tag{B-5}$$

For a Dirichlet boundary condition, $U_1 = a$, (B-5) requires $F_1 = a$, $E_1 = 0$, while for a Neumann boundary condition, $\partial U/\partial y = 0$, so to first order $U_2 = U_1$ and, therefore, (B-5) requires $F_1 = 0$, $E_1 = 1$.

With E_1 and F_1 specified,(B-3) and (B-4) determine all E_i and F_i, $i < N$.

The boundary condition at $i = N$ specifies U_N as follows. For a Dirichlet condition $U_N = C$ where C is specified. For a Neumann condition, $\partial U/\partial y = 0$, so $U_{N-1} = U_N$ to first order and from

$$U_{N-1} = F_{N-1} + E_{N-1} U_N \tag{B-6}$$

the requirement that

$$U_N = \frac{F_{N-1}}{1 - E_{N-1}} \tag{B-7}$$

is obtained.

For a mixed condition, $V + \alpha(\partial V/\partial y) = 0$, so that

$$U_N + \alpha\left(\frac{U_N - U_{N-1}}{h} \right) = 0 \tag{B-8}$$

to first order, and therefore from (A-6)

$$U_N = \frac{F_N-1}{\beta - E_{N-1}} \qquad \text{where} \quad \beta = \frac{1 + \alpha/h}{\alpha/h}$$

With E_i, F_i and U_N known, (B-2) may be used to compute U_i, $1 \leq i \leq N-1$.

Each sweep, therefore, proceeds as follows

(1) calculation along each row or column of the coefficients A_i, B_i, C_i and D_i for each of the tridiagonal matrices for u_{ij}, v_{ij} and w_{ij},

(2) calculation of E_1 and F_1 and, hence, E_i and F_i for each variable from the boundary conditions at $i = 1$ (or $j = 1$),

(3) application of the boundary conditions at $i = N$ (or $j = M$) and calculation of u_{ij}, v_{ij} and w_{ij} for that row or column,

(4) explicit pressure computation.